eman ta zabal zazu

Universidad del País Vasco
Euskal Herriko Unibertsitatea

Ultrastrong light-matter interaction in quantum technologies

Simone Felicetti

Supervisor:

Prof. Enrique Solano

Departamento de Química Física
Facultad de Ciencia y Tecnología
Universidad del País Vasco UPV/EHU

Leioa, September 2015

La biblioteca es ilimitada y periódica [..]
Mi soledad se alegra con esa elegante esperanza.

La Biblioteca de Babel, Jorge Luis Borges

The library is unlimited and periodic [..]
My solitude is gladdened by that elegant hope.

The Library of Babel, Jorge Luis Borges

Abstract

In the last decades, the experimental and theoretical study of light-matter interactions in confined quantum systems has allowed to considerably widen and deepen our understanding of the quantum world. The simplest fully-quantized light-matter interaction is the quantum Rabi model (QRM), where a two-level system is coupled to a single bosonic mode. The implementation of quantum-optical systems in which the interaction strength overcomes losses brought a revolution to this research area. Under this condition, dubbed strong coupling (SC) regime, quantum processes can be observed at the single-photon level, and even exploited to perform Quantum Information tasks. Recent developments in solid-state Quantum Technologies have made possible to push the line further, achieving the ultrastrong coupling (USC) regime of the QRM, in which the interaction strength is comparable with the bare frequencies of the interacting systems.

In the USC regime of the QRM, light and matter degrees of freedom merge into collective bound states called polaritons, the system ground state is not the vacuum and excitations are not conserved. The growing interest in USC-related phenomena is mainly motivated by the fundamental counterintuitive modifications to light-matter interactions entailed by this regime. At the same time, the USC regime is also expected to provide computational benefits in terms of operational speed, coherence time, and noise protection.

In this Thesis, we theoretically analyze novel quantum phenomena emerging in the USC regime, which can be observed using nowadays technology and can motivate foreseeable improvements. The results here presented have been derived using two conceptually different approaches. On one side, we have analyzed interesting models that can be implemented in superconducting circuits, a quantum platform where the USC regime can be naturally achieved. In particular, we focused on excitation transfer across USC impurities, entanglement generation via modulation of electrical boundary conditions and quantum state engineering in ultrastrongly-coupled systems. On the other hand, we have developed methods to reproduce the physics of light-matter interactions in the USC regime, by tailoring the Hamiltonian of atomic systems, like trapped ions and cold atoms. These proposals take profit of the specific features of such quantum platforms, in order to implement regimes and measurements that are not directly accessible.

We believe that this Thesis will contribute to develop a thorough understanding of quantum phenomena related to the USC regime of light-matter interaction, and that it will foster the dialog between experimental and theoretical research in this area.

Acknowledgements

I would like to thank first my PhD supervisor Prof. Enrique Solano, for his constant support and invaluable guidance. Countless thought-provoking discussions held with him during my PhD studies have contributed to develop my critical skills, and his advice has covered all facets of nowadays top-level research.

I cannot fail to thank all members of the QUTIS research group, for the nice and friendly working environment and for all the time spent together, be in the UPV/EHU campus, in Bilbao or around the world. Special thanks go to Prof. Guillermo Romero, who has been co-supervising and supporting me since day one, and to Dr. Enrique Rico, who has guided me during the final period of my research work and through the redaction of this Thesis.

I would like to thank also several researchers that I have had the pleasure to interact or collaborate with, during my PhD studies. Warm thanks go to Dr. Davide Rossini and Prof. Rosario Fazio from Scuola Normale Superiore di Pisa, for inviting me to visit them and for the great work done together, studying excitation transfer in resonator arrays. Special thanks to Prof. Leong Chuan Kwek, Prof. Dimitris Angelakis and M.Sc. Thi Ha Kyaw from Centre for Quantum Technologies, for all that I have learned during my visits in Singapore, and for the great teamwork. Special thanks also to Dr. Frank Deppe, Dr. Achim Marx and Prof. Rudolf Gross from Walther Meissner Institute, for inviting me several times to visit Garching Forschungszentrum and for the constant interaction. I would like to express my gratitude to Prof. Göran Johansson and Prof. Per Delsing from Chalmers University of Technology, for the great work done together on entanglement generation via DCE, and for their valuable teaching during my stay in Gothenburg. I thank Prof. Steven Girvin at Yale University for giving me the opportunity to discuss physics with him, also having the chance to visit the labs of Prof. Michel Devoret and Prof. Robert Shoelkopf. Many thanks to Prof. Andrew Houck from Princeton University, for the nice welcoming and the interesting discussions. I have to thank also Prof. William Oliver at Massachusetts Institute of Technology, for detailed explanations of the experiments carried on in his laboratory. Warm thanks go to Prof. Pérola Milman and her group Member M.Sc. Tom Douce from Laboratoire Matériaux et Phénomènes Quantiques, for all the stimulating discussions and the great work done together developing methods to achieve quantum control in the USC regime.

I cannot fail to thank Prof. Ivette Fuentes and Dr. Carlos Sabín from Nottingham University, I have profited greatly from their hospitality and I have really enjoyed the work done together on the simulation of quantum relativistic effects. I thank sincerely Dr. Daniel Braak from Augsburg University, for the nice work done together studying the two-photon quantum Rabi model, wandering back and forth all the way from applied physics to pure mathematics. I have also profited hugely from the hospitality of Prof. Martin Weitz from Bonn University, it has been interesting and stimulating to work with him and his group members on a quantum simulation of the quantum Rabi model.

To conclude, I want to thank people that are especially important to me. My father, for teaching me the value of culture and of independent thinking. My mother, for passing on to me the will and the strength to shape my own existence. My family, I still wonder at how their love and support cut through the Alps and the Pyrenees unaffected. My muse, Marta, that changed my life. My friends, I feel really lucky for having met so many wonderful people willing to bear me in good and bad times, in good and bad moods.

Without you, neither light nor matter would make much sense to me.

Contents

List of Figures

List of publications

I) **The results of this Thesis are based on the following articles**

Published Articles

1. S. Felicetti, G. Romero, D. Rossini, R. Fazio, and E. Solano
   Photon transfer in ultrastrongly coupled three-cavity arrays
   Phys. Rev. A, **89**, 013853 (2014).

2. S. Felicetti, M. Sanz, L. Lamata, G. Romero, G. Johansson, P. Delsing, and E. Solano
   Dynamical Casimir Effect Entangles Artificial Atoms
   Phys. Rev. Lett. **113**, 093602 (2014).

3. S. Felicetti, T. Douce, G. Romero, P. Milman and E. Solano
   Parity-dependent State Engineering and Tomography in the ultrastrong coupling regime
   Sci. Rep. **5**, 11818 (2015).

4. S. Felicetti, J. S. Pedernales, I. L. Egusquiza, G. Romero, L. Lamata, D. Braak, and E. Solano
   Spectral Collapse via Two-phonon Interactions in Trapped Ions
   Phys. Rev. A **92**, 033817 (2015).

5. J. S. Pedernales, I. Lizuain, S. Felicetti, G. Romero, L. Lamata, and E. Solano
   Quantum Rabi Model with Trapped Ions
   e-print arXiv:1505.00698, accepted in Sci. Rep. (2015).

In preparation

6. S. Felicetti, E. Rico, M. Leder, C. Grossert, M. Weitz, and E. Solano
   Quantum Rabi model in periodic phase space with cold atoms.

7. D. Rossatto, S. Felicetti, H. Eneriz, E. Rico, E. Solano, and M. Sanz
   Selection rules of coupled polaritons in superconducting circuits.

II) **Other articles produced during the Thesis period and not included**

Published Articles

8. T. H. Kyaw, S. Felicetti, G. Romero, E. Solano, and L. C. Kwek
   Scalable quantum memory in the ultrastrong coupling regime
   Sci. Rep. **5**, 8621 (2015).

9. S. Felicetti, C. Sabín, I. Fuentes, L. Lamata, G. Romero, and E. Solano
   Relativistic Motion with Superconducting Qubits
   Phys. Rev. B, **92**, 064501 (2015).

Submitted Articles

10. R. Di Candia, K. G. Fedorov, L. Zhong, S. Felicetti, E. P. Menzel, M. Sanz, F. Deppe, A. Marx, R. Gross, and E. Solano
    Quantum teleportation of propagating quantum microwaves
    e-print arXiv:1506.06701, submitted for publication.

In preparation

11. J. J. Mendoza-Arenas, S. R. Clark, S. Felicetti, G. Romero, E. Solano, D. G. Angelakis, and D. Jaksch
    Beyond mean-field bistability in driven-dissipative lattices: bunching-antibunching transition and quantum simulation.

Chapter 1

Introduction

1.1 Light-matter interaction

The interaction between the electromagnetic field and matter, be in solid state or atomic systems, is one of the most fundamental and ubiquitous physical processes. As transparent or reflective media can be used as tools to generate non-trivial states of light, the latter can be used, in turn, as probes to improve the analysis of materials. As a result of this interplay, the study of light-matter interaction has yielded an amazing variety of technological applications and novel scientific methodologies, from the earliest refracting telescopes to atomic clocks. Indeed, with the advent of quantum mechanics, it has played a key role in the scientific and technological revolution that led to current quantum technologies.

The theory of quantum mechanics itself was born out of the necessity of explaining the spectral distribution of the electromagnetic radiation produced by a thermal source. After Planck's postulation of energy quantization [1], Einstein introduced [2] first the hypothesis of *corpuscularity* of light as a possible explanation for the photoelectric effect and, in 1916, he proposed [3] a phenomenological theory for the atomic absorption and emission of light. A formal quantization of the electromagnetic field was derived [4] by Dirac in 1927, opening the way that led to the derivation of the full-fledged quantum electrodynamics (QED) [5]. Nevertheless, despite notable efforts [6–8], all quantum-optical experiments performed in the first half of the twentieth century could be explained with classical or semiclassical theories. Finally, with the invention of the laser [9] in 1960, the development of a full quantum theory both for the atoms and for the field became unavoidable. In the same years, the first contributions [10, 11] by Glauber on quantum theories of optical coherence gave birth to the modern research field of quantum optics.

Since then, our ability to implement controllable quantum systems has been steadily growing, until reaching the accuracy needed to engineer light-matter interactions at the single-photon level. This milestone achievement was made possible by the confinement of atoms and light modes into reflective cavities, a research area know as cavity QED. Notice that the behavior of a quantum system depends more on its fundamental statistical and spectral features than on the physical origins of the degrees of freedom involved. Accordingly, the concept of light-matter interaction has adopted a more comprehensive meaning, that is, the interaction between bosonic fields (light) and anharmonic systems (matter), whose dynamics effectively involves few energy levels. The possibility of controlling such interactions was demonstrated in the seminal works of Haroche [12], in which a stream of atoms controls the field in a microwave cavity, and Wineland [13], in which the interaction between vibrations and electronic excitations of atoms in a magnetic trap is controlled by means of optical drivings.

Nowadays, an impressive variety of quantum technologies have been developed [14]. Trapped ions, microwave or optical cavities, ultra cold atoms, photonic systems, semiconductor nanocrystals, superconducting circuits and nanomechanical devices form an incomplete list of the most promising platforms. As this Thesis is being redacted, quantum systems are on the brink of becoming applicable in commercial information technologies, where they are expected to provide an exponential gain in computational power, the ability of efficiently simulating complex quantum systems and classically-unbreakable encryption protocols. Beyond practical applications, the growing complexity of experiments in the quantum regime is still deepening and broadening our understanding of quantum phenomena. As notable examples, novel theoretical tools are needed in order to understand quantum many-body physics, the role of causality, the principles of quantum correlations, quantum thermodynamics, and the physics of novel quantum regimes, as the ultrastrong coupling regime, subject of the present work.

1.1.1 Ultrastrong coupling regime of the quantum Rabi model

In the framework of cavity QED, the most fundamental model of light-matter interaction is given by an atomic dipole coupled to a single mode of the electromagnetic field. The first semiclassical version of this system has been proposed by Rabi [15] in 1937. The full quantum version of this model, dubbed quantum Rabi model (QRM), is given by the following Hamiltonian

$$H_{\mathrm{R}} = \omega a^{\dagger} a + \frac{\omega_q}{2}\sigma_z + g\sigma_x \left(a^{\dagger} + a\right), \tag{1.1}$$

where $a^\dagger$, a are creation and annihilation operators of the bosonic field, while σ_i are Pauli matrices describing the Hilbert space of a two-level quantum system, or *qubit*. We define the field and qubit energy spacing ω and ω_q, respectively, and the coupling strength g. We will use γ_i to denote the dissipation and decoherence rates of the non-unitary processes due to unavoidable couplings with the environment. In order to observe a complete Rabi cycle, i.e., a coherent exchange of excitation between the bosonic field and the qubit, the interaction strength g must overcome all dissipation rates γ_i. When this is the case, the system is said to be in the strong coupling regime. This challenging condition has been reached [16] for the first time in 1987 using single atoms interacting with microwave cavities.

More recently, and in this Thesis, the term strong coupling (SC) is used to define the parameter regime such that the light-matter coupling strength is larger than dissipations, $g \gg \gamma_i$, but also smaller than the system characteristic frequencies, i.e., $g \ll \omega$ and $g \ll \omega_q$. In the SC regime, a rotating-wave approximation can be performed, replacing the quantum Rabi Hamiltonian with

$$H_{\mathrm{R}} = \omega a^\dagger a + \frac{\omega_q}{2}\sigma_z + g\left(\sigma_- a^\dagger + \sigma_+ a\right), \tag{1.2}$$

where $\sigma_\pm = (\sigma_x \pm i\sigma_y)$. This Hamiltonian, known as Jaynes-Cummings (JC) model, has been introduced [17] in 1963 in order to study the relation between the semiclassical approach and a full quantum theory. The JC model is analytically solvable and it has been used for decades to describe a plethora of experiments in the quantum regime [18].

The system enters the ultrastrong coupling (USC) regime when the coupling strength becomes comparable with the bosonic mode frequency $g/\omega \gtrsim 0.1$. In this case, the rotating wave approximation cannot be applied and the full quantum Rabi model must be taken into account. The bosonic field and the qubit merge into bound states called polaritons, and the system ground state is not the vacuum, as in the SC regime. In fact, it contains a number of photons proportional to the ratio $(g/\omega)^2$. In the USC regime, excitations are not conserved and the simple pattern of excitation transfer typical of the JC dynamics disappears. Despite its seeming simplicity, the QRM is not integrable, and formal solutions for the eigenspectrum have been found only recently [19, 20].

The ratio between the coupling strength and field frequency of the first atom-cavity systems was of the order of [21] $g/\omega \approx 10^{-3}$. Requiring an improvement of three orders of magnitude, the USC regime has long been considered unphysical. In fact, recent development in quantum technologies have shown that achieving the USC regime of light-matter interaction is possible, using semiconducting quantum wells [22–24], superconducting circuits [25–28], arrays of electronic split-ring resonators [29, 30] and,

possibly, nano mechanical devices [31]. Besides purely technological advances, the fundamental improvement that makes the USC regime achievable in those systems is the confinement of the bosonic mode to one- or two-dimensional media and, in some cases, the use of synthetic matter.

In the last decade, the USC regime has been gathering growing theoretical and experimental interest. The most outstanding features of the USC regime are the highly non-trivial properties of the ground state [32–34], counter-intuitive dissipation processes [35, 36], the possibility of generating non-classical states [37–39], and novel transport and scattering properties [40, 41]. The model is also expected to have a qualitatively different behavior when the coupling strength becomes larger than the bosonic mode frequency, a condition that has been called deep strong coupling regime [42]. Furthermore, besides the interest in these fundamental quantum phenomena, the USC regime is expected to entail computational benefits, in terms of robustness against external noise [43, 44] and operational speed [45].

1.2 Quantum technologies

Before introducing the original contribution discussed in the present Thesis, let us briefly review the quantum technologies that are going to be considered. Circuit cavity QED stands out as the most appropriate platform in which the USC regime can be achieved in a natural way. On the other hand, trapped ions and ultracold atoms are good examples of extremely controllable quantum systems, where engineering the Hamiltonian allows to implement models of light-matter interaction in the USC regime.

1.2.1 Circuit quantum electrodynamics

Cavity quantum electrodynamics studies the coupling of atoms with discrete photon modes, in cavities with high quality factor. Circuit QED consists in reproducing such fundamental interactions using superconducting circuits. The key ingredients are transmission line resonators (TLR), which support discrete bosonic modes, and artificial atoms, i.e., quantum circuits with an anharmonic spectrum. The required anharmonicity is obtained exploiting the non-linear inductance of Josephson junctions [46]. TLRs are around 1cm long, and they support microwaves modes at frequencies $\omega = 2\pi \times (3 - 10)$GHz. Artificial atoms, also called superconducting qubits, are of the order of 1μm, hence their spatial extension is generally negligible with respect to TLR modes wavelengths.

Proposed [47] and experimentally implemented [48, 49] for the first time in 2004, circuit QED has swiftly become one of the most promising platform for the realization of controllable quantum systems and for the implementation of quantum computing tasks. With respect to other quantum technologies, circuit QED benefit of a high degree of tunability and scalability, and of the capability of achieving extremely large light-matter couplings. Single-qubit gates can be performed in 5ns, and two-qubit gates in less than 50ns, resulting in an amazing number of operations that can be performed within the coherence time of superconducting qubits, that can be as high [50] as 90μs. For now, the main drawbacks of this platform are the finite fabrication precision, which introduces inhomogeneities in artificial atoms, and the lack of single photon detectors for microwave frequencies.

A variety of different designs have been developed for superconducting qubits, exploiting the charge [51, 52], flux [53] or superconducting phase [54] degrees of freedom. In this thesis, we will consider two specific qubit designs. The first one is the *transmon* qubit, consisting in a charge qubit shunted by a large capacitance [55]. The transmon qubit boasts protection from dephasing noise induced by charge fluctuations, thanks to its nearly-flat charge dispersion relation. The second one is the flux qubit, that can be galvanically connected to TLR. This specific design allows to reach extreme values of the inductive coupling strength, breaching into the USC regime [26]. In circuit QED setups, artificial atoms can be controlled and measured [56] by means of microwave drivings sent through the cavity they are embedded in. Quantum nondemolition measurement can also be performed[57], via dispersive coupling of a superconducting qubit with a TLR.

In quantum computing tasks, circuit QED currently boasts the most advanced implementation of digital simulations [58, 59]. The long awaited demonstration of the dynamical Casimir effect has been finally achieved [60], exploiting the tunability of superconducting devices. Confinement in the one-dimensional media provided by TLR allows to radically increase the cross section in scattering experiments [61]. The scalability of lithographically printed circuits will soon allow the manufacturing of large bidimensional arrays of resonators [62]. Concluding, the possibility of implementing novel regimes of light-matter interaction, like multimode strong coupling [63] or tunable diamagnetic term [64], shows that the revolution introduced by circuit QED has only just begun.

1.2.2 Trapped ions

Discrete bosonic modes interacting with two-level quantum systems can also be implemented using ions trapped in time-dependent magnetic potentials [13]. In this case, the

bosonic mode is given by the oscillations of the ion inside the trap, while the qubit is provided by internal optical or hyperfine transitions of the ion itself. The motional mode can be cooled down to its ground state via sideband cooling [65]. Effective interaction between internal electronic states and the ion motion can be induced by laser drivings, whose tunable intensities establish the coupling strengths. Measurement of the electronic state can be done via fluorescence techniques [66], while other observables can be obtained in an indirect way, mapping the expected value on internal transitions [67].

Trapped ions are well known for the impressive precision achieved in state preparation, read-out and control [68], made possible by the developing of laser technology and optical detection techniques. Thanks to the weak interaction of the ion electronic transitions with the environment, trapped ion qubits have long coherence times, ranging from milliseconds up to seconds [69]. Single-qubit gates can be implemented by addressing electronic transitions with laser drivings, while two-photon gates are realized [70] using the motional degrees of freedom as a quantum bus to mediate interactions between distant ions. Also a version of this method robust to thermal noise has been developed [71]. These features make trapped ions a promising platform for the implementation of digital quantum simulations [72, 73].

Of specific interest for the present Thesis is the possibility of using trapped ions to implement chains of interacting spin systems. The use of collective motional modes [74] of ion chains made possible to experimentally study spin-spin interaction, including few [75] or hundreds [76] of ions. Disparate complex quantum phenomena have been explored using trapped-ion setups, like Ising spin frustration [77], quantum phase transitions [78, 79] and the inhomogeneous Kibble-Zurek mechanism [80]. The controllability of interactions between spins and bosonic modes allowed also for the quantum simulation of relativistic effects [81–83].

Concluding, with the advent of superconducting qubits, trapped ions do not represent the prime candidate for the implementation of a universal quantum computer. Nevertheless, controllable experiments in trapped ions are close to overcome the maximum complexity of models approachable with classical numerical techniques. Hence, this platform may soon serve as a specific task quantum computer. Besides practical applications, trapped ions will undoubtedly represent a compelling scientific tool for many years to come.

1.2.3 Ultracold atoms

The field of ultracold atoms consists in the manipulation of atomic clouds, typically at temperatures of the order of tenths of μK, where quantum mechanical effects become

dominant. Such low temperatures are achieved by means of magneto-optical trapping, laser cooling and evaporative cooling. The achievement of Bose-Einstein condensation (BEC) [84–86] and Fermi degeneracy [87–89] brought a revolution to atomic physics, shifting the focus from single atom dynamics to particle statistics and many-body interactions. At the beginning, experimental efforts were aimed at the study of coherent matter waves in an interacting macroscopic system. Interesting example of phenomena associated with the existence of a macroscopic matter waves are the interference of overlapping BECs [90], long-range coherence [91] and quantized vortices [92].

Dilute quantum gases can effectively be described by a single-particle description [93, 94]. In this picture, weak interactions will introduce a potential proportional to the local density of atoms in the cloud. Allowing small fluctuations around this zeroth-order approximation results in a model of a weakly interacting Bose gas. In this framework, a number of basic many-body models have been implemented, and their characteristic properties have be quantitatively verified [95]. Two novel methods have significantly extended the range of physical phenomena accessible to ultracold atoms. The first one is the possibility of tuning the atom scattering lenght by Feshbach resonances [96]. This technique allows to tune the coupling strength of the effective many-body system, making use of magnetic fields or collective optical drivings. The second one consists in the use of strong harmonic or periodic optical potentials, in order to confine the atomic cloud to lower dimensionalities or to load it on periodic lattices [97]. These developments allowed ultracold atoms to break the regime dominated by non-interacting quasi particles, paving the way for the study of strongly correlated quantum systems [98].

The high versatility of cold atoms allows for the implementation of a broad variety of models [99]. For example, in one-dimensional systems, microscopic properties of Luttinger liquids [100] or the spin-boson model [101] can be studied. Many important many-body systems, like spin models, can be realized as a limit of the Hubbard model in specific regimes [102]. Spin systems with high momentum [103], strong dipolar interactions [104] and many-body entanglement [105] can also be implemented. In disordered systems, the interplay of localization and repulsive interactions can be analyzed [106, 107], as well as the origin of ordering in spin glasses [108]. Fundamental theories for high-energy and condensed-matter physics can also be studied by means of synthetic gauge lattices [109]. Of specific interest for the preset Thesis, relativistic effects have also been implemented in atomic systems [110]. Concluding, ultracold atoms represent the most interesting platform for the direct implementation of complex many-body system.

1.3 In this Thesis

In this Thesis, we theoretically analyze a variety of phenomena related to light-matter interaction in the ultrastrong coupling regime. In particular, we focus on models that can be implemented with current technology, or that can inspire the development of existing quantum platforms. As the USC regime has been finally observed only recently, we believe that this standpoint is very timely. Our work aims at stimulating the close interplay between experimental and theoretical research that characterized the rapid development of quantum information and quantum technologies research areas.

This thesis is composed of two parts, each one containing three chapters, and various appendices. The first part is devoted to the study of USC-related phenomena in circuit QED, which is the most promising platform where the USC regime can be naturally achieved. In the second part, we consider atomic systems, namely trapped ions and ultracold atoms, where the physics of light-matter interaction in the USC regime can emerge as the result of Hamiltonian engineering.

I **Ultrastrong coupling regime in circuit quantum electrodynamics**

In this part, we analyze the modifications that the USC regime induces on fundamental quantum dynamical processes, like excitation transport or entanglement generation. We consider specific systems that can be implemented in circuit QED, namely, arrays of resonators interacting with superconducting qubits. We take into account technical and intrinsic issues of controlling devices working in the USC regime, and we design circuit architectures that exploit the specific advantages of this quantum platform, like the high tunability of system parameters.

In chapter 2, we consider excitation transfer in a linear array of three quantum cavities interrupted by an impurity, namely, a qubit interacting with the central resonator. In particular, we analyze how the probability of observing transfer is modified in the crossover between the SC and the USC regime. Indeed, our approach enables us to derive an operational definition of the SC-USC transition.

In chapter 3, we show first that the fast modulation of electrical boundary conditions can be used as a tool to generate entanglement among superconducting qubits, in complex arrays of quantum resonators. Then, we generalize this analysis to include the USC regime, where the mode structure of the electromagnetic field is strongly modified by the interaction with the qubit. In this case, we show that the anharmonicity of the spectrum enables us to restrict the dynamics to a low-energy subspace, where maximally entangled states of USC polaritons can be generated. However, the lack of techniques for measuring qubit-cavity system in

the USC regime would limit our capability of experimentally verifying the preparation of such entangled states.

In order to solve this issue, in chapter 4, we propose a feasible method to perform state engineering and tomography of a cavity-qubit system in the USC regime. Usually, measurements on superconducting qubits are implemented by decoupling the relevant qubit from the rest of the system in order to allow for dispersive read-out. However, in the USC regime decoupling is extremely challenging. Our proposal consists in a protocol to measure and control polaritonic excitations using an auxiliary qubit, requiring minimal resources and circumventing the decoupling issue.

II **Ultrastrong coupling regime in atomic systems**

In this part, we show how the physics of light-matter interactions in the USC regime can be effectively reproduced and observed in atomic systems, even if the natural coupling strengths are way too small to enter such a regime. This endeavor is interesting from different perspectives. From one side, the reproduction of complex phenomena in controllable quantum systems represents a resource for quantum simulations, where experiments in the quantum regime are engineered to retrieve information about quantum mechanical models which are intractable with classical numerical simulations. Then, the application of fundamental models, derived from first principles to describe specific interactions, as phenomenological descriptions for different systems, creates links between different research areas, facilitating the transfer of ideas and techniques. Finally, the implementation of models in unusual physical systems allows to explore different regimes and, in general, to exploit the specific features of the chosen platform.

In chapter 5, we propose a feasible scheme for simulating the quantum Rabi model in trapped ions, using current technology. Our method makes use of laser drivings to tailor effective interactions which resemble the quantum Rabi model in a specific interaction picture. The possibility of modifying the detuning between the laser drivings results in the complete tunability of physical parameters, in such a way that the QRM can be implemented in all relevant regimes.

Using similar techniques, in chapter 6, we show that two-photon interactions of a $N-$qubit chain coupled to a single bosonic mode can also be feasibly implemented in trapped ions, for all parameter regimes. The resulting models are dubbed two-photon Rabi for $N = 1$ and two-photon Dicke for $N > 1$. The interest in these models is motivated by novel, counterintuitive spectral features that are expected to appear only in the USC regime which, so far, has never been observed for this kind of models.

Finally, in chapter 7, we propose a method to reproduce the physics of the quantum Rabi model using a cloud of ultracold atoms. In this implementation, the bosonic mode is given by harmonic oscillations of the atoms in a quadratic trap, whereas the qubit is effectively introduced by a periodic potential that induces coupling between different bands. The proposed scheme allows to explore the USC and DSC regimes, and to generalize the quantum Rabi model to a periodic phase space. The predicted collapse and revivals of the initial state could be experimentally observed, in a platform that allows to efficiently track the time evolution of the momentum distribution.

III **Appendix**

In Appendix A, we provide further details about state transfer in three-cavity arrays. In Appendix B, we report the circuit quantization for the model discussed in chapter 3. In Appendix C, we provide details about two-step processes for state engineering in the USC regime. In Appendix D, we discuss some mathematical properties of the two-photon quantum Rabi model, and we describe a method to measure parity in the proposed trapped-ion implementation of the model.

Part I

Ultrastrong coupling regime in circuit quantum electrodynamics

Chapter 2

Photon transfer in ultrastrongly coupled three-cavity arrays

2.1 Introduction

The high level of control achieved on quantum optical systems [18, 69, 111, 112] motivated an increasing interest in the study of strongly correlated systems and collective phenomena. Particularly promising are arrays of coupled resonators, where cavities can interact with single two-level systems. These platforms are the best candidates to implement highly non-trivial photon lattice models, like the Jaynes-Cummings-Hubbard model [113–115], among others. The possibility of designing different geometries enables one to engineer quantum networks for distributed quantum information processing [116]. These lattice models have also proved useful to describe the scattering of a single-photon interacting with a qubit in a one-dimensional waveguide [117, 118].

A similar approach has been used to consider homogeneously coupled cavity arrays [119], where the central cavity-qubit interaction is in the strong coupling regime. However, reaching the ultrastrong coupling regime of light-matter interaction has important consequences in the collective properties of strongly correlated systems. Photon-scattering properties have been studied [120] only recently for the case in which the rotating-wave approximation (RWA) ceases to be valid. Circuit QED technologies [47–49] represent the most natural platform both to implement photon lattice models [62, 121, 122] and to reach the USC regime [25, 26, 28]. Networks of microwave resonators offer a high degree of tunability and scalability, but they also include disorder in the cavity coupling distribution due to fabrication imperfections.

In this chapter, we consider the problem of photon transfer in a linear array of three coupled cavities, where a two-level system interacts at the central site in the SC and USC regimes (see Fig. 2.1). This configuration can be thought as a microwave analogue [123] of the superconducting Josephson interferometer. We also include disorder in the cavity-cavity coupling, thus mimicking experimental imperfections. Under these conditions, we are able to unveil the following features: (i) in the SC regime, and for finite values of the hopping amplitudes and of the cavity-qubit coupling, a single excitation initially localized in the leftmost cavity is strictly forbidden to fully populate the rightmost cavity, similar to the delocalization-localization phenomenon [124]; (ii) in the USC regime, the above restriction does not hold any more, and a single excitation can fully populate the rightmost cavity for almost arbitrary Hamiltonian parameters. Furthermore, the tunneling rate of the single excitation becomes negligible for a critical value of the cavity-qubit coupling strength, and it also allows an operational way of defining the SC/USC crossover. Our scheme represents a feasible building block [62, 121, 122, 125] to study photon excitation and state transfer towards scalable cavity arrays.

The present chapter is organized as follows. In section 2.2, we introduce the model and we provide a description of the dynamical processes we consider. In section 2.3, we analyze the single-photon transfer in the SC regime. In section 2.4, we begin with a discussion on the system dynamics in the case in which the RWA breaks down, before moving on to a comparison of the photon transfer behavior between the SC and USC regimes. Further details on the transfer of a more general state (such as a qubit and a coherent state) are provided in Appendix A. In section 2.5, we report on a particular regime in which the qubit frequency vanishes. Finally, in section 2.6, we summarize and discuss our results.

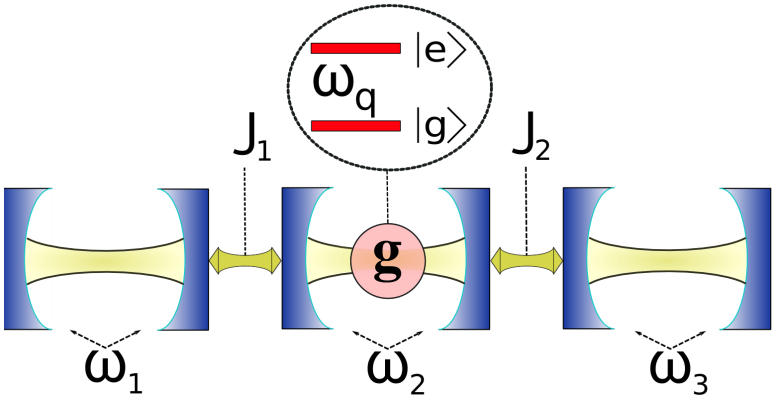

FIGURE 2.1: Linear chain of three microwave cavities. The central cavity is coupled to a two-level quantum system in the strong coupling or ultrastrong coupling regime. The side cavities are linked to the central one through hopping interaction that can also be strong enough to invalidate the RWA.

2.2 The model

Our model consists of an array of three single-mode cavities, where the central site interacts with a two-level system in the SC or in the USC regime. A schematic representation is shown in Fig. 2.1 where each cavity is linked with its neighbor through a hopping interaction that, in general, is not weak enough to consider the RWA. The corresponding Hamiltonian reads

$$\begin{aligned} H &= \sum_{\ell=1}^{3} \omega_\ell a_\ell^\dagger a_\ell + \frac{\omega_q}{2}\sigma_z + g\sigma_x(a_2^\dagger + a_2) \\ &- \sum_{\ell=1}^{2} J_\ell(a_\ell^\dagger a_{\ell+1} + a_\ell^\dagger a_{\ell+1}^\dagger + \text{H.c.}), \end{aligned} \tag{2.1}$$

where $a_\ell(a_\ell^\dagger)$ is the annihilation (creation) operator for photons on the ℓ-th cavity ($\ell = 1, 2, 3$), ω_ℓ being the characteristic frequencies and J_ℓ are nearest-neighbor hopping amplitudes. The qubit of frequency ω_q is located inside the central cavity and is described by the Pauli matrices σ_α ($\alpha = x, y, z$), while g denotes the cavity-qubit coupling strength. The complexity of the Hamiltonian in Eq. (2.1) is associated with the appearance of counter-rotating terms in the cavity-qubit and cavity-cavity interaction. Hereafter, we consider identical cavities ($\omega_\ell = \omega$) and resonant qubit ($\omega_q = \omega$). We stress that in all simulations we set the energy scales in units of the resonator frequency ω.

The system is initialized in the state $|\psi_0\rangle = |100\rangle \otimes |\text{g}\rangle$, corresponding to having a single photon in the leftmost cavity, zero in the others, and the qubit in its ground state. We address the dynamics dictated by the Hamiltonian (2.1), and study the single-excitation transfer along our three-cavity array. Depending on the ratio g/ω, two regimes can be identified: the SC regime for $g/\omega \lesssim 0.1$, and the USC regime for $0.1 \lesssim g/\omega \lesssim 1$.

2.3 Single-photon transfer in strong coupling regime

When $g/\omega \ll 1$, the RWA provides a faithful description of the cavity-qubit dynamics, so that we can neglect the counter-rotating terms in Eq. (2.1): $\sigma_x(a_2^\dagger + a_2) \to (\sigma_+ a_2 + \sigma_- a_2^\dagger)$. In the regime where hoppings $J_l/\omega \ll 1$, the cavity-cavity RWA also holds, and the $U(1)$ symmetry provides the conservation of the total number of excitations. In this case, the time-evolution of the system will necessarily lead to a state of the form $|\psi(t)\rangle = \alpha\,|000\rangle \otimes |\text{e}\rangle + \big(\beta\,|100\rangle + \gamma\,|010\rangle + \delta\,|001\rangle\big) \otimes |\text{g}\rangle$. A full analytical solution can be found in the interaction picture and directly solving the Schrödinger equation. At resonance, where qubit and resonator frequencies coincide ($\omega_q = \omega$), we can derive explicitly the probability amplitude for finding a photon in the rightmost cavity: $\delta(t) = T\left[\cos(\lambda t) - 1\right]/2$, where

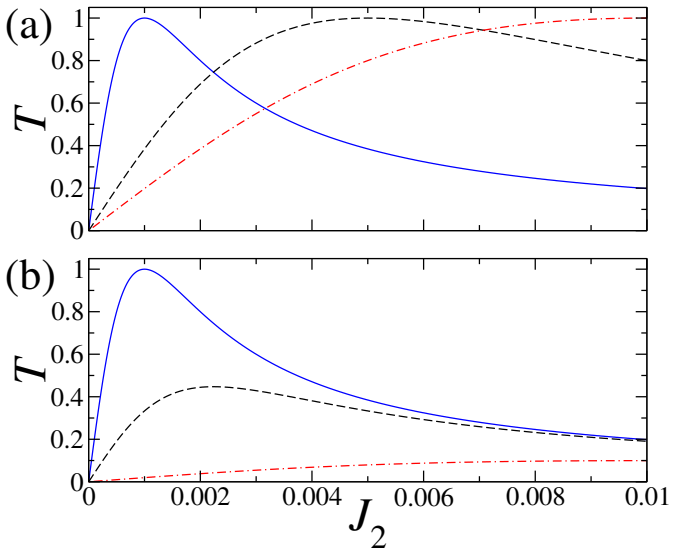

FIGURE 2.2: Oscillation amplitude T defined in Eq. (2.2) as function of the hopping parameter J_2, and for different sets of Hamiltonian parameters. In panel (a), for a fixed value of the cavity-qubit coupling $g = 0$, we display data for $J_1 = 0.001$ (continuous blue line), $J_1 = 0.005$ (dashed black line), and $J_1 = 0.01$ (dot-dashed red line). In panel (b), for a fixed value of $J_1 = 0.001$, we consider $g = 0$ (continuous blue line), $g = 0.002$ (dashed black line), and $g = 0.01$ (dot-dashed red line). Here and in the following figures, we express all the couplings/hoppings in units of ω, while times are denoted in units of ω^{-1} . We also set $\hbar = 1$.

$\lambda = \sqrt{g^2 + J_1^2 + J_2^2}$ and the amplitude reads

$$T = \frac{2J_1 J_2}{g^2 + J_1^2 + J_2^2}. \tag{2.2}$$

The above result unveils a competition between cavity-cavity and cavity-qubit interactions. Equation (2.2) indeed shows that, introducing disorder in the cavity-cavity couplings ($J_1 \neq J_2$), the single-photon transfer has a counter-intuitive dependence on the hopping terms. In particular, for given parameters g, ω, and J_1, the excitation transfer to the rightmost cavity exhibits a non-monotonic behavior with increasing J_2 and is maximum for $J_1 = J_2$ (see Fig. 2.2a). Note that only in the homogeneous case ($J_1 = J_2$) and for a negligible cavity-qubit coupling g, it is possible to have photon transfer with unit probability. On the other hand, for any finite value of g, the latter is strictly forbidden. We also notice that, in Eq. (2.2) and for fixed J_1, increasing g decreases the amplitude T (see Fig. 2.2b). This behavior has a simple explanation: when a single excitation tries to move from the left to the central cavity, it is scattered back by the cavity-qubit system without being fully absorbed. In fact, the probability for exciting the qubit $|\alpha|^2$ is inversely proportional to the square of the coupling strength.

2.4 Single-photon transfer in the USC regime

If the coupling strength g and the resonator frequency ω satisfy $0.1 \lesssim g/\omega \lesssim 1$, the system enters the USC regime. In this case, photons are spontaneously generated from the vacuum such that the total number of excitations grows with the ratio g/ω, enlarging unavoidably the associated Hilbert space[1]. To observe an appreciable excitation transfer, the photon hopping strength must be of the same order of g, thus we consider values up to $J_\ell \sim 0.1$. In this regime, for the sake of consistency, the counter-rotating terms of the cavity-cavity interaction have been taken into account, although they do not change qualitatively the system dynamics. In order to provide a reliable system real-time dynamics, we performed a fourth order-Trotter expansion[2] of the evolution operator [126]. To extend this kind of analysis to a higher number of cavities, one should rely on more sophisticated numerical techniques, such as the time-evolving block-decimation scheme for a one-dimensional array of cavities.

2.4.1 System dynamics

Figure 2.3 shows the time-evolution of the average photon number in each cavity, $N_{\rm ph}^{(i)}(t) = \langle\psi(t)|a_i^\dagger a_i|\psi(t)\rangle$, starting from the state $|\psi_0\rangle = |100\rangle \otimes |{\rm g}\rangle$ that evolves according to Hamiltonian (2.1). At first glance, one recognizes a highly irregular behavior of $N_{\rm ph}^{(i)}(t)$, which arises from the counter-rotating terms in the cavity-qubit interaction. Remarkably, this is developed by the unitary evolution of the system itself, and it is not due to the limited time-resolution of our simulations. In order to quantify this behavior, we analyse the fractal dimension of $N_{\rm ph}^{(1)}(t)$ by using the modified box counting algorithm [127]. This consists in dividing the total time interval in segments of size τ, and then covering the data with a set of rectangular boxes of size $\tau \times \Delta_i$ (Δ_i is the largest excursion of the curve in the i-th region τ). One then computes the average excursion $M(\tau) = \sum_i \Delta_i/\tau$. The dimension $\mathcal{D}$ of the curve is defined by $\mathcal{D} = -\log_\tau M(\tau)$. One finds $\mathcal{D} = 1$ for a straight line, and $\mathcal{D} = 2$ for a periodic curve. Indeed, for times much larger than the period, a periodic curve uniformly covers a rectangular region. Any value of $\mathcal{D}$ between these integer values entails the fractality of the curve (see caption of Fig. 2.3). In the case of Fig. 2.3a, we obtained $\mathcal{D} \approx 1.66$ (inset to the figure). Furthermore, increasing g, we found a fractal dimension which rapidly decreases from $\mathcal{D} \sim 2$

[1] The counter-rotating terms in the cavity-cavity coupling also induce photon generation from the vacuum. However, for the cases we consider ($J_\ell \lesssim g$) most of the non-conserving excitation effects come from the cavity-qubit USC regime.

[2] In order to keep the Hilbert space dimension manageable in our simulations, we cut the maximum number of allowed photons per cavity to a finite amount $N_{\rm max} = 18$. We checked that such cutoff value induces an error that is negligible on the scale of our results, for $g/\omega \lesssim 1$. All Trotter time evolutions have been performed up to a time $t = 5000$.

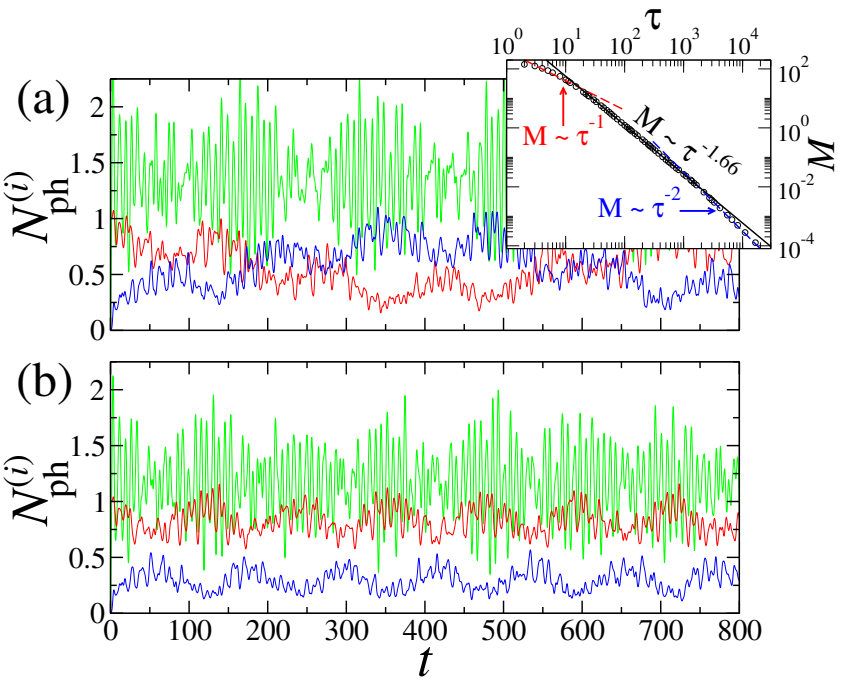

FIGURE 2.3: Average photon number in each cavity $N_{\rm ph}^{(i)}(t)$ at resonance condition (ω_q=ω), and for homogeneous cavity-cavity couplings (J_1=J_2=0.1). The red line stands for the leftmost cavity, the blue line for the rightmost cavity, while the green line for the central cavity. The main panels refer to different cavity-qubit couplings: $g = 0.9$ (a), $g = 0.85$ (b). The inset shows the box counting analysis for $N_{\rm ph}^{(1)}(t)$ ($g = 0.9$), and displays M as a function of τ. For any curve, there exists a region of box lengths $\tau_{\rm min} < \tau < \tau_{\rm max}$ where $M \propto \tau^{\mathcal{D}}$. Outside this region, one either finds $\mathcal{D} = 1$ or $\mathcal{D} = 2$. The first equality holds for $\tau < \tau_{\rm min}$, and it is due to the coarse grain artificially introduced by numerical simulations. The second one is obtained for $\tau > \tau_{\rm max}$ and it is due to the finite length of the analyzed time series. The boundaries $\tau_{\rm min}$, $\tau_{\rm max}$ have to be chosen properly for any time series. A power-law fit of the intermediate region gives a fractal dimension $\mathcal{D} \approx 1.66$. Time is expressed in units of ω^{-1}.

(quasi-periodic curve) down to non integer values close to $\mathcal{D} \sim 1.5$ for large cavity-qubit couplings.

The fractal time-dependence emerging in the system is clearly due to the presence of counter-rotating terms. Here we point out that a similar analysis, performed after removing the two side-cavities from the model, systematically produced integer values of $\mathcal{D}$. This means that the Rabi model alone is not sufficient to generate a fractal signal. In order to have a sufficient number of incommensurate frequencies generating a fractal behavior, the Rabi model has to be combined with some non trivial interaction with other bosonic modes.

2.4.2 Photon transfer

Before discussing the transfer properties, it is appropriate to observe that, even though in the USC regime photons are spontaneously generated in the central site, for the

coupling values considered here and if the system is initialized in the vacuum state, the average photon number in the side-cavities keeps being way smaller than 0.1 during the whole evolution. This guarantees that the signal tunneled through the central site can be clearly distinguished from excitations generated by the presence of counter-rotating terms. Furthermore, in the case of homogeneous cavity-cavity couplings, given the symmetry of the system Hamiltonian (2.1), the two side-cavities have identical behavior and differences between them can arise only from asymmetrical initial states.

Two fundamental differences with respect to the SC regime can be found in the excitation transfer analysis. First, in the USC regime a single photon excitation can be completely transferred from the leftmost to the rightmost cavity, also for a finite value of the coupling strength g [see, *e.g.*, Fig. 2.3a]. This is the typical situation for almost arbitrary Hamiltonian parameters in the USC regime, a disparity that can be explained as follows. The initial state $|\psi_0\rangle$ has a finite overlap with the state $|E\rangle = (g\,|100\rangle \otimes |\mathrm{g}\rangle + J\,|000\rangle \otimes |\mathrm{e}\rangle)/\sqrt{g^2+J^2}$. In the SC regime, $|E\rangle$ is an Hamiltonian eigenstate, and its overlap with the evolved system state $|\psi(t)\rangle$ is conserved during the time-evolution. Consequently, the state $|001\rangle \otimes |\mathrm{g}\rangle$ is not accessible (as far as $g \neq 0$). On the other hand, in the USC regime the state $|E\rangle$ is no longer an eigenstate of the Hamiltonian. Hence, the previous limitation does not hold anymore, and complete transfer to the rightmost cavity is generally allowed. In the USC regime, the qubit and the field in the central cavity cannot be considered as separated entities, and the Jaynes-Cummings doublets are not the correct eigenstates to describe the system dynamics. In fact, the system eigenstates are defined in two infinite-dimensional Hilbert spaces that have a defined parity $p = \pm 1$, according to the Z_2 symmetry [19].

The second feature to be highlighted is that the photon transfer is strongly inhibited for a specific value of the cavity-qubit coupling strength, as displayed in Fig. 2.3b. In particular, in Fig. 2.4 we analyzed the population inversion time T_{inv}, defined as the time in which the average photon number becomes bigger in the rightmost cavity than in the leftmost cavity, as a function of the coupling strength g, and for different values of the cavity-cavity coupling strength. We found that there exists a critical value g_c, dependent on the system parameters, for which the time needed to observe single-photon transfer dramatically increases. For the considered parameter ranges, we find a critical coupling $0.78 \lesssim g_c \lesssim 0.88$ (in units of ω). Fixing $J_1 = 0.1$, we found $g_c \approx 0.94 - 0.97 \times J_2$, while the population inversion time $T_{\mathrm{inv}}^{(\mathrm{max})}$ in correspondence to such value exhibits a quite irregular pattern of oscillations with J_2 (inset to Fig. 2.4). To our knowledge, this is the first observation of this behavior in the excitation transfer properties of a cavity QED system. This phenomenon is specific to the USC dynamics and occurs in the *higher-coupling region* of the Rabi model ($g/\omega \gtrsim 0.4$) [128], a zone where the photon

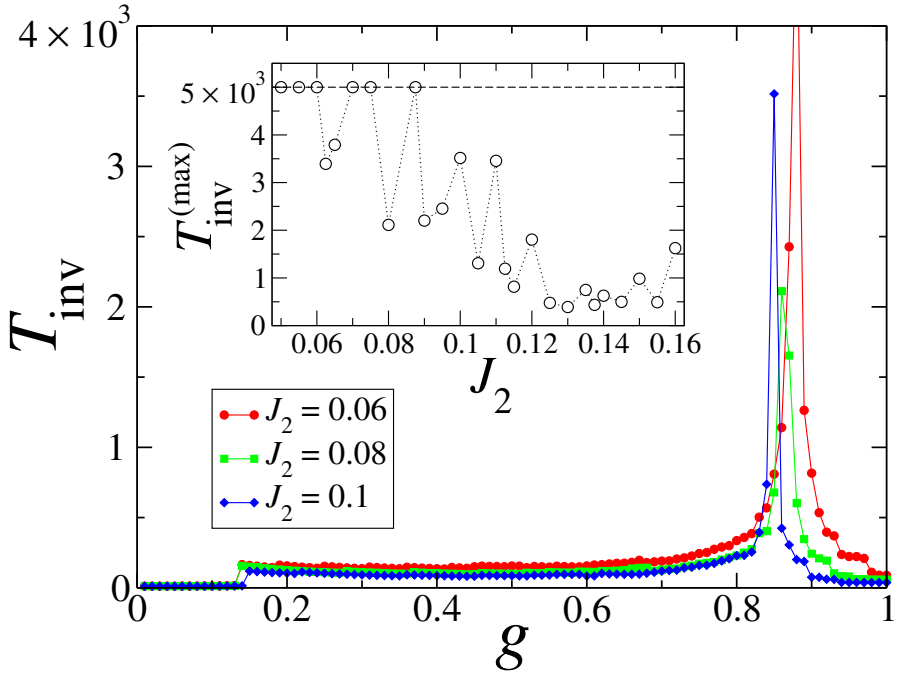

FIGURE 2.4: Population inversion time $T_{\rm inv}$ as a function of the cavity-qubit coupling constant, for $J_1 = 0.1$, defined as the time in which $N_{\rm ph}^{(3)}(t)$ becomes bigger than $N_{\rm ph}^{(1)}(t)$. We note the SC-USC transition for $g \approx 0.14$, and the inhibition of state transfer around a critical value g_c which depends on the hopping term J_2 according to: $g_c \approx 0.94 - 0.97 \times J_2$. The couplings g and $J_{1,2}$ are expressed in units of ω, as well as $T_{\rm inv}$ is in units of ω^{-1}. The inset displays the maximum value of the population inversion time $T_{\rm inv}^{(\rm max)}$ that is reached at g_c, as a function of J_2.

production exceeds the RWA predictions, and an analytical treatment becomes difficult despite the integrability of the model [19].

We highlight the sudden increase of $T_{\rm inv}$ occurring in the *lower-coupling region* of the Rabi model, which is zoomed-in in Fig. 2.5. This abrupt behavior is due to the SC/USC regime crossover. If the RWA holds, the population inversion time is given by: $T_{\rm inv} = \arccos(1-\lambda^2/(J_1^2+J_2^2))/\lambda$, where λ has been defined previously. For $g > \sqrt{J_1^2+J_2^2}$, the population inversion never occurs. Contrariwise, when the counter-rotating terms are taken into account, we observe population inversion at finite time also for larger value of the coupling g. Notice that the location of the discontinuities appearing in Fig. 5 is related to our definition for the inversion time $T_{\rm inv}$. For example, a redefinition of $T_{\rm inv}$ as the time in which $N_{\rm ph}^{(3)}/3$ becomes bigger than $2\,N_{\rm ph}^{(1)}/3$, would quantitatively change the value of g for which the inversion time experiences a discontinuity. However the emerging physics would not qualitatively change. Here we use the most natural definition of $T_{\rm inv}$, in analogy with the concept of population inversion in statistical mechanics. The sudden increase of the population inversion time is due to the fact that, in the USC regime, the accessible part of the Hilbert space is unbounded, because of the $U(1)$ symmetry breaking down to a $\mathbb{Z}_2$ symmetry. Hence, the system can explore

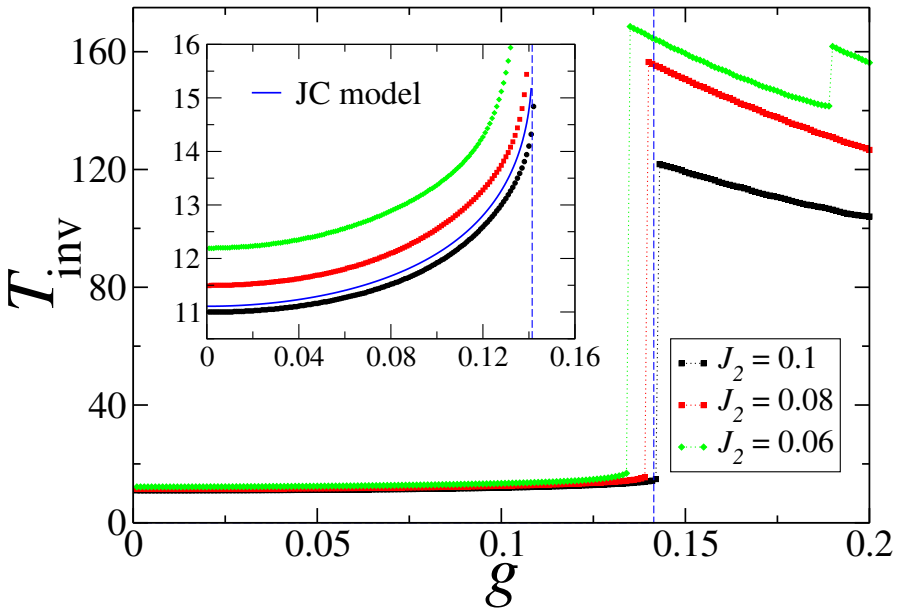

FIGURE 2.5: Population inversion time T_{inv} (in units of ω^{-1}) as a function of the cavity-qubit coupling constant g , and for fixed value $J_1 = 0.1$. The blue and the black lines correspond to the homogeneous case. The blue line corresponds to the analytical solution when the RWA holds for cavity-cavity and cavity-qubit interaction. The black, red and green lines are obtained through numerical simulations of the full model ruled by the Hamiltonian (2.1).

a much bigger number of states: complete transfer is allowed, but the probability of its occurrence is smaller. For our three-cavity array, the parameter $g_t = g/\sqrt{J_1^2 + J_2^2}$ provides us with an operational definition for the SC/USC transition of the cavity-qubit interaction. For small values of g_t, the RWA describes correctly the transfer dynamics. When $g_t > 1$, the full model behavior differs quantitatively and qualitatively from the JC model predictions. We observe also that varying J_2 with respect to J_1 results in a longer population inversion time: in both regimes, inhomogeneity in the hopping terms hinders the excitation transfer.

We have also analyzed the transfer of coherent states, $|\phi_0\rangle$=$|\alpha\rangle$, and of arbitrary linear superposition states $|\phi_0\rangle = p\,|0\rangle + e^{i\theta}\sqrt{1-p^2}\,|1\rangle$, with p randomly chosen in the interval [0,1]. We numerically simulated the system evolution, setting $|\psi_0\rangle = |\phi_0\rangle\,|0\rangle\,|0\rangle\,|\mathrm{g}\rangle$ as initial state, and we recorded the behavior of the transfer fidelity, defined as: $F = \mathrm{Tr}[\rho_0\rho(t)]$, where $\rho_0 = |\phi_0\rangle\langle\phi_0|$ and $\rho(t)$ is the state of the rightmost cavity at time t. The results we found are consistent with those relative to the case of single-excitation transfer. The interplay between the hopping constant J and the cavity-qubit coupling strength g, rules the state transfer dynamics: with increasing J the transfer is more likely to happen, while increasing g results in smaller values of the transfer fidelity. Specifically, in the SC regime, as far as $g \neq 0$, it is impossible to observe complete state transfer, i.e. $F < 1$ at any time. This is not the case in the USC regime, where the transfer fidelity, be in a linear superposition or a coherent state, can be close to unity,

also when g and J are of the same order. These results show the peculiar features of state transfer physics beyond the RWA, and may pave the way for developing a general theory in presence of USC regimes. Further details on state transfer features can be found in appendix A.

2.5 Degenerate qubit case

In the case in which the qubit frequency vanishes, a closed analytical solution of the system dynamics is available if we consider the RWA in the cavity-cavity interaction. This model can be simulated with current technology by means of a coupled cavity-qubit system in the SC regime, and the application of a strong classical driving to the qubit [129, 130]. It can be shown that the dynamics of such system will be ruled by the effective Hamiltonian

$$H_{\rm eff} = \omega \sum_{\ell=1}^{3} a_\ell^\dagger a_\ell + \frac{g}{2}\sigma_x(a_2^\dagger + a_2) - \sum_{\ell=1}^{2} J_\ell(a_\ell^\dagger a_{\ell+1} + \text{H.c.})\,. \tag{2.3}$$

which can be obtained setting $\omega_q = 0$ in Eq. (2.1), and performing the RWA on the cavity-cavity interaction. In this case, the excitation transfer exhibits a smooth periodic behavior in time, which is independent of the cavity-qubit coupling strength, and allows a complete transfer at regular times. In fact, the time evolution of the difference between the average photon number in the leftmost and rightmost cavities, starting from the initial state $|\psi_0\rangle$=$|100\rangle \otimes |\mathrm{g}\rangle$ in the homogeneous case, reads

$$\Delta N_{\rm ph}(t) = N_{\rm ph}^{(1)}(t) - N_{\rm ph}^{(3)}(t) = \cos(\sqrt{2}Jt). \tag{2.4}$$

This result holds both in the SC and in the USC regime, hence the counter-rotating terms do not modify the excitation transfer properties of the system. We point out that, when $g/\omega \gtrsim 0.1$, spontaneous photon generation occurs: $\langle a_1^\dagger a_1\rangle$ and $\langle a_3^\dagger a_3\rangle$ keep a chaotic time dependence, despite their difference follows a smooth and regular behavior.

2.6 Conclusions

In this chapter, we have studied excitation transfer in an array of three coupled cavities, where a two-level system interacts with the central one, focusing on the comparison between strong and ultrastrong coupling regimes of light-matter interaction. In the SC regime, the cavity-qubit interaction g and the cavity-cavity inhomogeneities $J_1 \neq J_2$ constrain the excitation transfer, thus inhibiting complete population tunneling. On

the contrary, in the USC regime a much richer scenario appears. A complete photon transfer is generally allowed, even for finite values of the cavity-qubit coupling strength and for inhomogeneous hoppings, although there exists a specific regime for which the tunneling rate becomes negligible. The complexity of the USC dynamics, generated by counter-rotating terms, manifests itself in the highly irregular time pattern of the observables, exhibiting a fractal behavior. Nonetheless, the physics beyond the RWA plays an important role for the enhancement of quantum state transfer. Finally, in the degenerate qubit case, the excitation transfer is regular and its period does not depend on the cavity-qubit coupling strength.

The proposed scheme can be implemented with state-of-the-art superconducting circuit technology. Such a controllable system could be used as building block for realizing controllable quantum simulation of large lattices involving the quantum Rabi model in all coupling regimes. We also remark that, studying the photon transport mechanism in coupled cavities, as for example our three-cavity setup, in the presence of losses could be also relevant for the understanding of noise-assisted transport in quantum networks [131, 132].

Chapter 3

Dynamical Casimir effect entangles artificial atoms

3.1 Introduction

In this chapter, we investigate how to generate multipartite entangled states of two-level systems, also referred to as quantum bits (qubits), by means of varying boundary conditions. We also propose a scheme that could be feasibly implemented in the framework of superconducting circuits with nowadays technology. For pedagogical reasons, we illustrate our model with a hypothetical quantum-optical system, shown in Fig. 3.1. It is composed of two cavities, independently coupled to single qubits, sharing a partially reflecting mirror. Fast modulation of the mirror properties generates squeezed light, a phenomenon known as dynamical Casimir effect (DCE).

We consider the cavity-qubit coupling strength in the strong and ultrastrong coupling regimes. In the SC case, we introduce the key concepts allowing the generation of highly-entangled two-qubit states, also known as Bell states [133], in circuit QED [47–49]. Furthermore, we consider the generation of tripartite entanglement [134] and the scalability aspects of our proposal to multipartite systems. In the USC regime, we show that the strong anharmonicity allows to restrict the system dynamics to a low-energy subspace, so that Bell-states of USC polaritons can be generated.

Before going on, we provide a brief introduction to the dynamical Casimir effect, in particular related to recent implementations in circuit quantum electrodynamics.

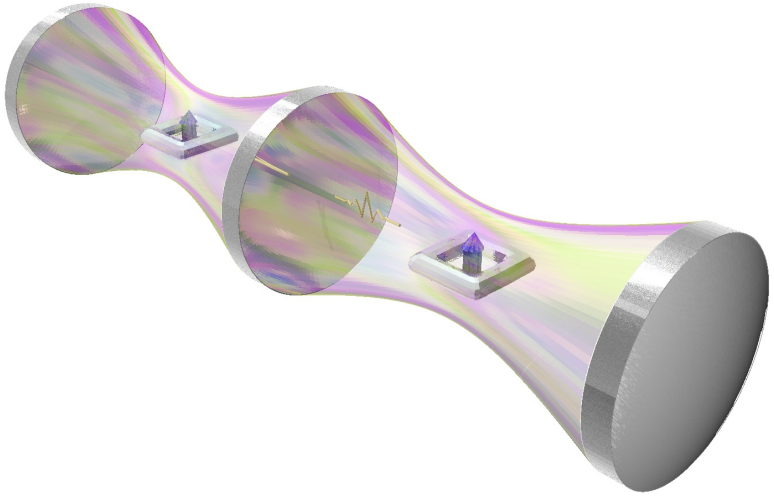

FIGURE 3.1: Quantum optical implementation of the model of Eq. (3.1): two cavities with a common partially-reflecting mirror, each one containing a two-level artificial atom in the strong-coupling regime. If the position and/or transmission coefficient of the central mirror is time-modulated, correlated photon pairs are generated and entanglement is transferred to qubits via the Jaynes-Cummings interaction.

3.1.1 The dynamical Casimir effect in superconducting circuits

The phenomenon of quantum fluctuations, consisting in virtual particles emerging from vacuum, is central to understanding important effects in nature—for instance, the Lamb shift of atomic spectra [135] and the anomalous magnetic moment of the electron [136]. The appearance of a vacuum-mediated force between two perfectly conducting plates, known as the Casimir effect, is caused by a reduction of the density of electromagnetic modes imposed by the boundary conditions [137–139]. This leads to a vacuum radiation pressure between the mirrors that is lower than the pressure outside. It was also suggested [140] that a mirror undergoing relativistic motion could convert virtual into real photons. This phenomenon, denominated dynamical Casimir effect (DCE), has been observed in recent experiments with superconducting circuits [60, 141]. In the same manner that the Casimir effect can be understood as a mismatch of vacuum modes in space, the kinetic counterpart can be explained as a mismatch of vacuum modes in time.

A moving mirror modifies the mode structure of the electromagnetic vacuum. If the mirror velocity, v, is much smaller than the speed of light, c, then the electromagnetic modes adiabatically adapt to the changes and no excitations occur. Otherwise, if the mirror experiences relativistic motion, changes occur nonadiabatically and the field can be excited out of the vacuum, generating real photons. Beyond its fundamental interest, it has been pointed out that the DCE provides a mechanism to generate quantum correlations [142–148]. In this sense, we may consider the study of the DCE as a resource for quantum networks and quantum simulations, in the frame of quantum technologies. In circuit quantum electrodynamics, DCE photons have been created

by modifying the boundary conditions of the electromagnetic field [60] confined in a one-dimensional medium. In a similar experiment photons have also been created by modulating the effective speed of light [141] in a Josephson metamaterial.

This chapter is organized as follows. In section 3.2, we introduce the model with a quantum-optical analogy. In section 3.3, we show how such a model can be implemented using superconducting circuit technology. In section 3.4, we theoretically demonstrate that, using the proposed protocol, it is possible to generate bipartite Bell states. In section 3.5, we show that our framework can be generalized to the multipartite case. In section 3.6, we extend the model to the USC regime. Finally, in section 3.7, we provide some comments over the scope and over possible promising extensions of our research work.

3.2 The model: a quantum-optical analogy

The Hamiltonian describing the system of Fig. 3.1 is composed of the sum of two Jaynes-Cummings (JC) interactions and a time-dependent coupling between the field quadratures,

$$\begin{aligned} \mathcal{H} &= \hbar \sum_{\ell=1}^{2} \left[\omega_\ell a_\ell^\dagger a_\ell + \frac{\omega_\ell^q}{2} \sigma_\ell^z + g_\ell \left(\sigma_\ell^+ a_\ell + \sigma_\ell^- a_\ell^\dagger \right) \right] \\ &+ \hbar \alpha(t) \left(a_1^\dagger + a_1 \right) \left(a_2^\dagger + a_2 \right). \end{aligned} \tag{3.1}$$

Here, $a_\ell^\dagger$, a_ℓ are the creation and annihilation operators of the bosonic modes representing the cavity fields, while σ_ℓ^z, $\sigma_\ell^\pm$ are the Pauli operators of qubits. The characteristic frequencies of the two cavities are denoted by ω_ℓ, while the qubit energies are ω_ℓ^q. The parameters g_ℓ and $\alpha(t)$ denote the cavity-qubit and cavity-cavity interaction strength, respectively.

In Eq. (3.1), the coupling between different cavity modes, due to the overlap of their spatial distribution, is written in its full form without performing the rotating wave approximation. While in optical cavities this overlap can be obtained with a partially reflecting mirror [149], in circuit QED it is commonly implemented using capacitors or inductances shared by two or more resonators. The boundary condition at the edge shared by the cavities is ruled by the central mirror position and by its reflection coefficient. Modulating these physical quantities results in a time dependence of the cavity frequencies ω_i and of the coupling parameter α. When the effective cavity length is oscillating with small deviations from its average value, we can still consider the system as a single-mode resonator. In particular, if the cavity-cavity coupling parameter is a

time-dependent function, $\alpha(t) = \alpha_0 \cos(\omega_d t)$ with $\omega_d = \omega_1 + \omega_2$ and $\alpha_0/\omega_i \ll 1$, the interaction effectively turns into a two-mode squeezing term (see below),

$$\alpha(t) X_1 X_2 \to \frac{\alpha_0}{2} \left(a_1^\dagger a_2^\dagger + a_1 a_2 \right), \tag{3.2}$$

which generates pairs of entangled photons shared by the cavities. By means of the Jaynes-Cummings interaction, entanglement generated between cavities may be transferred to resonant qubits. In fact, we will prove below that, under suitably designed conditions, maximal entanglement (Bell state) between the two qubits may be attained.

3.3 Circuit QED implementation

Nowadays, quantum technologies [150] offer several platforms to study fundamentals and applications of quantum theory. In particular, superconducting circuit technology [151, 152] is a prime candidate to implement the model of Eq. (3.1). In this framework, the cavities are constituted by coplanar waveguides, working at cryogenic temperatures, that are described by an equivalent LC circuit, as shown in Fig. 3.2a,b. The characteristic frequency of such devices is in the $2 - 10$ GHz microwave regime. Each cavity can be coupled to a superconducting qubit built from Josephson junctions (JJs) to access charge [51], flux [53], or phase [153] degrees of freedom. Specifically, we propose the use of transmon qubits which have low sensitivity to charge noise and coherence times well above ten μs [55, 154, 155]. The moving mirror [156, 157] that couples both cavities (see Fig. 3.1) can be implemented by means of a superconducting quantum interference device (SQUID) [158], which behaves as a tunable inductance. A SQUID is composed of a superconducting loop interrupted by two JJs (see Fig. 3.2a), threaded by an external flux ϕ_{ext}. The latter allows a fast modulation of the electrical boundary condition of cavities and their interaction. Notice that a modulation of the magnetic flux threading the SQUID induces a proportional variation of the effective resonator lengths, while in the system of Fig. 3.1, moving the central mirror results in an opposite change of cavity lengths.

By using off-the-shelf electronics, it is possible to produce magnetic fluxes that oscillate at the cavity characteristic frequencies. The upper limit to the speed of modulation is imposed by the SQUID plasma frequency, defined as $\omega_p = \frac{1}{\hbar}\sqrt{8E_C E_J}$, where E_C is the charging energy, E_J the Josephson energy, both associated with a single JJ belonging to the superconducting loop. Beyond this frequency, the internal degrees of freedom of the device are activated and a more complex behavior appears. To overcome this problem, the external flux $\phi_{\text{ext}}(t)$ injected into the device, which also determines E_J, will be composed of the sum of a signal oscillating at the driving frequency ω_d and a constant

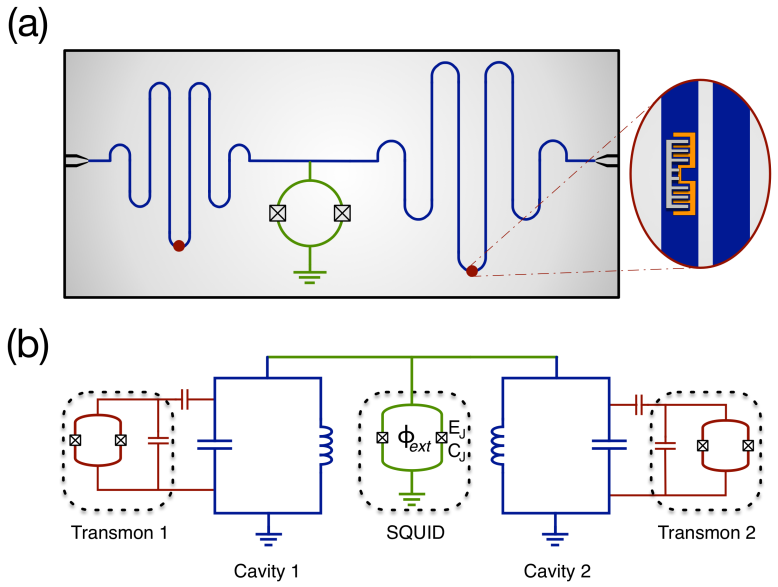

FIGURE 3.2: (a) The model of Fig. 3.1 can be implemented by means of two coplanar waveguides, grounded through a SQUID, containing two superconducting qubits. The blue lines represent two parallel strip lines of isolating material, where the superconducting region between them constitutes the coplanar waveguide. Each cavity interacts with a transmon qubit that is denoted by a red dot. Different resonator lengths result in distinct resonator frequencies. (b) Circuit diagram for the previous scheme, where the cavities are effectively represented by LC resonators. We assume two identical Josephson junctions of the SQUID, while transmon qubits are constituted by two Josephson junctions shunted by a large capacitance.

offset ϕ_0, $\phi_{\rm ext}(t) = \phi_0 + \Delta\phi\cos(\omega_d t)$. We consider nondegenerate resonators to avoid uncorrelated photon generation at the cavity resonance frequencies, an assumption that has been confirmed by a detailed quantum mechanical analysis (see appendix B) of the effective lumped circuit element in Fig. 3.2b.

If the instantaneous resonant frequency of a given resonator follows the time-dependence $\omega(t) = \omega_0 + \delta\omega\cos(\omega_d t)$, cavity modes are well defined only under the condition $\delta\omega \ll \omega_0$. In our proposal, the frequencies of the cavity modes are obtained by solving the transcendental equation $kd\tan(kd) = L/L_s - C_s/C(kd)^2$ for the wave number k, where d is the length of the resonator. We called C_s, L_s and C, L the effective capacitance and inductance of the SQUID and of the resonator, respectively. Parameters used in our simulations assure that $\delta\omega/\omega_0 < 10^{-3}$.

In the interaction picture, the parametric processes induced by the SQUID lead to the Hamiltonian

$$\begin{aligned}\mathcal{H}_{\rm d}^I(t) &= \hbar\cos(\phi_{\rm ext}/\varphi_0)\Big[\sum_{\ell=1}^{2}\alpha_\ell(a_\ell e^{-i\omega_\ell t} + a_\ell^\dagger e^{i\omega_\ell t})^2 \\ &- \hbar\tilde{\alpha}(a_1 e^{-i\omega_1 t} + a_1^\dagger e^{i\omega_1 t})(a_2 e^{-i\omega_2 t} + a_2^\dagger e^{i\omega_2 t})\Big], \qquad (3.3)\end{aligned}$$

where $\varphi_0 = \hbar/2e$ is the reduced flux quantum, and the coefficients α_ℓ and $\tilde{\alpha}$ are functions of the Josephson energy (E_J), the junction capacitance (C_J), the cavity parameters such as capacitance (C_ℓ) and inductance (L_ℓ). If the parameters α_ℓ and $\tilde{\alpha}$ are much smaller than cavity frequencies ω_ℓ, we can perform the rotating wave approximation (RWA), and so neglect fast-oscillating terms in Eq. (3.3). In this case, if we consider $\phi_{\text{ext}} = \phi_0 + \Delta\phi \cos(\omega_d t)$ with $\Delta\phi$ a small flux amplitude, the controlling the driving frequency ω_d allows to selectively activate interaction terms in the system dynamics. When the cavity is off-resonant and $\omega_d = \omega_1 + \omega_2$, the interaction Hamiltonian reads as Eq. (3.2). Interactions among different cavity modes, called mode mixing, are activated under the frequency-matching condition $\omega_d = \omega_a - \omega_b$. Cavity and driving frequencies can be chosen in order to make the relevant mode interact only with off-resonance, overdamped modes. Circuit design allows each qubit to be resonantly coupled with a single cavity mode, in which activation of higher modes due to the DCE mechanism can be neglected.

3.4 Bipartite entanglement generation

Our protocol for generating entanglement requires neither direct [159] nor single cavity-bus mediated [160] qubit-qubit interaction. Instead, it consists in cooling down the system to its ground state, turning on the external driving flux ϕ_{ext} and switching it off at time t_{SO}, when the maximal qubit entanglement is reached. The *concurrence* $\mathcal{C}$ is an entanglement monotone of a given bipartite mixed state ρ, namely, the minimum average entanglement of an ensemble of pure states that represents ρ. For an arbitrary two-qubit state the concurrence reads [161] $\mathcal{C}(\rho) = \max\{0, \lambda_1 - \lambda_2 - \lambda_3 - \lambda_4\}$, where λ_i are the eigenvalues, in decreasing order, of the Hermitian matrix $R = \sqrt{\sqrt{\rho}\tilde{\rho}\sqrt{\rho}}$, with $\tilde{\rho} = \sigma_y \otimes \sigma_y \rho^* \sigma_y \otimes \sigma_y$.

The numerical results are shown in Fig. 3.3a. An almost maximally entangled state ($\mathcal{C} = 0.97$) can be reached within $t_{SO} \approx 10 - 500$ ns, that is, for a wide range of realistic system parameters (see appendix B). Such protocol allows generation of the Bell state $|\psi\rangle = (|ee\rangle + i|gg\rangle)/\sqrt{2}$ with fidelity $\mathcal{F} = |\langle\psi|\rho|\psi\rangle| = 0.99$, with current superconducting circuits technology. The density matrix of the produced Bell state is shown in Fig. 3.3b. We have also proven that entanglement generation is robust against small imperfections due to limited fabrication precision and imperfect ground state preparation. Our protocol can be implemented in an on-chip architecture and it does not require any external source of squeezed signals [162].

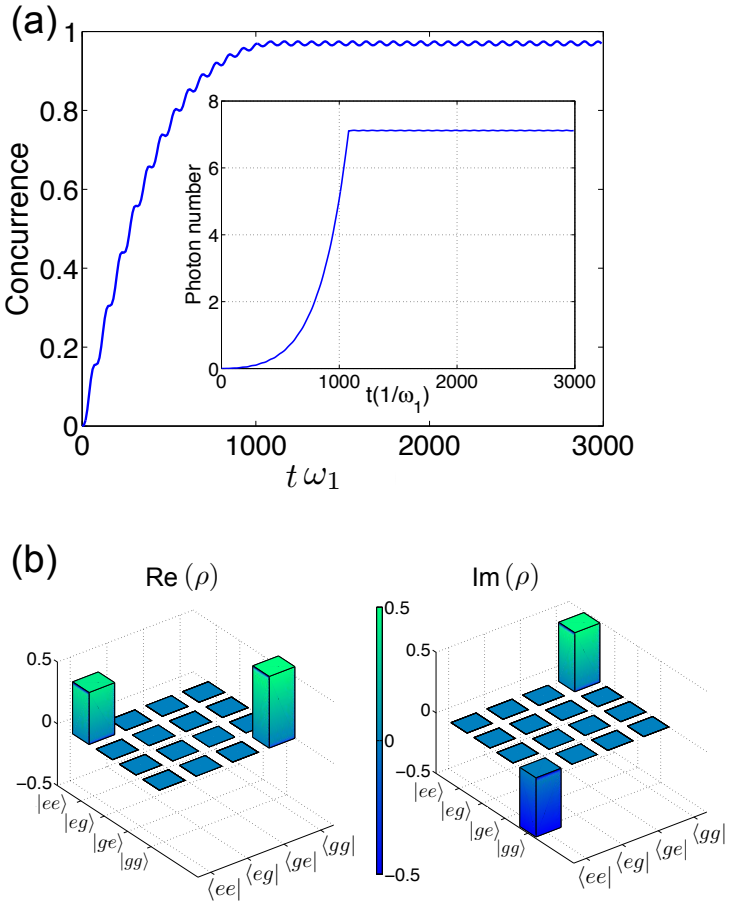

FIGURE 3.3: (a) Concurrence and mean photon number as a function of time in units of the cavity frequency ω_1. Here, the chosen parameters are: $\omega_1/2\pi = 4$ GHz, $\omega_2/2\pi = 5$ GHz, the impedance for both cavities is $Z_0 = 50\Omega$, and the critical current of the SQUID junctions is $I_C = 1.1$ μA. Such parameters result in a squeezing parameter $\alpha_0 = \omega_1 \times 10^{-3}$. Each qubit is resonant with its corresponding cavity and they are coupled with the same interaction strength $g = 0.04\ \omega_2$. (b) Real and imaginary parts of the density matrix ρ associated with the two-qubit system.

3.5 Generalization to multipartite systems

In the framework of superconducting circuits, resonators can be linked together in unidimensional and bidimensional arrays to build networks of quantum cavities and superconducting devices. This enables us to envision more complex configurations which generalize the concept of dynamical Casimir effect to the multipartite case. Let us consider three resonators connected to the ground via a SQUID, as shown in Fig. 3.4. By injecting a fast-oscillating magnetic flux through the SQUID results in varying boundary conditions, which generate correlated photons pairs distributed in the three cavity modes. Such a configuration has no direct analogy with optical cavities, as opposed to the bipartite case. The Hamiltonian that describes the circuit of Fig. 3.4 is composed of three JC interactions and three time-dependent direct couplings between the field

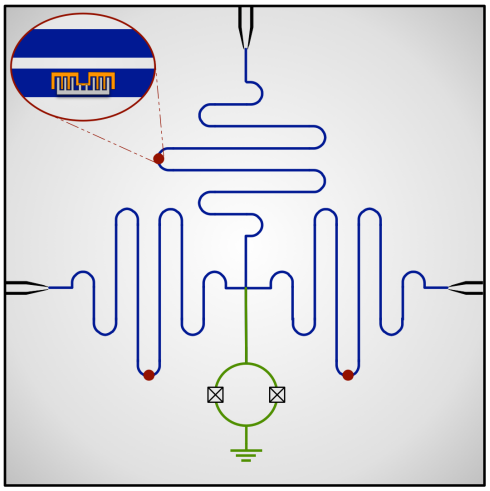

FIGURE 3.4: Three coplanar waveguide resonators are connected to the ground through a SQUID. Each resonator is coupled with a resonant transmon qubit. This scheme allows generation of GHZ-like entangled states, through a first-order process. By using this circuit design as a building-block, it is possible to explore more complex configurations and to build scalable cavity networks (see Appendix B).

quadratures of each resonator pair

$$\begin{aligned} \mathcal{H} &= \hbar \sum_{\ell=1}^{3} \left[\omega_\ell a_\ell^\dagger a_\ell + \frac{\omega_\ell^q}{2} \sigma_\ell^z + g_\ell \left(\sigma_\ell^+ a_\ell + \sigma_\ell^- a_\ell^\dagger \right) \right] \\ &+ \hbar \sum_{\langle \ell, m \rangle} \alpha_{\ell m}(t) \left(a_\ell^\dagger + a_\ell \right) \left(a_m^\dagger + a_m \right). \end{aligned} \tag{3.4}$$

If the external flux threading the SQUID is composed of three signals oscillating at the frequencies $\omega_{\ell m}^d = \omega_\ell + \omega_m$, we can isolate the two-mode squeezing terms as in Eq. (3.2).

Generating multipartite entanglement is a challenging task, since it requires multi-qubit gates whose operation fidelity is considerably lower than the single- or two-qubit gates.Here we show that our protocol allows generation of genuine multipartite entanglement (GME). With GME, we refer to quantum correlations which cannot be described using mixtures of bipartite entangled states alone.The negativity [163] is an entanglement monotone that estimates the bipartite entanglement shared between two subsystems of any possible bipartition, it ranges from zero for separable to 1/2 for maximally entangled states. It is defined as $\mathcal{N}(\rho) = \frac{||\rho^{T_A}||_1 - 1}{2}$ where $||\rho^{T_A}||_1$ is the trace-norm of the partial transpose of the bipartite mixed state ρ. Numerical results on the negativity, shown in Fig. 3.5a, indicate the generation of highly entangled states of three qubits. Figure 3.5b shows the average photon number in each cavity. In order to prove that such state is not biseparable, we evaluate an entanglement monotone that detects only multipartite quantum correlations, called genuine multipartite entanglement

(GME) concurrence $\mathcal{C}_{GME}$. It is obtained after an optimization process over all decomposable witnesses $W = P + Q^{T_A}$, where P and Q are positive semidefinite [164, 165]. Our results, $\max(\mathcal{C}_{\mathrm{GME}}) \approx 0.3$, confirm the existence of genuine multipartite entanglement.

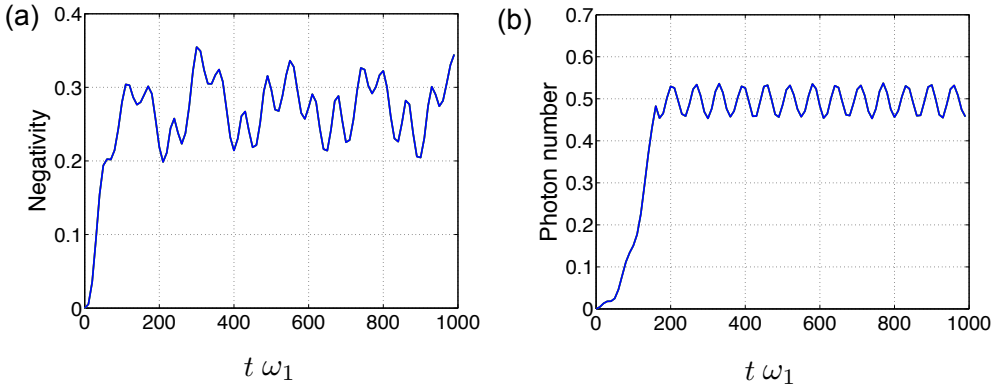

FIGURE 3.5: (a) Negativity of the bipartite system obtained isolating one qubit from the set of the other two, as a function of time. Here, we considered resonator frequencies of $\omega_1/2\pi = 3.8$ GHz, $\omega_2/2\pi = 5.1$ GHz and $\omega_3/2\pi = 7.5$ GHz. The SQUID is identical to the bipartite case and we use resonant qubits. The coupling parameters are homogeneous and their bare value is given by $\alpha_0 = 5\ \omega_1 \times 10^{-3}$. (b) Average photon number in each cavity as a function of time. Due to the symmetric configuration the photon distribution is the same for the three cavities.

Finally, to identify the entanglement class of three-qubit states, we make use of the entanglement witness [166] $\mathcal{W}_{\mathrm{GHZ}} = 3/4\ \mathbb{I} - P_{\mathrm{GHZ}}$, where $P_{\mathrm{GHZ}} = |\mathrm{GHZ}\rangle\langle\mathrm{GHZ}|$. Negative values for $\mathrm{Tr}\left[\rho\mathcal{W}_{\mathrm{GHZ}}\right]$ imply that for any decomposition $\rho = \sum_j p_j\rho_j$ at least one ρ_j is a GHZ state, and so ρ belongs to the GHZ class. Local operations do not change the entanglement class, it means the witness can be optimized by minimizing $\mathrm{Tr}\left[F\rho F^\dagger\mathcal{W}_{\mathrm{GHZ}}\right]$, where $F = F_1 \otimes F_2 \otimes F_3$, and F_i are arbitrary single-qubit SLOCC operations. We obtained $\mathcal{W}_{\mathrm{GHZ}} = -0.06$, proving generation of (mixed) GHZ-like states, which belong to the most general entanglement class [134].

3.6 Ultrastrong coupling regime

So far, we have considered values of the coupling strength g small enough to perform the rotating wave approximation, and so to use the Jaynes-Cummings model to describe the qubit-field interaction. In this section, we analyze how the proposed circuit implementation can be used to generate maximally entangled states of polaritons, in the case in which the coupling g is comparable with the cavities bare frequencies.

We consider the Hamiltonian of Eq. (3.1), in the bipartite case, considering the full quantum Rabi model for the qubit-field coupling. For the sake of clarity, we label the two qubit-cavity systems with the letters a and b, as well as the corresponding ladder

operators a, $a^\dagger$ and b, $b^\dagger$. The system Hamiltonian can be then written as

$$H = H_R^a + H_R^b + \alpha(t)\left(a + a^\dagger\right)\left(b + b^\dagger\right) + \frac{\alpha(t)}{2}\left[\left(a + a^\dagger\right)^2 + \left(b + b^\dagger\right)^2\right], \tag{3.5}$$

where H_R^a and H_R^b are quantum Rabi Hamiltonians,

$$H_R^a = \omega_a a^\dagger a + \frac{\omega_a}{2}\sigma_z^a + g\sigma_x^a\left(a + a^\dagger\right), \tag{3.6}$$

and similarly for system b. As in section 3.2, we define $\alpha(t) = \alpha_0 \cos(\omega_d t)$. We anticipate that, in this case, we will tune ω_d to be resonant with polaritonic transitions, while in the SC regime the optimal frequency-matching condition corresponds to resonance with the bare cavities.

We will rewrite now the system Hamiltonian in the polariton basis, *i.e.* in the basis of the eigenvectors of the uncoupled Rabi models, $H_R^{a/b}\left|\psi_i^{a/b}\right\rangle = E_i^{a/b}\left|\psi_i^{a/b}\right\rangle$. Let us consider the interaction terms individually. The field quadratures can be rewritten as

$$\left(a + a^\dagger\right) = \sum_{i,j}\left(A_{i,j} + A_{j,i}^*\right)\left|\psi_i^a\right\rangle\left\langle\psi_j^a\right|, \quad \text{where} \qquad A_{i,j} = \left\langle\psi_i^a\right| a \left|\psi_j^a\right\rangle. \tag{3.7}$$

In the same way, we define $B_{i,j} = \left\langle\psi_i^b\right| b \left|\psi_j^b\right\rangle$. Let us show that the single-mode squeezing terms $\left(a + a^\dagger\right) = a^2 + {a^\dagger}^2 + 2a^\dagger a + 1$ have no effect for the specific dynamics here considered. We are interested in transitions between the ground and the first excited states, which have always opposite parity $\Pi = -\sigma_z e^{i\pi a^\dagger a}$ (which corresponds to a discrete $\mathbb{Z}_2$ symmetry of the system). Given that a^2 leaves the parity Π of a given state untouched[1], we know that $\left\langle\psi_i\right| a^2 \left|\psi_j\right\rangle = 0$ for any pair of states with different parity. Clearly, the same holds for $a^\dagger$. This means that, as opposite to the SC case [167], discussed in previous chapters of the present chapter, we do not need to consider off-resonant resonators in order to remove the single-mode squeezing terms. The terms $a^\dagger a$ and $b^\dagger b$ are diagonal in the basis of Rabi eigenvectors, hence they will carry no time-dependency in the interaction picture and they can be neglected via rotating wave approximation (RWA), given that they have a fast-oscillating prefactor $\alpha(t)$.

The Hamiltonian of Eq. (3.5) can be then rewritten as

$$H = \sum_i E_i^a \left|\psi_i^a\right\rangle\left\langle\psi_i^a\right| + \sum_i E_i^b \left|\psi_i^b\right\rangle\left\langle\psi_i^b\right| \tag{3.8}$$

$$+ \alpha(t)\sum_{i,j}\sum_{\mu,\nu}\left(A_{i,j} + A_{j,i}^*\right)\left(B_{\mu,\nu} + B_{\nu,\mu}^*\right)\left|\psi_i^a\right\rangle\left\langle\psi_j^a\right| \otimes \left|\psi_i^b\right\rangle\left\langle\psi_j^b\right|, \tag{3.9}$$

[1]For an extended discussion on parity conservation in the USC regime, see chapter 4 and Appendix B.1.

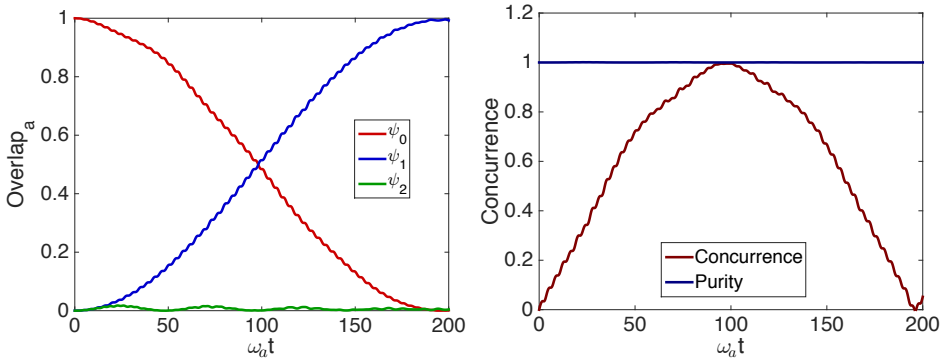

FIGURE 3.6: (On the left) Projection of the system state over the first three eigenvectors of H_R^a, over evolution time. Only the ground and the first excited states are appreciably involved in the system dynamics. (On the right) Concurrence and purity of the effective two-qubit state obtained by restricting us to consider the ground and the first excited states of each local Rabi model. The system parameters of the individual systems are $\omega_a = 1$, $\omega_b = 2$, $g = 0.9$ (homogeneous coupling). The interaction strength is given by $\alpha_0 = 0.01$, and the driving frequency is chosen in order to make the interaction term resonant $\omega_d = \Delta^a + \Delta^b$, where $\Delta^{a/b} = E_2^{a/b} - E_1^{a/b}$.

or, switching to the interaction picture,

$$H_I = \alpha(t) \sum_{i,j} \sum_{\mu,\nu} \left(A_{i,j} + A_{j,i}^*\right) \left(B_{\mu,\nu} + B_{\nu,\mu}^*\right) |\psi_i^a\rangle \langle\psi_j^a| \otimes \left|\psi_i^b\right\rangle \left\langle\psi_j^b\right| \; e^{i\Delta_{i,j}^a t} \, e^{i\Delta_{\mu,\nu}^b}, \quad (3.10)$$

where $\Delta_{i,j}^{a/b} = E_i^{a/b} - E_j^{a/b}$ are the polariton energy splittings. Given that $\alpha(t) = \alpha_0 \cos(\omega_d t)$, where $\alpha_0 \ll \Delta_{i,j}$, choosing ω_d to be resonant with a given transition allows us to neglect the other ones via RWA. In particular, if we set $\omega_d = \Delta_{01}^a + \Delta_{01}^b$, we obtain

$$H_I = \frac{\alpha_0}{2} \left(A_{0,1} + A_{1,0}^*\right) \left(B_{0,1} + B_{1,0}^*\right) |\psi_0^a\rangle \langle\psi_1^a| \otimes \left|\psi_0^b\right\rangle \left\langle\psi_1^b\right| \; + \text{H. c.} \quad (3.11)$$

The simple form of the resulting Hamiltonian is due to the opposite parity of the ground and first-excited state, and to the strong anharmonicity of the USC regime. Assuming that the system can be initialized in its ground state $|\psi_0^a\rangle \left|\psi_0^b\right\rangle$, the evolution described by the interaction of Eq. (3.11) leads to the Bell state $\left(|\psi_0^a\rangle \left|\psi_0^b\right\rangle + |\psi_1^a\rangle \left|\psi_1^b\right\rangle\right)/\sqrt{2}$. The validity of the approximations made has been checked performing numerical simulations of the full model of Eq. (3.5). The results, displayed in Fig 3.6, show that unwanted transitions are safely off-resonant, and that a maximally entangled states between USC polaritons can be feasibly generated. However, the measurement of such a state is hindered by the lack of decoupling mechanisms in the USC regime. In order to solve this problem, in the following chapter 4, we will introduce a method that would allow to experimentally demonstrate that a USC polariton Bell state has been generated in a feasible experiment.

3.7 Conclusions and outlook

The theoretical analysis presented in this chapter shows that fast-oscillating boundary conditions can generate a maximum entangled state of two qubits, in a non trivial way. In the USC regime, effective two-level quantum systems are represented by USC polaritons, *i.e.*, hybrid qubit-field excitations. This results demonstrate that the dynamical Casimir effect (DCE) represents a valuable, so far overlooked resource for quantum information science. The implementation of quantum resonators ruled by fast-oscillating boundary conditions in superconducting circuits discloses the possibility of generalizing the dynamical Casimir physics to multipartite systems. Accordingly, we have theoretically proven that the DCE allows generation of three-qubit entangled states belonging to the GHZ class, i.e., to the most general class of genuine multipartite entanglement in the three-partite case.

Our proposal can be used as a building block to realize more complex circuit configurations, which exploit the dynamical Casimir physics in order to generate and distribute quantum correlations. Figure 3.7 shows two possible configurations of three-cavity setups: a linear array, box (a), and a triangular configuration, box (b). While in the multipartite configuration presented in Fig. 3.4, two-body interactions links all resonators pairwise, the schemes of figure 3.7 lead to first-neighbour couplings. The linear array is interesting since it can be easily scaled to higher number of resonators. The triangular configuration allows real-time control of the inhomogeneities in the couplings, due to the presence of three SQUIDs. Figure 3.8a shows a direct generalization of the three-partite scheme previously discussed, in which four cavities are involved. Such configuration is the most natural candidate to generate symmetric genuine multipartite entangled states of more artificial atoms. Finally, in figure 3.8b it can be found an example of a complex Casimir network, which shows the flexibility of the present proposal.

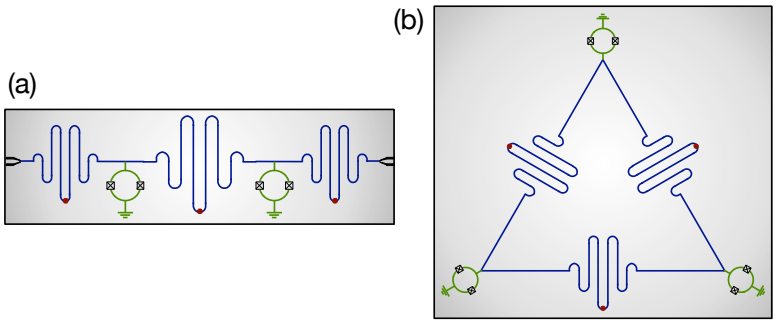

FIGURE 3.7: **Tripartite setups.** **a** Linear array of three resonators with near-neighbour couplings. **b** Three SQUIDs in a triangular configuration. In this case, it is possible to independently control pairwise interactions.

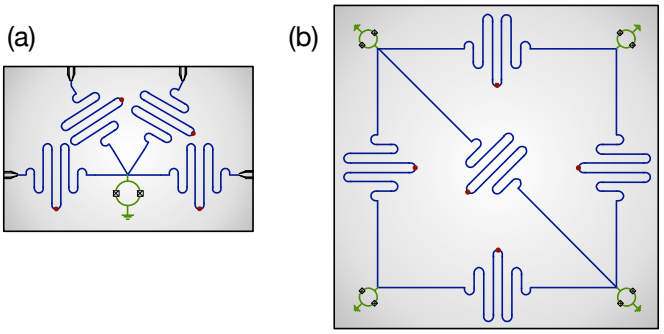

FIGURE 3.8: **Multipartite case.** Complex cavity configurations which apply the dynamical Casimir physics in order to implement highly-correlated quantum networks.

Chapter 4

Parity-dependent state engineering in the USC regime

4.1 Introduction

The fast-growing interest in the USC regime is motivated by theoretical predictions of novel fundamental properties [32, 33, 37–41, 167], and by potential applications in quantum computing tasks. Indeed, in previous chapters, we have shown how entering the USC regime can modify the excitation transfer and entanglement generation in arrays of quantum resonators. However, in order to experimentally analize fundamental processes, or to use USC systems as tools for QI processing, it is needed the same controllability that is available for SC systems.

Unfortunately, state reconstruction in the USC regime, as well as many quantum information applications, are hindered by the lack of *in situ* switchability and control of the cavity-qubit coupling strength. This difficulty is a consequence of the fact that, in the USC regime, the field and the two-level system merge into collective bound states called polaritons. Consequently, usual decoupling mechanisms applied in circuit and cavity QED to address individual subsystem do not work in the USC regime, as the coupling is so large that it provides a preferential interaction channel regardless of the induced frequency detuning.

The experimental certification of the achievement of the USC regime is also an open issue. Nowadays, quantum technologies featuring the USC regime have been able to characterize this coupling regime only by detecting deviations in transmission or reflection spectroscopy in measurements of optical/microwave signals [26, 28]. For the sake of completeness, we can say that direct Wigner function reconstruction of an anharmonic

oscillator has been realized [168], but only for a small anharmonicity. In the case of harmonic oscillators, microwave cavity field states have been measured using streaming Rydberg atoms as probes [169, 170].

In this chapter, we propose a method which makes use of an ancillary qubit as a tool for state generation, spectroscopy, and quantum state tomography of USC polariton states. We analyze a system composed of a single-mode quantum resonator coupled to two two-level systems, or qubits, as shown in Fig. 4.1. One of them, the system qubit, interacts with the cavity mode in the USC regime, forming polariton states, while the coupling strength of the ancillary qubit with the cavity is in the SC regime. Our analysis enables us to design a spectroscopy protocol able to identify the parity of each USC energy level, allowing us to check distinctive features of the USC spectrum in a realistic experiment.

Moreover, we show how the ancillary qubit allows for state engineering of the USC qubit-cavity system. From our analysis, it emerges that USC polaritons populating the system substantially modify the light-matter interaction of the ancillary qubit, leading to a counter-intuitive breaking of the Jaynes-Cummings model [17] even for small interaction strengths. Finally, the validity of our method has been checked by means of numerical simulations, performed considering realistic parameters of current implementations of circuit QED in the USC regime, where the present model may be implemented with state-of-the-art technology.

This chapter is organized as follows. In section 4.2, we introduce our model and we describe specific features of the spectrum and parity conservation of the quantum Rabi model, which are of particular interest for our method. In section 4.3, we analyze the dynamics of the proposed system. In section 4.4, we show how the proposed architecture can be used to perform quantum state tomography and state preparation. Finally, in section 4.5, we summarize the results discussed in this chapter.

4.2 The quantum Rabi model and an ancillary qubit.

The quantum Rabi model (QRM) [19, 171] describes the dipolar coupling of a two-level system and a single-mode cavity field, as described by the Hamiltonian

$$H_S = \hbar\omega_r a^\dagger a + \frac{\hbar\omega}{2}\sigma_z + \hbar g\sigma_x\left(a^\dagger + a\right), \tag{4.1}$$

where $a^\dagger(a)$ represents the creation(annihilation) operator of the cavity field, while σ_x and σ_z are Pauli operators defined in the qubit Hilbert space. We denote, in Eq. (4.1), the cavity mode frequency, ω_r, the qubit frequency spacing, ω, and the interaction

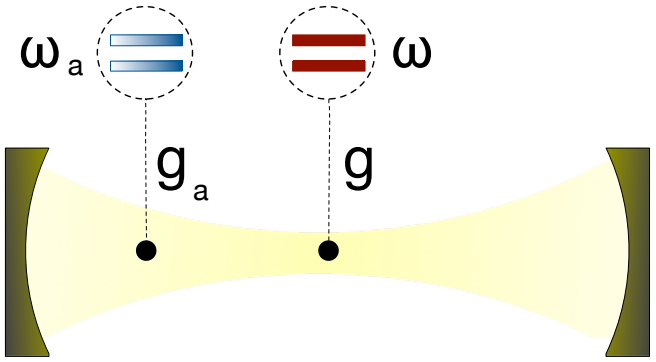

FIGURE 4.1: A single-mode quantum optical cavity interacts with a qubit (red, solid color) of frequency ω in the ultrastrong coupling regime. The coupling g is of the same order of the qubit and resonator frequencies. Another qubit (blue, shaded color) can be used as an ancillary system in order to measure and manipulate USC polariton states.

strength, g. If we restrict ourselves to near resonant interactions, $\omega \approx \omega_r$, depending on the parameter g/ω_r, two regimes can be identified: the SC regime for $g/\omega_r \ll 1$ and the USC regime for $0.1 \lesssim g/\omega_r \lesssim 1$. In the former, the Hamiltonian of Eq. (4.1) reduces to the celebrated Jaynes-Cummings model [17], where the conservation of the excitation number $\hat{N} = a^\dagger a + \sigma_z$ turns the model analytically solvable. On the contrary, in the USC regime, the field and the qubit merge into polariton states that feature a discrete symmetry Z_2, see Fig. 4.2. This symmetry is characterized by the parity operator $\hat{\Pi}_S = -\sigma_z \, e^{i\pi a^\dagger a}$, such that $\hat{\Pi}_S|\psi_j\rangle = \pm|\psi_j\rangle$ with $j = 0, \ldots, \infty$. Here, we denote $|\psi_j\rangle$ as polariton eigenstates of energy $\hbar\omega_j$. Furthermore, this parity symmetry turns the model solvable [19], and approximations exist in limiting cases, as is the case of the perturbative USC regime [172] and the deep strong coupling (DSC) regime [42, 173].

Here, we consider the QRM in the USC regime plus an ancillary qubit interacting with the cavity field,

$$H = H_S + H_A \ , \quad H_A = \frac{\hbar\omega_a}{2}\sigma_z^a + \hbar g_a \sigma_x^a \left(a^\dagger + a\right). \tag{4.2}$$

Later, we will assume that the frequency ω_a can be tuned in real time, a requirement that is fulfilled in most implementations with superconducting circuits [55, 174]. We set the ancilla-cavity field interaction g_a to be in the SC regime. However, counterintuitively, we will show that the presence of the USC system activates the counter-rotating terms of the ancilla $g_a\left(\sigma_-^a a + \sigma_+^a a^\dagger\right)$, even for small g_a/ω_r. Indeed, the relevance of the ancilla counter-rotating terms depends on the polariton eigenstate more than on the ratio g_a/ω_r, as long as the interaction between the ancillary qubit and the USC system is in the SC regime. Here, $\sigma_\pm^a = \left(\sigma_x^a \pm i\ \sigma_y^a\right)/2$ is the raising(lowering) operator of the ancilla.

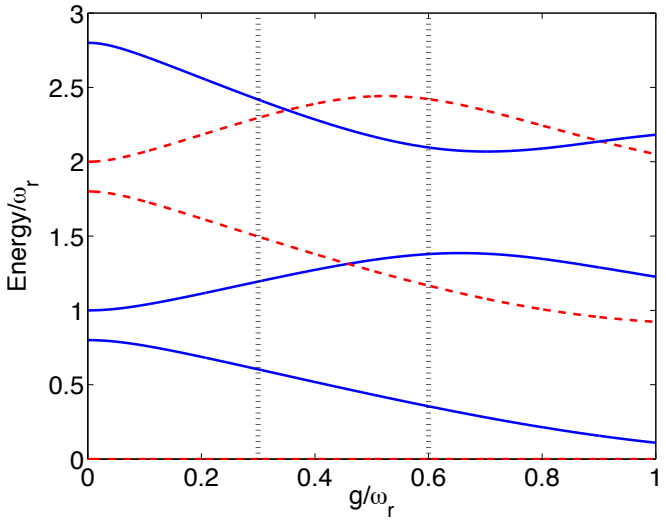

FIGURE 4.2: Energy levels of the quantum Rabi model as a function of the dimensionless parameter g/ω_r. We assume $\hbar = 1$. Parameter values are expressed in units of ω_r and we consider a detuned system qubit $\omega/\omega_r = 0.8$. Energies are rescaled in order to set the ground level to zero. The parity of the corresponding eigenstates is identified, blue continuous line for odd and red dashed lines for even states.

4.2.1 Full model spectrum

The spectrum of the full Hamiltonian (4.2) is shown in Fig. 4.3a (Fig. 4.3b) as a function of the ancilla frequency for $g/\omega_r = 0.3$ ($g/\omega_r = 0.6$), corresponding to the vertical lines displayed in Fig. 4.2. The total ancilla-system spectrum, associated to Hamiltonian H in Eq. (4.2), presents three main features. First, the system still preserves the Z_2 symmetry with the global parity operator $\hat{\Pi} = \sigma_z^a \otimes \sigma_z \; e^{i\pi a^\dagger a} = \hat{\Pi}_A \otimes \hat{\Pi}_S$. Notice that eigenstates with global parity $+1(-1)$ are represented by dashed-red(continuous-blue) lines in Figs. 4.3a and 4.3b. Second, introducing the ancillary qubit results in the splitting of the energy levels of polaritons. There are regions where the energy differences behave linearly with ω_a/ω_r, so the main contribution of the ancilla comes from its self-energy. This behavior can be explained if we consider the average value of the quadrature $\hat{X} = a + a^\dagger$ appearing in the cavity-ancilla interaction of Eq. (4.2). It vanishes for diagonal projections in the polariton basis, that is, $\langle\psi_j|\hat{X}|\psi_j\rangle = 0$ for $j = 0, \ldots, \infty$ (see Appendix C.1). Third, intersections between levels of different global parity subspaces show that those eigenstates are not coupled. On the contrary, avoided crossings between eigenenergies sharing the same global parity confirm that such states experience a direct coupling. In the following, we will show how this feature allows for selective state engineering of the USC polaritons.

In order to use the ancillary qubit as a tool to characterize and to measure polaritons in the USC regime, the ground state of the ancilla plus USC system must be separable. This condition is fulfilled as seen in Fig. 4.3c, where we show the purity $\mathcal{P} = \mathrm{Tr}\left\{\rho_a^2\right\}$ for

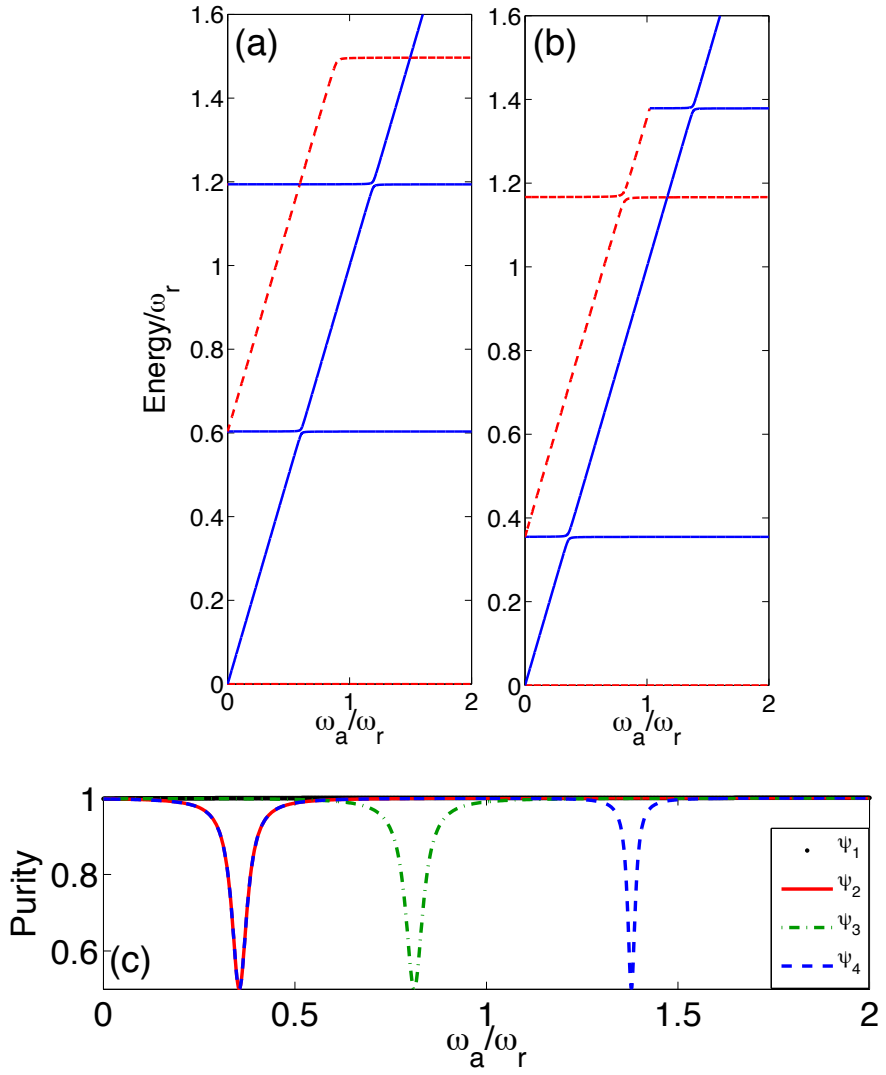

FIGURE 4.3: (a), (b) Energy levels of the full model of Eq. (4.2) as a function of the ancilla frequency ω_a. We assume $\hbar = 1$. For both (a) and (b), the USC qubit frequency is $\omega/\omega_r = 0.8$ and the ancilla-field cavity interaction strength is $g_a/\omega_r = 0.02$. The USC qubit coupling is $g/\omega_r = 0.3$ for (a) and $g/\omega_r = 0.6$ for (b). Energies are rescaled in order to set the ground level to zero. The global parity of the corresponding eigenstates is identified, blue continuous line for odd and red dashed lines for even states. (c) Purity $\mathcal{P}$ of the reduced density matrix of the ancillary qubit for different global system eigenstate, as a function of the ancilla frequency. For the ground state $|\psi_0\rangle$, $\mathcal{P}$ is always unity.

the ground and first excited states. We define the ancilla reduced density matrix as $\rho_a = \mathrm{Tr}_{\mathrm{polariton}}\{\rho\}$, where the partial trace runs over the USC system degrees of freedom. If $\mathcal{P} = 1$, the ancilla and the polariton are in a separable state. Contrariwise, in coincidence with avoided crossings in the spectrum, see Fig. 4.3a,b, the purity presents some dips for excited states revealing ancilla-system entanglement, with $\mathcal{P} = 1/2$ corresponding to a maximally entangled state.

4.3 Real-time dynamics and spectroscopic protocol.

Let us now analyze the total system real-time dynamics. From the previous considerations on the spectrum, it emerges that it is appropriate to describe the global system using a separable basis for the Hilbert space $\mathcal{H}_{\text{ancilla}}$ of the ancilla and of the USC qubit-cavity system $\mathcal{H}_{\text{polariton}}$. Accordingly, we formally rewrite the Hamiltonian of Eq. (4.2) as

$$\begin{aligned} H &= \hbar \sum_j \omega_j \left|\psi_j\right\rangle \left\langle\psi_j\right| + \frac{\hbar\omega_a}{2}\sigma_z^a + H_I \\ H_I &= \hbar g_a \sigma_x^a \sum_{ij} \left[k_{ij} \left|\psi_i\right\rangle \left\langle\psi_j\right| + k_{ji}^* \left|\psi_i\right\rangle \left\langle\psi_j\right|\right], \end{aligned} \tag{4.3}$$

where we denote $|\psi_j\rangle$ as polariton states of energy $\hbar\omega_j$, *i.e.* eigenstates of H_S (4.1). We defined the transition matrix elements $k_{ij} = \langle\psi_i| a |\psi_j\rangle$.

Because of the strong anharmonicity of the QRM, when the ancilla frequency matches a given polariton transition $\omega_a = \omega_\alpha - \omega_\beta$, we can perform a RWA and rewrite the interaction Hamiltonian H_I as (see Appendix C.2)

$$H_I = \hbar g_a \left(k_{\alpha\beta} + k_{\beta\alpha}^*\right) \sigma_-^a \ \left|\psi_\alpha\right\rangle \left\langle\psi_\beta\right| + \text{H.c.}, \tag{4.4}$$

where we fixed $\omega_\alpha > \omega_\beta$. Such a Hamiltonian induces coherent excitation transfer between the ancilla qubit and the polariton system. Notice that the matrix element k_{ij} is non-vanishing only for transitions that link states of opposite parity in the polaritonic system. To check the validity of our analytical treatment, we simulate the real-time dynamics of the full model. We take into account decoherence effects by means of second-order time-convolutionless projection operator method [36], which correctly describes the dissipative dynamics in the USC regime. In this simulation we have considered zero-temperature thermal baths and noises acting on the $\hat{X}$ quadrature and transversal noise (σ_x) for both two-level systems. Realistic parameters for superconducting circuits have been considered. Fig. 4.4c shows an example of Rabi oscillations (green continuous line) between the states $|e\rangle|\psi_0\rangle$ and $|g\rangle|\psi_1\rangle$, where we denoted with $|g\rangle(|e\rangle)$ the ground(excited) state of the ancillary qubit.

We stress that counter-rotating terms $g_a\left(\sigma_+^a a^\dagger + \sigma_-^a a\right)$ of the ancilla-cavity coupling, see Eq.(4.2), play an important role in the total system dynamics. Those terms contribute to Eq. (4.4) with the coefficients $k_{\alpha\beta}$ and $k_{\beta\alpha}^*$, given that we fixed $\omega_\alpha > \omega_\beta$. Their effect is highlighted in Fig. 4.4c by reproducing the same dynamics in the case in which such contributions are artificially neglected (black dashed line). Notice that, if the system qubit were removed, or if it were interacting in the SC regime, the effect of

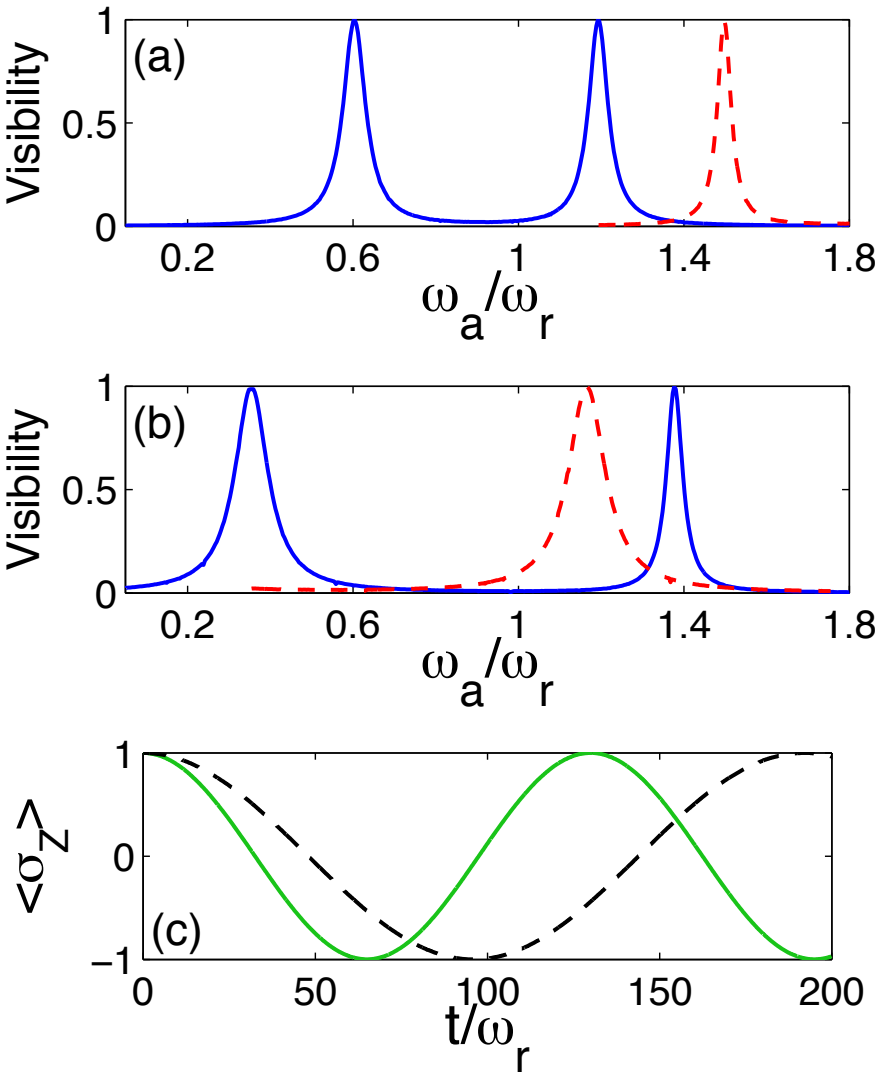

FIGURE 4.4: (a), (b) Numerical simulation of the spectroscopy protocol. Visibility of the ancilla population oscillations as a function of frequency ω_a. Physical parameters correspond to the vertical cuts in Fig. 4.2. For both (a) and (b), the system qubit frequency is $\omega/\omega_r = 0.8$ and the ancilla-field cavity coupling is $g_a/\omega_r = 0.02$. The USC system coupling is $g/\omega_r = 0.3$ for (a) and $g/\omega_r = 0.6$ for (b). The parity of each energy level is identified, blue continuous line for odd and red-dashed lines for even states. (c) Comparison of full model (green continuous line) to the dynamics obtained when removing counter-rotating terms from the ancilla-cavity interaction (black dashed line). System parameters are the same that in box (b). In all cases, decay rates are $\gamma/\omega_r = 10^{-3}$ for the system qubit, $\gamma_r/\omega_r = 10^{-4}$ for the cavity and $\gamma_a/\omega_r = 10^{-4}$ for the ancilla.

counter-rotating terms of the ancilla-cavity interaction would be negligible for such small values of the ratio g_a/ω. In fact, the presence of a qubit in the USC regime modifies the mode structure of the cavity field in such a way that the coefficients k_{ij} can be non-vanishing also for $\omega_i > \omega_j$ (see Appendix C.2). In simple words, this condition implies that removing a photon results in an increase of the system energy, in striking contrast with Jaynes-Cummings-like energy spectrum. Indeed, the counterintuitive breaking of

the RWA, explained here for an ancilla interacting with a ultrastrongly coupled system, unveils a general feature of the USC regime.

The expectation value of σ_z^a can be measured by detuning ω_a out of resonance, with respect to the USC system, and in resonance with an idle cavity for readout [57, 175]. This enables us to design a spectroscopy protocol for the USC system, which identifies the parity of each energy level. Such a protocol consists in keeping track of the expectation value $\langle\sigma_z^a\rangle$ during the time-evolution, after initializing the USC system in its ground level and the ancilla in its excited state $|\phi_0^{\mathrm{e}}\rangle = |\psi_0\rangle\,|e\rangle$. Notice that the ground and first-excited states of the QRM Hamiltonian have even and odd parity, respectively. The initialization can be realized when the ancilla is far off-resonance, then its frequency can be suddenly switched [174] to be within the relevant frequency range. As the ancilla frequency becomes closer to a given transition of the USC system, the amplitude of the excitation transfer increases, granted that the process preserves the global parity. Thus, sampling the ancilla dynamics for different values of ω_a, we can deduce the USC system eigenvalues belonging to a specific parity subspace (blue continuous line in Fig. 4.4a and Fig. 4.4b). We define the visibility as half the difference between the maximum and the minimum values reached by $\langle\sigma_z^a\rangle$ during its time-evolution. Considering realistic parameters of superconducting circuit technology, taking $\omega_r = 2\pi \times 5$ GHz, the first three resonance peaks can be obtained within a time of approximatively 10 μs (see AppendixC.3).

In the same way, we can obtain the level structure of the *even* subspace (red dashed line in Fig. 4.4a and Fig. 4.4b) by repeating the protocol with the odd initial state $|\phi_0^{\mathrm{o}}\rangle = |\psi_1\rangle\,|e\rangle$, i.e., both the ancilla and the USC system in their first-excited state. The total system can be initialized in such a state via state-transfer process (see below) plus a spin-flip operation on the ancilla qubit. The proposed spectroscopic protocol allows us to obtain the parity structure of the USC system in a direct way. Hence, one could check the eigenstate-parity inversion (see Fig. 4.2), which is specific to the QRM and represents a distinctive signature of the USC regime. Higher energy levels can be obtained in a similar way with a multi-step procedure. Notice that the widths of the resonance peaks in Fig. 4.4 are proportional to the matrix elements k_{ij}, hence they contain information about the eigenstates of the USC system.

4.4 Tomography and state engineering.

So far we have considered the ancillary qubit dynamics as a tool to investigate the spectral structure of the USC system. Let us now focus on how this ancilla can be used as a tool to fully measure and control the USC, granted that a limited number

of its eigenstates can be excited. First, we show how the tomography of the ancillary qubit [176] enables us to recover all the coefficients of the USC density matrix. The protocol to be followed consists in initializing the ancilla in a proper state, implementing a selective state transfer between the USC system and the ancilla, and performing tomography of the latter. After the initialization of the ancilla, the global density matrix reads $\rho = \sum_{i,j} \rho_{ij} \left|\psi_i\right\rangle \left\langle\psi_j\right| \otimes \left|g\right\rangle \left\langle g\right|$. For opposite parity eigenstates $\left|\psi_n\right\rangle$ and $\left|\psi_m\right\rangle$, implementing the state transfer process $\left|\psi_n\right\rangle \left|g\right\rangle \leftrightarrow \left|\psi_m\right\rangle \left|e\right\rangle$, and tracing over the USC system degrees of freedom, we obtain the ancillary qubit density matrix

$$\rho_a = \rho_0 \left|g\right\rangle \left\langle g\right| + \rho_{nn} \left|e\right\rangle \left\langle e\right| + \rho_{nm} \left|e\right\rangle \left\langle g\right| + \rho_{mn} \left|g\right\rangle \left\langle e\right|, \tag{4.5}$$

where $\rho_0 = \sum_{i \neq n} \rho_{ii}$. Hence, performing tomography over the ancilla yields the value of the population in state $\left|\psi_n\right\rangle$ and the coherence coefficients with $\left|\psi_m\right\rangle$. In order to infer the coherences between USC system states of identical parity, a slightly different procedure must be used. In this case, a two-step state transfer process can be implemented, making use of a third level of opposite parity to mediate the interaction, as shown in Appendix C.4. Then, iterating the protocol for all couples of relevant eigenstates, the complete density matrix of the USC system state can be reconstructed.

Notice that the selective state-transfer processes introduced for the tomography protocol can be performed in a reverse way to engineer the state of the USC system itself. Assuming that any single-qubit gate can be performed on the ancilla, the components of the USC system state in the energy eigenbasis can be individually addressed by means of the selective interactions of Eq. (4.4). Again, parity-forbidden transitions can be circumvented by means of a two-step protocol (see Appendix C.4). For instance, the USC system can be prepared in any superposition of its eigenstates by iteratively initializing the ancilla qubit in the desired state, tuning its energy spacing to match a given transition, and performing a selective state-transfer. This feature can be exploited in order to connect ultrastrongly-coupled systems with standard quantum information processing devices. For instance a logical qubit can be encoded in the ancilla state and then transferred to the polariton, where the computational benefits of the USC coupling can be exploited [43–45].

4.5 Conclusions

In conclusion, we have analyzed the interaction between an ancillary qubit and an ultrastrongly coupled qubit-cavity system. We find that the presence of a USC qubit-cavity system modifies the interaction of the cavity with the ancillary qubit in a nontrivial manner. We have designed a spectroscopy protocol able to detect parity-inversion of

eigenstates, a signature of the USC regime in the QRM, requiring control over a single ancillary qubit and tunability of its effective frequency. The present method can be applied in order to certify that a device is operating in the USC regime of the quantum Rabi model. Moreover, we show that the same ancilla may be used as a tool to engineer the dynamics of arbitrary USC system states. The proposed method overcomes the lack of decoupling mechanisms in the USC regime, requiring minimal external resources. For example, the present technique could be applied to measure and process the polariton Bell state produced with the proposal described in chapter 3. Our results pave the way to novel applications of the USC regime of the QRM in quantum technologies and quantum information processing.

Part II

Ultrastrong coupling regime in atomic systems

Chapter 5

Quantum Rabi Model with Trapped Ions

5.1 Introduction

As detailed in the introduction of the present Thesis, several systems have recently been able to experimentally reach the USC regime of the quantum Rabi model (QRM). To extend the list of quantum platforms where it has been possible to observe signatures of the breaking of the rotating wave approximation, we can mention the case of circuit QED [26, 28], semiconductor systems coupled to metallic microcavities [177–179], split-ring resonators connected to cyclotron transitions [180], or magnetoplasmons coupled to photons in coplanar waveguides [181]. These first achievements, together with recent theoretical advances, have put the QRM back in the scientific spotlight. However impressive it looks, these experimental results have been limited to explore the lower coupling region of the QRM, where the system spectrum and real-time dynamics can still be described with perturbative corrections of the Jaynes-Cummings model. Yet the most interesting features of the QRM appear in the nonperturbative USC regime, or in the DSC regime, where the system dynamics is well described by the slow-qubit approximation [38, 42, 128, 167, 173, 182, 183]. As these regimes of light-matter interactions are extremely challenging to achieve, analog quantum simulations represent a valuable alternative to implement USC models in any regime. To this respect, of particular interest are scalable quantum systems, which have the potential to provide answers on physical models that cannot be obtained with analytical or numerical methods.

Trapped ions are considered as one of the prominent platforms for building quantum simulators [69]. In fact, the realization and thorough study of the JC model in ion traps, a model originally associated with CQED, is considered a cornerstone in physics [184,

185]. This is done by applying a red-sideband interaction with laser fields to a single ion [65, 66, 186] and may be arguably presented as the first quantum simulation ever implemented. In this sense, the quantum simulation of all coupling regimes of the QRM in trapped ions would be a historically meaningful step forward in the study of dipolar light-matter interactions.

In this chapter, we discuss a method that allows the access to the full-fledged QRM with trapped-ion technologies by means of a suitable interaction picture associated with inhomogeneously detuned red and blue sideband excitations. Note that, in the last years, bichromatic laser fields have been successfully used for different purposes [187–190]. In addition, we propose an adiabatic protocol to generate the highly-correlated ground states of the USC and DSC regimes.

5.2 The model

Single atomic ions can be confined using radio-frequency Paul traps and their motional quantum state cooled down to its ground state by means of sideband cooling techniques [69]. In this respect, two internal metastable electronic levels of the ion can play the role of a quantum bit (qubit). Driving a monochromatic laser field in the resolved-sideband limit allows for the coupling of the internal qubit and the motional mode, whose associated Hamiltonian reads ($\hbar = 1$)

$$\begin{aligned} H &= \frac{\omega_0}{2}\sigma_z + \nu a^\dagger a + \Omega(\sigma^+ + \sigma^-)\Big(\exp\{i[\eta(a + a^\dagger) - \omega_l t + \phi_l]\} \\ &+ \exp\{-i[\eta(a + a^\dagger) - \omega_l t + \phi_l]\}\Big). \end{aligned} \tag{5.1}$$

Here, $a^\dagger$ and a are the creation and annihilation operators of the motional mode, σ^+ and σ^- are the raising and lowering Pauli operators, ν is the trap frequency, ω_0 is the qubit transition frequency, Ω is the Rabi coupling strength, and η is the Lamb-Dicke parameter, while ω_l and ϕ_l are the corresponding frequency and phase of the laser field. For the case of a bichromatic laser driving, changing to an interaction picture with respect to the free-energy Hamiltonian, $H_0 = \frac{\omega_0}{2}\sigma_z + \nu a^\dagger a$ and applying an optical RWA, the dynamics of a single ion reads [66]

$$H^{\mathrm{I}} = \sum_{n=r,b} \frac{\Omega_n}{2}\left[e^{i\eta[a(t)+a^\dagger(t)]}e^{i(\omega_0-\omega_n)t}\sigma^+ + \mathrm{H.c.}\right], \tag{5.2}$$

with $a(t) = ae^{-i\nu t}$ and $a^\dagger(t) = a^\dagger e^{i\nu t}$. We will consider the case where both fields are off-resonant, first red-sideband (r) and first blue-sideband (b) excitations, with detunings

δ_r and δ_b, respectively,

$$\omega_r = \omega_0 + \nu + \delta_r, \;\; \omega_b = \omega_0 - \nu + \delta_b.$$

In such a scenario, one may neglect fast oscillating terms in Eq. (5.2) with two different vibrational RWAs. We will restrict ourselves to the Lamb-Dicke regime, that is, we require that $\eta\sqrt{\langle a^\dagger a\rangle} \ll 1$. This allows us to select terms that oscillate with minimum frequency, assuming that weak drivings do not excite higher-order sidebands, $\delta_n, \Omega_n \ll \nu$ for $n = r, b$. These approximations lead to the simplified time-dependent Hamiltonian

$$\bar{H}^{\mathrm{I}} = \frac{i\eta\Omega}{2}\sigma^+ \left(ae^{-i\delta_r t} + a^\dagger e^{-i\delta_b t}\right) + \mathrm{H.c.}, \tag{5.3}$$

where we consider equal coupling strengths for both sidebands, $\Omega = \Omega_r = \Omega_b$. By switching to a further interaction picture, defined by $H_0 = \frac{1}{4}(\delta_b + \delta_r)\sigma_z + \frac{1}{2}(\delta_b - \delta_r)a^\dagger a$, we get rid of the time dependence and the full Rabi Hamiltonian arises,

$$H_{\mathrm{QRM}} = \frac{\omega_0^R}{2}\sigma_z + \omega^R a^\dagger a + ig(\sigma^+ - \sigma^-)(a + a^\dagger), \tag{5.4}$$

where the effective qubit and mode frequencies,

$$\omega_0^R = -\frac{1}{2}(\delta_r + \delta_b), \;\; \omega^R = \frac{1}{2}(\delta_r - \delta_b), \;\; g = \frac{\eta\Omega}{2}, \tag{5.5}$$

are represented by the sum and difference of both detunings, respectively. The tunability of these parameters permits the study of all coupling regimes of the QRM via the suitable choice of the ratio g/ω^R. It is important to note that all realized interaction-picture transformations, so far, are of the form $\alpha a^\dagger a + \beta\sigma_z$. This expression commutes with the observables of interest, $\{\sigma_z, |n\rangle\langle n|, a^\dagger a\}$, warranting that their experimental measurement will not be affected by the transformations.

5.3 Accessible regimes

The quantum Rabi model in Eq. (5.4) will show distinct dynamics for different regimes, which are defined by the relation among the three Hamiltonian parameters: the mode frequency ω^R, the qubit frequency ω_0^R, and the coupling strength g.

We first explore the regimes that arise when the coupling strength is much weaker than the mode frequency $g \ll |\omega^R|$. Under such a condition, if the qubit is close to resonance, $|\omega^R| \sim |\omega_0^R|$, and $|\omega^R + \omega_0^R| \gg |\omega^R - \omega_0^R|$ holds, the RWA can be applied. This implies neglecting terms that in the interaction picture rotate at frequency $\omega^R + \omega_0^R$, leading to the JC model. This is represented in Fig. 5.1 by the region 1 in the diagonal.

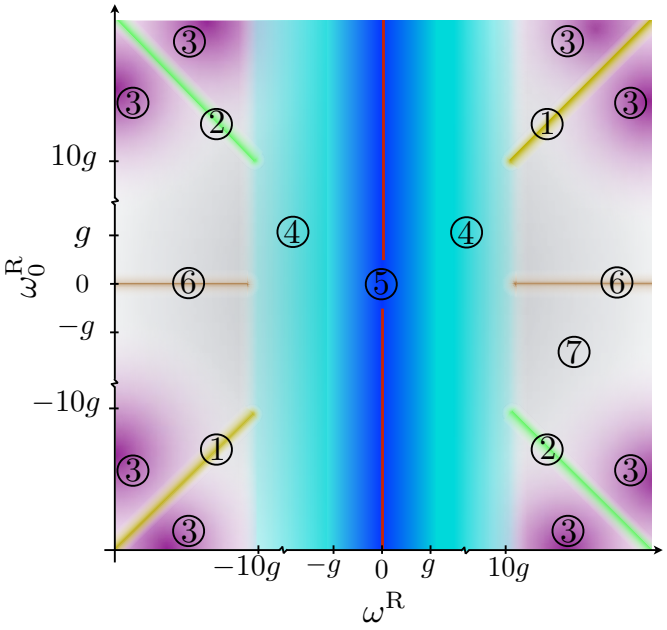

FIGURE 5.1: Configuration space: (1) JC regime: $g \ll \{|\omega^R|, |\omega_0^R|\}$ and $|\omega^R - \omega_0^R| \ll |\omega^R + \omega_0^R|$. (2) AJC regime: $g \ll \{|\omega^R|, |\omega_0^R|\}$ and $|\omega^R - \omega_0^R| \gg |\omega^R + \omega_0^R|$. (3) Two-fold dispersive regime: $g < \{|\omega^R|, |\omega_0^R|, |\omega^R - \omega_0^R|, |\omega^R + \omega_0^R|\}$. (4) USC regime: $|\omega^R| < 10g$, (5) DSC regime: $|\omega^R| < g$, (6) Decoupling regime: $|\omega_0^R| \ll g \ll |\omega^R|$. (7) This intermediate regime ($|\omega_0^R| \sim g \ll |\omega^R|$) is still open to study. The (red) central vertical line corresponds to the Dirac equation regime.

Notice that these conditions are only possible if both the qubit and the mode frequency have the same sign. However, in a quantum simulation one can go beyond conventional regimes and even reach unphysical situations, as when the qubit and the mode have frequencies of opposite sign. In this case, $|\omega^R - \omega_0^R| \gg |\omega^R + \omega_0^R|$ holds, see region 2, and we will be allowed to neglect terms that rotate at frequencies $|\omega^R - \omega_0^R|$. This possibility will give rise to the anti-Jaynes Cummings (AJC) Hamiltonian, $H^{AJC} = \frac{\omega_0^R}{2}\sigma_z + \omega^R a^\dagger a + ig(\sigma^+ a^\dagger - \sigma^- a)$. It is noteworthy to mention that, although both JC and AJC dynamics can be directly simulated with a single tuned red or blue sideband interaction, respectively, the approach taken here is fundamentally different. Indeed, we are simulating the QRM in a regime that corresponds to such dynamics, instead of directly implementing the effective model, namely the JC or AJC model.

If we depart from the resonance condition and have all terms rotating at high frequencies $\{|\omega^R|, |\omega_0^R|, |\omega^R + \omega_0^R|, |\omega^R - \omega_0^R|\} \gg g$, see region 3, for any combination of frequency signs, the system experiences dispersive interactions governed by a second-order effective Hamiltonian. In the interaction picture, this Hamiltonian reads

$$H_{\text{eff}} = g^2 \left[\frac{|e\rangle\langle e|}{\omega^R - \omega_0^R} - \frac{|g\rangle\langle g|}{\omega^R + \omega_0^R} + \frac{2\omega^R}{(\omega_0^R + \omega^R)(\omega^R - \omega_0^R)} a^\dagger a \sigma_z \right], \tag{5.6}$$

inducing AC-Stark shifts of the qubit energy levels conditioned to the number of excitations in the bosonic mode.

The USC regime is defined as $0.1 \lesssim g/\omega^R \lesssim 1$, with perturbative and nonperturbative intervals, and is represented in Fig. 5.1 by region 4. In this regime, the RWA does not hold any more, even if the qubit is in resonance with the mode. In this case, the description of the dynamics has to be given in terms of the full quantum Rabi Hamiltonian. For $g/\omega^R \gtrsim 1$, we enter into the DSC regime, see region 5 in Fig. 5.1, where the dynamics can be explained in terms of phonon number wave packets that propagate back and forth along well defined parity chains [42].

In the limit where $\omega^R = 0$, represented by a vertical centered red line in Fig. 5.1, the quantum dynamics is given by the relativistic Dirac Hamiltonian in 1+1 dimensions,

$$H_D = mc^2\sigma_z + cp\sigma_x, \tag{5.7}$$

which has been successfully implemented in trapped ions [81, 82], as well as in other platforms [191, 192].

Moreover, an interesting regime appears when the qubit is completely out of resonance and the coupling strength is small when compared to the mode frequency, $\omega_0^R \sim 0$ and $g \ll |\omega^R|$. In this case, the system undergoes a particular dispersive dynamics, where the effective Hamiltonian becomes a constant. Consequently, the system does not evolve in this region that we name as decoupling regime, see region 6 in Fig. 5.1. The remaining regimes correspond to region 7 in Fig. 5.1, associated with the parameter condition $|\omega_0^R| \sim g \ll |\omega^R|$.

The access to different regimes is limited by the maximal detunings allowed for the driving fields, which are given by the condition $\delta_{r,b} \ll \nu$, ensuring that higher-order sidebands are not excited. The simulations of the JC and AJC regimes, which demand detunings $|\delta_{r,b}| \leq |\omega^R| + |\omega_0^R|$, are the ones that may threaten such a condition. We have numerically simulated the full Hamiltonian in Eq. (5.2) with typical ion-trap parameters: $\nu = 2\pi \times 3$MHz, $\Omega = 2\pi \times 68$kHz and $\eta = 0.06$ [82], while the laser detunings were $\delta_b = -2\pi \times 102$kHz and $\delta_r = 0$, corresponding to a simulation of the JC regime with $g/\omega^{\mathrm{R}} = 0.01$. The numerical simulations show that second-order sideband transitions are not excited and that the state evolution follows the analytical JC solution with a fidelity larger than 99% for several Rabi oscillations. This confirms that the quantum simulation of these regimes is also accessible in the lab. We should also pay attention to the Lamb-Dicke condition $\eta\sqrt{\langle a^\dagger a\rangle} \ll 1$, as evolutions with an increasing number of phonons may jeopardize it. However, typical values like $\eta = 0.06$ may admit up to

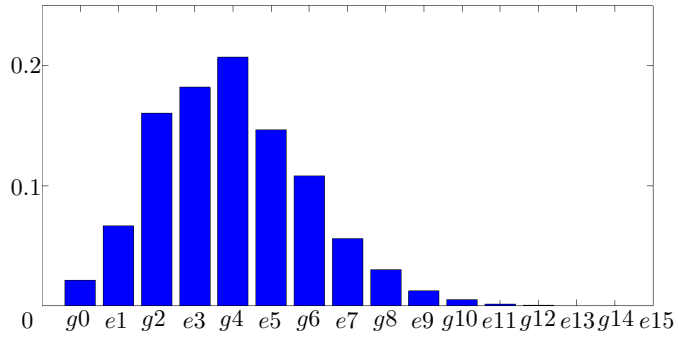

FIGURE 5.2: State population of the QRM ground state for $g/\omega^R = 2$, parity $p = +1$, and corresponding parity basis $\{|g,0\rangle, |e,1\rangle, |g,2\rangle, |e,3\rangle, \ldots\}$. Here, p is the expectation value of the parity operator $P = \sigma_z e^{-i\pi a^\dagger a}$ [42], and only states with even number of excitations are populated. We consider a resonant red-sideband excitation ($\delta_r = 0$), a dispersive blue-sideband excitation ($\delta_b/2\pi = -11.31$kHz), and $g = -\delta_b$, leading to the values $\omega^R = \omega_0^R = -\delta_b/2$ and $g/\omega^R = 2$.

some tens of phonons, allowing for an accurate simulation of the QRM in all considered regimes.

Regarding coherence times, the characteristic timescale of the simulation will be given by $t_{\text{char}} = \frac{2\pi}{g}$. In our simulator, $g = \frac{\eta\Omega}{2}$, such that $t_{\text{char}} = \frac{4\pi}{\eta\Omega}$. For typical values of $\eta = 0.06 - 0.25$ and of $\Omega/2\pi = 0 - 500$ kHz, the dynamical timescale of the system is of milliseconds, well below coherence times of qubits and motional degrees of freedom in trapped-ion setups [69].

5.4 State preparation

The ground state $|G\rangle$ of the QRM in the JC regime ($g \ll \omega^R$) is given by the state $|g,0\rangle$, that is, the qubit ground state, $|g\rangle$, and the vacuum of the bosonic mode, $|0\rangle$. It is known that $|g,0\rangle$ will not be the ground state of the interacting system for larger coupling regimes, where the contribution of the counter-rotating terms becomes important [193]. As seen in Fig. 5.2, the ground state of the USC/DSC Hamiltonian is far from trivial [19], essentially because it contains qubit and mode excitations, $\langle G|a^\dagger a|G\rangle > 0$.

Hence, preparing the qubit-mode system in its actual ground state is a rather difficult state-engineering task in most parameter regimes, except for the JC limit. We propose here to generate the ground state of the USC/DSC regimes of the QRM via adiabatic evolution. Figure 5.3 shows the fidelity of the state prepared following a linear law of variation for the coupling strength at different evolution rates. When our system is initialized in the JC region, achieved with detunings $\delta_r = 0$ and $|\delta_b| \gg g$, it is described by a JC Hamiltonian with the ground state given by $|G\rangle = |g,0\rangle$. Notice that the g/ω^{R} ratio can be slowly turned up, taking the system adiabatically through a straight line in

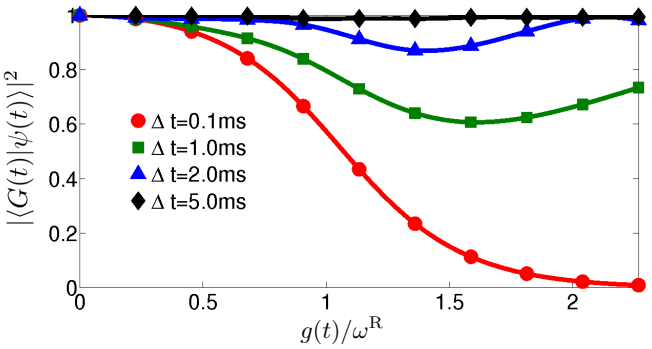

FIGURE 5.3: Let us assume that the system is initially prepared in the JC ground state $|g,0\rangle$, that is, when $g \ll \omega^R$. Then, the coupling is linearly chirped during an interval Δt up to a final value g_f, i. e., $g(t) = g_f t/\Delta t$. For slow changes of the laser intensity, the ground state is adiabatically followed, whereas for non-adiabatic processes, the ground state is abandoned. The instantaneous ground state $|G(t)\rangle$ is computed by diagonalizing the full Hamiltonian at each time step, while the real state of the system $|\psi(t)\rangle$ is calculated by numerically integrating the time dependent Schrödinger equation for a time-varying coupling strength $g(t)$. For the simulation, a $^{40}Ca^{+}$ ion has been considered with parameters: $\nu = 2\pi \times 3$MHz, $\delta_r = 0$, $\delta_b = -6 \times 10^{-4}\nu$, $\eta = 0.06$ and $\Omega_f = 2\pi \times 68$kHz [82].

the configuration space to regions 4-5 [44]. This can be done either increasing the value of g by raising the intensity of the driving, or decreasing the value of ω^{R} by reducing the detuning $|\delta_b|$. The adiabatic theorem ensures that if this process is slow enough, transitions to excited states will not occur and the system will remain in its ground state. As expected, lower rates ensure a better fidelity.

5.5 Conclusions

In this chapter, we have presented a method for implementing a quantum simulation of the QRM in ion traps with nowadays technology. Its main advantage consists in the accessibility to the USC/DSC regimes and the required switchability to realize full tomography, outperforming other systems where the QRM should appear more naturally, such as cQED [194, 195]. In addition, we have shown how to prepare the qubit-mode system in its entangled ground state through adiabatic evolution from the known JC limit into the USC/DSC regimes. This would allow for the complete reconstruction of the QRM ground state, never realized in the lab, in a highly controllable quantum platform as trapped ions. The present ideas are straightforwardly generalizable to many ions, opening the possibility of going from the more natural Tavis-Cummings model to the Dicke model.

Chapter 6

Spectral Collapse via Two-phonon Interactions in Trapped Ions

6.1 Introduction

In the last decades, the quantum Rabi model has been considered in regimes where the rotating-wave approximation holds, giving rise to the Jaynes-Cummings model [17] and describing a plethora of experiments, mostly related to cavity quantum electrodynamics. On the other hand, from a mathematical point of view, an analytical solution for the spectrum of the quantum Rabi model in all regimes has been only recently developed [19]. Such a result has prompted a number of theoretical efforts aimed at applying similar techniques to generalizations of the quantum Rabi model, including anisotropic couplings [196–198], two-photon interactions [199–202] and multi-qubit extensions [203], as is the case of the Dicke model.

In particular, the two-photon quantum Rabi model enjoys a spectrum with highly counterintuitive features [204, 205], which appear when the coupling strength becomes comparable with the bosonic mode frequency. In this sense, it is instructive to compare these features with the ultrastrong [25, 26, 28] and deep strong [42] coupling regimes of the quantum Rabi model [206]. The two-photon quantum Rabi model has been applied as an effective model to describe second-order processes in different physical setups, like Rydberg atoms in microwave superconducting cavities [207] and quantum dots [208, 209]. However, the considered small second-order coupling strengths takes us to the RWA domains and restrict the observation of the richer dynamics of the model.

In this chapter, we design a trapped-ion scheme in which the two-photon quantum Rabi and two-photon Dicke models can be realistically implemented in all relevant

regimes. We theoretically show that the dynamics of the proposed system is characterized by harmonic two-phonon oscillations or by spontaneous generation of excitations, depending on the effective coupling parameter. In particular, we consider cases where complete spectral collapse—namely, the fusion of discrete energy levels into a continuous band—can be observed.

In trapped-ion systems [210, 211], it is possible to control the coherent interaction between the vibrations of an ion crystal and internal electronic states, which form effective spin degrees of freedom. This quantum technology has emerged as one of the most promising platforms for the implementation of quantum spin models, including few [75] or hundreds [76] of ions. A variety of complex quantum phenomena has been explored using trapped-ion setups, like Ising spin frustration [77], quantum phase transitions [78, 79] and the inhomogeneous Kibble-Zurek mechanism [80]. Furthermore, second sidebands have been considered for laser cooling [212] and for generating nonclassical motional states [213–215].

6.2 The model

We consider a chain of N qubits interacting with a single bosonic mode via two-photon interactions

$$\mathcal{H} = \omega a^\dagger a + \sum_n \frac{\omega_q^n}{2}\sigma_z^n + \frac{1}{N}\sum_n g_n \sigma_x^n \left(a^2 + a^{\dagger 2}\right), \tag{6.1}$$

where $\hbar = 1$, a and $a^\dagger$ are bosonic ladder operators; σ_x^n and σ_z^n are qubit Pauli operators; parameters ω, ω_q^n, and g_n, represent the mode frequency, the n-th qubit energy spacing and the relative coupling strength, respectively. We will explain below how to implement this model using current trapped-ion technology, considering in detail the case $N = 1$ and discussing the scalability issues for $N > 1$.

We consider a setup where the qubit energy spacing, $\omega_{\rm int}$, represents an optical or hyperfine/Zeeman internal transition in a single trapped ion. The vibrational motion of the ion is described by bosonic modes a, $a^\dagger$, with trap frequency ν. Turning on a bichromatic driving, with frequencies ω_r and ω_b, an effective coupling between the internal and motional degrees of freedom is activated. In the interaction picture, the standard Hamiltonian [210] describing this model reads

$$\mathcal{H}^I = \sum_{j=r,b} \frac{\Omega_j}{2}\left\{e^{i\eta_j\left[a(t)+a^\dagger(t)\right]} e^{i(\omega_{\rm int}-\omega_j)t} e^{i\phi_j}\sigma_+ + \text{H.c.}\right\}, \tag{6.2}$$

where $a(t) = a\ e^{-i\nu t}$. Here, Ω_r and Ω_b are coupling parameters directly proportional to the driving laser amplitude, and ϕ_j represents the phase of each laser with respect

to the atom dipole. The Lamb-Dicke parameter $\eta_j = k_z^j \sqrt{\frac{\hbar}{2m\nu}}$ is defined by the the projection k_z^j of the j-th laser field wavevector in the z direction and by the ion mass m. We consider the system to be in the Lamb-Dicke regime, $\eta^2(2\langle\hat{n}\rangle + 1) \ll 1$, where $\hat{n} = a^\dagger a$ is the phonon number operator.

We set the frequencies of the bichromatic driving to be detuned from the second sidebands, $\omega_r = \omega_{\rm int} - 2\nu + \delta_r$, $\omega_b = \omega_{\rm int} + 2\nu + \delta_b$. The frequency shifts δ_r and δ_b will introduce tunable effective energies for the qubit and field. We choose homogeneous Lamb-Dicke parameters $\eta_j = \eta$, phases $\phi_j = 0$, and coupling strengths $\Omega_j = \Omega$ for both sideband excitations. Expanding the exponential operator in Eq. (6.2) to the second order in η, and performing a RWA with $\delta_j, \Omega_j \ll \nu$, we can rewrite the interaction picture Hamiltonian

$$\mathcal{H}^I = -\frac{\eta^2\Omega}{4}\left[a^2\ e^{-i\delta_r t} + a^{\dagger 2}\ e^{-i\delta_b t}\right]\sigma_+ + \text{H.c.} \tag{6.3}$$

The first-order correction to approximations made in deriving Eq. (6.3) is given by $\frac{\Omega}{2}\ e^{\pm i2\nu t}\sigma_+ + \text{H.c.}$, which produce spurious excitations with negligible probability $P_e = \left(\frac{\Omega}{4\nu}\right)^2$. Further corrections are proportional to $\eta\Omega$ or η^2 and oscillate at frequency ν, yielding $P_e = \left(\frac{\eta\Omega}{4\nu}\right)^2$. Hence, they are negligible in standard trapped-ion implementations. The explicit time dependence in Eq. (6.3) can be removed by going to another interaction picture with $\mathcal{H}_0 = \frac{1}{4}\left(\delta_b - \delta_r\right)a^\dagger a + \frac{1}{4}\left(\delta_b + \delta_r\right)\sigma_z$, which we dub simulation picture. Then, the system Hamiltonian resembles the two-phonon quantum Rabi Hamiltonian

$$\mathcal{H}_{\rm eff} = \omega\ a^\dagger a + \frac{\omega_q}{2}\sigma_z - g\ \sigma_x\left(a^2 + a^{\dagger 2}\right), \tag{6.4}$$

where the effective model parameters are linked to physical variables through $\omega = \frac{1}{4}\left(\delta_r - \delta_b\right)$, $\omega_q = -\frac{1}{2}\left(\delta_r + \delta_b\right)$, and $g = \frac{\eta^2\Omega}{4}$. Remarkably, by tuning δ_r and δ_b, the two-phonon quantum Rabi model of Eq. (6.4) can be implemented in all regimes. Moreover, the N-qubit two-phonon Dicke model of Eq. (6.1) can be implemented using a chain of N ions by applying a similar method. In this case, the single bosonic mode is represented by a collective motional mode [74], see section 6.3 for further details.

The validity of the approximations made in deriving Eq. (6.4) has been checked comparing the simulated two-photon quantum Rabi dynamics with numerical evaluation of the simulating trapped-ion model of Eq. (6.2), as shown in Fig. 6.1. Standard parameters and dissipation channels of current setups have been considered. In all plots of Fig. 6.1, the vibrational frequency is $\nu/2\pi = 1$ MHz and the coupling coefficient is $\Omega/2\pi = 100$ KHz. The Lamb-Dicke parameter is $\eta = 0.04$ for Fig. 6.1a and Fig. 6.1b, while $\eta = 0.02$ for Fig. 6.1c. Notice that larger coupling strengths imply a

more favourable ratio between dynamics and dissipation rates. Hence, the implementation accuracy improves for large values of g/ω, which correspond to the most interesting coupling regimes.

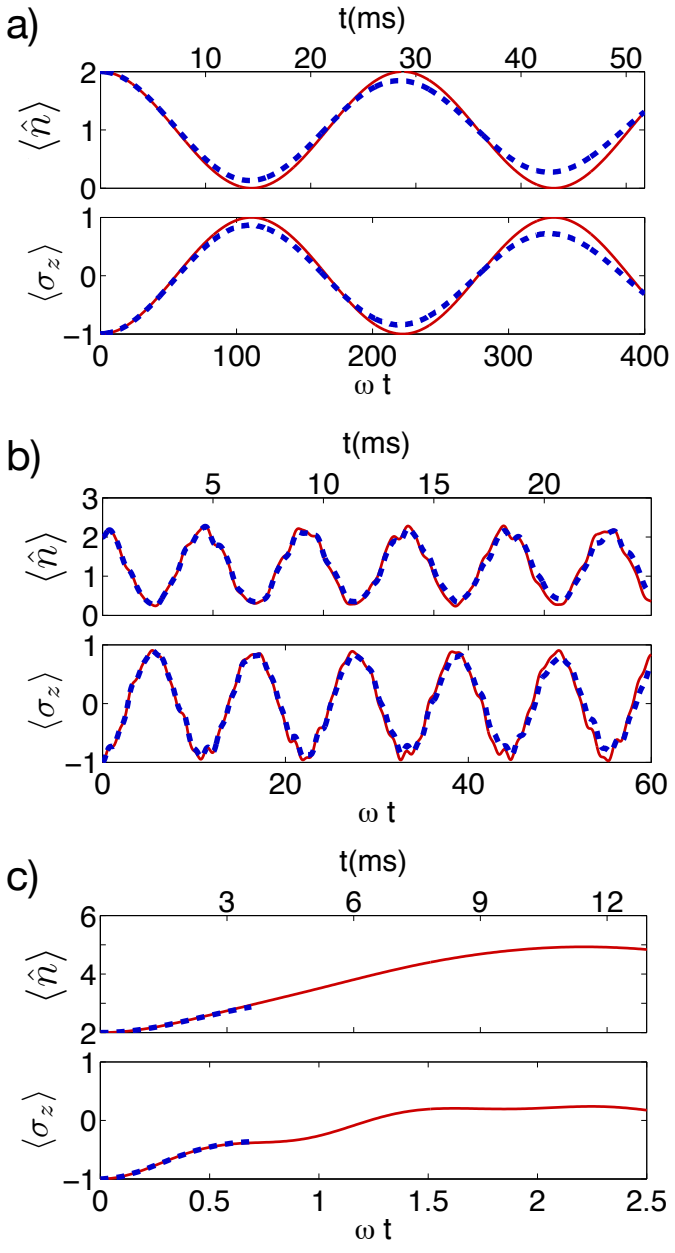

FIGURE 6.1: Real-time dynamics for $N = 1$, resonant qubit $\omega_q = 2\omega$, and effective couplings: (a) $g = 0.01\omega$, (b) $g = 0.2\omega$, and (c) $g = 0.4\omega$. The initial state is given by $|g, 2\rangle$, i.e., the two-phonon Fock state and the qubit ground state. In all plots, the red continuous line corresponds to numerical simulation of the exact Hamiltonian of Eq. (6.1), while the blue dashed line is obtained simulating the full model of Eq. (6.2), including qubit decay $t_1 = 1$s, pure dephasing $t_2 = 30$ms and vibrational heating of one phonon per second. In each plot, the lower abscissa shows the time in units of ω, while the upper one shows the evolution time of a realistic trapped-ion implementation. In panel (c), the full model simulation could not be performed for a longer time due to the fast growth of the Hilbert-space.

6.3 Implementation of the two-photon Dicke model

In the previous section, we showed how a two-photon Rabi model can be implemented using the vibrational degree of freedom of a single ion, coupled to one of its internal electronic transitions by means of laser-induced interactions. Let us now show how the N-qubit two-photon Dicke model

$$\mathcal{H} = \omega a^\dagger a + \sum_n \frac{\omega_q^n}{2}\sigma_z^n + \frac{1}{N}\sum_n g_n \sigma_x^n \left(a^2 + a^{\dagger 2}\right), \tag{6.5}$$

can be implemented in a chain of N ions, generalizing such a method. The N qubits are represented by an internal electronic transition of each ion, while the bosonic mode is given by a collective motional mode of the ion chain. The two-phonon interactions are induced by a bichromatic laser driving with the same frequency-matching conditions used for the single-qubit case. The drivings can be implemented by shining two longitudinal lasers coupled to the whole chain, or by addressing the ions individually with transversal beams. The former solution is much less demanding, but it may introduce inhomogeneities in the coupling for very large ion chains; the latter allows complete control over individual coupling strengths.

In order to guarantee that the model of Eq. (6.5) is faithfully implemented, the bichromatic driving must not excite unwanted motional modes. In our proposal, the frequency of the red/blue drivings $\omega_{r/b}$ satisfy the relation $|\omega_{r/b} - \omega_{int}| = 2\nu + \delta_{r/b}$, where $\delta_{r/b}$ are small detunings that can be neglected for the present discussion. We recall that ν is the bosonic mode frequency and ω_{int} the qubit energy spacing. To be definite, we take the motion of the center of mass of the ion chain as the relevant bosonic mode. Then, the closest collective motional mode is the breathing mode [74], with frequency $\nu_2 = \sqrt{3}\nu$. An undesired interaction between the internal electronic transitions and the breathing mode could appear if $|\omega_{r/b} - \omega_{int}|$ is close to ν_2 or $2\nu_2$, corresponding to the first and second sidebands, respectively. In our case, the drivings are detuned by $\Delta_1 = |\omega_{r/b} - \omega_{int}| - \nu_2 \approx 0.27\nu$ from the first and $\Delta_2 = |\omega_{r/b} - \omega_{int}| - 2\nu_2 \approx 1.46\nu$ from the second sideband. Given that the frequency ν is much larger than the coupling strength Ω, such detunings make those unwanted processes safely negligible.

6.4 Real-time dynamics

Depending on the ratio between the normalized coupling strength g and the mode frequency ω, the model of Eq. (6.1) exhibits qualitatively different behaviors. Two parameter regimes can be identified accordingly. For the sake of simplicity, we will consider

the homogeneous coupling case $g_n = g$, $\omega_q^n = \omega_q$, for every n, and we will focus in the resonant or near-resonant case $\omega_q \approx 2\omega$.

In accordance with the quantum Rabi model, we define the strong coupling (SC) regime by the condition $g/\omega \ll 1$. Under this restriction, the RWA can be applied to the coupling terms, replacing each direct interaction $g\sum_n \sigma_x^n \left(a^2 + a^{\dagger 2}\right)$ with $g\sum_n \left(\sigma_+^n a^2 + \sigma_-^n a^{\dagger 2}\right)$, where we defined the raising/lowering single-qubit operators $\sigma_\pm^n = \left(\sigma_x^n \pm i\sigma_y^n\right)/2$.

When the RWA is valid, the system satisfies a continuous symmetry identified by the operator $\zeta = a^\dagger a + 2\sum_n \sigma_+^n \sigma_-^n$, corresponding to a weighed conservation of the total number of excitations, such that a spin flip is balanced by the creation or annihilation of two bosonic excitations. The presence of a continuous symmetry makes the model superintegrable [19]. In the SC regime, the interaction leads to two-photon excitation transfers between the bosonic field and the qubits, as shown in Fig. 6.1a. When the bosonic field is initially in a coherent state, Jaynes-Cummings-like collapses and revivals of population inversion are expected to appear [216, 217].

As the ratio g/ω increases, the intuitive dynamics of the SC regime disappears. Excitations are not conserved and the average value of observables like the boson number or the qubit occupation do not follow the pattern of coherent excitation transfer (see Fig. 6.1b and Fig. 6.1c). When the normalized coupling approaches the value $g \sim 0.1\omega$, the RWA cannot be performed, and the full quantum Rabi model must be taken into account. We define the ultrastrong coupling (USC) regime as the parameter region for which $0.1 \lesssim g/\omega < 0.5$. Even if analytical solutions for the system eigenstates have been derived [199–201], they hold only for $N = 1$, they are not in a closed form, and they do not entail computational benefits with respect to numerical simulations. Indeed, due to the large number of excitations involved in the dynamics, the two-photon Dicke model is demanding for classical numerical techniques.

In the SC/USC transition, the continuous symmetry ζ breaks down to a $\mathbb{Z}_4$ discrete symmetry identified by the parity operator

$$\Pi = (-1)^N \bigotimes_{n=1}^{N} \sigma_z^n \ \exp\left(i\frac{\pi}{2}a^\dagger a\right). \tag{6.6}$$

Four invariant Hilbert subspaces are identified by the four eigenvalues $\lambda = \{1, -1, i, -i\}$ of Π. Hence, for any coupling strength, the symmetry Π restricts the dynamics to parity chains, shown in Fig. 6.2a, for $N = 1, 2$. Notice that in the SC regime, the RWA confines the system to a very small number of states. On the contrary, when g is large enough to make counter-rotating terms relevant (USC regime), the system evolution spans a much larger Hilbert space.

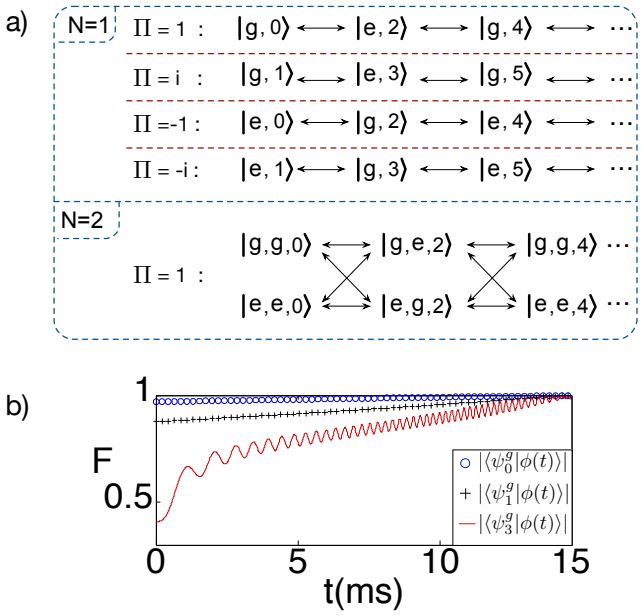

FIGURE 6.2: (a) Parity chains for $N = 1, 2$. For simplicity, for $N = 2$, only one parity subspace is shown. (b) Quantum state fidelity between the system state $|\phi(t)\rangle$ and the target eigenstates $|\psi_n^g\rangle$ during adiabatic evolution. The Hamiltonian at $t = 0$ is given by Eq. (6.1) with $N = 1$, $\omega_q/\omega = 1.9$ and $g = 0$. During the adiabatic process, the coupling strength is linearly increased until reaching the value $g/\omega = 0.49$. For the blue circles, the initial state is given by the ground state $|\phi(t = 0)\rangle = \left|\psi_0^{g=0}\right\rangle$. For black crosses, $|\phi(t = 0)\rangle = \left|\psi_1^{g=0}\right\rangle$, while for the red continuous line, $|\phi(t = 0)\rangle = \left|\psi_4^{g=0}\right\rangle$. The color code indicates parity as in Fig. 6.3a. Notice that, due to parity conservation, the fourth excited eigenstate $\left|\psi_4^{g=0}\right\rangle$ of the decoupled Hamiltonian is transformed into the third one $|\psi_3^g\rangle$ of the full Hamiltonian.

When the normalized coupling g approaches $g = \omega/2$ (see Fig 6.3c), the dynamics is dominated by the interaction term and it is characterized by photon production. Finally, when $g > \omega/2$, the Hamiltonian is not bounded from below. However, it still provides a well defined dynamics when applied for a limited time, like usual displacement or squeezing operators.

6.5 The spectrum

The eigenspectrum of the Hamiltonian of Eq. (6.1) is shown in Figs. 6.3a and 6.3c for $N = 1$ and $N = 3$, respectively. Different markers are used to identify the parity Π of each Hamiltonian eigenvector, see Eq. (6.6). In the SC regime, the spectrum is characterized by the linear dependence of the energy splittings, observed for small values of g. On the contrary, in the USC regime the spectrum is characterized by level crossings known as Juddian points, allowing for closed-form isolated solutions [205] in the single-qubit case.

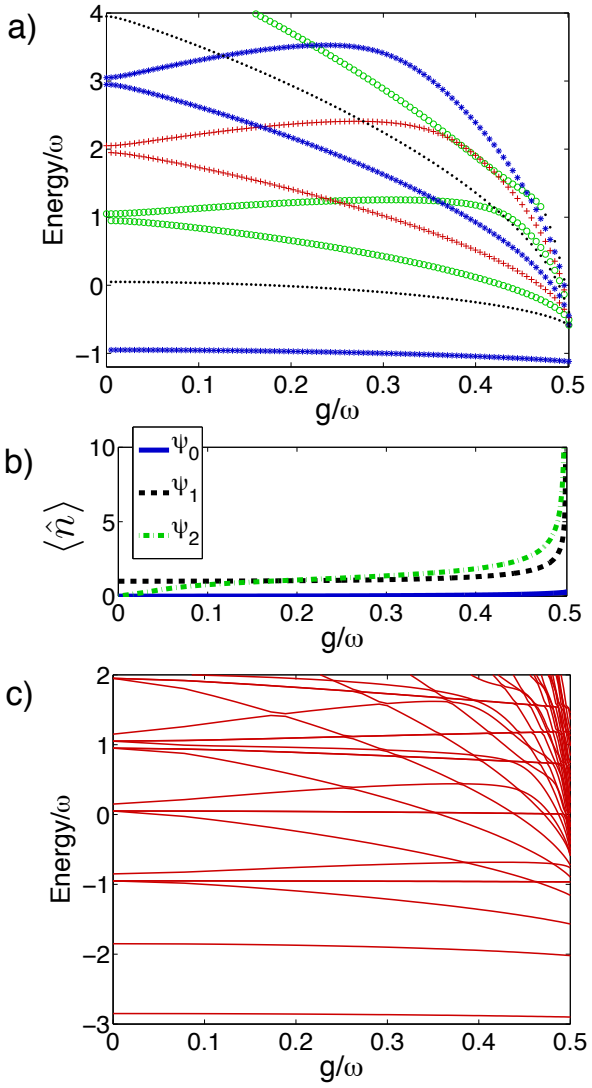

FIGURE 6.3: Spectral properties of the Hamiltonian Eq. (6.1), in units of ω, for $\omega_q = 1.9$, as a function of the coupling strength g. For $g > 0.5$, the spectrum is unbounded from below. (a) Spectrum for $N = 1$. Different markers identify the parity of each eigenstate: green circles for $p = 1$, red crosses for $p = i$, blue stars for $p = -1$, and black dots for $p = -i$. (b) Average photon number for the ground and first two excited states, for $N = 1$. (c) Spectrum for $N = 3$. For clarity, the parity of the eigenstates is not shown.

The most interesting spectral features appear when the normalized coupling g approaches the value $\omega/2$. In this case, the energy spacing between the system eigenergies asymptotically vanishes and the average photon number for the first excited eigenstates diverges (see Fig. 6.3b). When $g = \omega/2$, the discrete spectrum collapses into a continuous band, and its eigenfunctions are not normalizable. Beyond that value, the Hamiltonian is unbounded from below [204, 205]. This can be shown rewriting the bosonic components of Hamiltonian of Eq. (6.1) in terms of the effective position and momentum operators of a particle of mass m, defined as $\hat{x} = \sqrt{\frac{1}{2m\omega}}\left(a + a^\dagger\right)$ and $\hat{p} = i\sqrt{\frac{m\omega}{2}}\left(a - a^\dagger\right)$. Therefore,

we obtain

$$\begin{aligned}\mathcal{H} &= \frac{m\omega}{2}\left[(\omega - 2g\ \hat{S}_x)\frac{\hat{p}^2}{m^2\omega^2} + (\omega + 2g\ \hat{S}_x)\hat{x}^2\right] \\ &+ \frac{\omega_q}{2}\sum_n \sigma_z^n, \end{aligned} \tag{6.7}$$

where $\hat{S}_x = \frac{1}{N}\sum_n \sigma_x^n$. Notice that $\hat{S}_x$ can take values included in the interval $\langle S_x\rangle \in [-1, 1]$. Hence, the parameter $(\omega+2g)$ establishes the shape of the effective potential. For $g < \omega/2$, the particle experiences an always positive quadratic potential. For $g = \omega/2$, there are qubit states which turn the potential flat and the spectrum collapses (see appendix D), as for a free particle. Finally, when $g > \omega/2$, the effective quadratic potential can be positive, for $\langle \hat{S}_x\rangle < -\omega/2g$, or negative, for $\langle \hat{S}_x\rangle > \omega/2g$. Therefore, the Hamiltonian (6.7) has neither an upper nor a lower bound.

6.6 Measurement technique

A key experimental signature of the spectral collapse (see Fig. 6.3a) can be obtained by measuring the system eigenergies [218] when g approaches 0.5ω. Such a measurement could be done via the quantum phase estimation algorithm [219]. A more straightforward method consists in directly generating the system eigenstates [195] by means of the adiabatic protocol shown in Fig. 6.2b. When $g = 0$, the eigenstates $\left|\psi_n^{g=0}\right\rangle$ of Hamiltonian in Eq. (6.1) have an analytical form and can be easily generated [220]. Then, adiabatically increasing g, the eigenstates $|\psi_n^g\rangle$ of the full model can be produced. Notice that parity conservation protects the adiabatic switching at level crossings (see Fig. 6.2b).

Once a given eigenstate has been prepared, its energy can be inferred by measuring the expected value of the Hamiltonian in Eq. (6.1). We consider separately the measurement of each Hamiltonian term. The measurement of σ_z^n is standard in trapped-ion setups and is done with fluorescence techniques [210]. The measurement of the phonon number expectation value was already proposed in Ref. [67]. Notice that operators σ_z^n and $a^\dagger a$ commute with all transformations performed in the derivation of the model, hence their expectation values in the lab and simulation picture will coincide. The expectation value of the interaction term $g\sigma_x^n\left(a^2 + a^{\dagger 2}\right)$ can be mapped into the value of the first time derivative of $\langle\sigma_z^n\rangle$ at measurement time $t = 0$, with the system evolving under $\mathcal{H}_m = \omega a^\dagger a + \frac{\omega_q}{2}\sigma_z^n - g\sigma_y^n\left(a^2 + a^{\dagger 2}\right)$. This Hamiltonian is composed of a part $A = \omega a^\dagger a + \frac{\omega_q}{2}\sigma_z^n$ which conmutes with σ_z^n, $[A, \sigma_z^n] = 0$, and a part $B = -g\sigma_y^n\left(a^2 + a^{\dagger 2}\right)$

which anti-conmutes with σ_z^n, $\{B, \sigma_z^n\} = 0$, yielding

$$\langle e^{i(A+B)t}\sigma_z^n e^{-i(A+B)t}\rangle = \langle e^{i(A+B)t}e^{-i(A-B)t}\sigma_z^n\rangle. \tag{6.8}$$

The time derivative of this expression at $t = 0$ is given by

$$\langle [i(A+B) - i(A-B)]\sigma_z^n\rangle = 2i\langle B\sigma_z^n\rangle, \tag{6.9}$$

which is proportional to the expectation value of the interaction term of Hamiltonian in Eq. (6.4),

$$\partial_t\langle e^{i\mathcal{H}_m t}\sigma_z^n e^{-i\mathcal{H}_m t}\rangle|_{t=0} = 2\langle g\sigma_x^n\left(a^2 + a^{\dagger 2}\right)\rangle. \tag{6.10}$$

The evolution under Hamiltonian $\mathcal{H}_m$ in the simulation picture is implemented just in the same way as with Hamiltonian of Eq. (6.4), but selecting the laser phases ϕ_j to be $\frac{\pi}{2}$. Moreover, expectation values for the parity operator Π of Eq. (6.6) can be extracted following techniques described in appendix D.

6.7 Conclusions

We have introduced a trapped-ion scheme that allows to experimentally investigate two-photon interactions in unexplored regimes of light-matter coupling, replacing photons of the model by trapped-ion phonons. It provides a feasible method to observe an interaction-induced spectral collapse in a two-phonon quantum Rabi model, approaching recent mathematical and physical results with current quantum technologies. The proposed scheme provides a scalable quantum simulator of a complex quantum system, which is difficult to approach with classical numerical simulations even for low number of qubits, due to the large number of phonons involved in the dynamics. Furthermore, the two-photon Dicke model may present a very interesting phase diagram. As the standard Dicke model, the two-photon Dicke is expected to show a superradiant phase transition, when the coupling strength reaches a critical value. However, the phase transition could be inhibited by the spectral collapse, if the latter happens for smaller values of the coupling strength. The interplay between these two effects is expected to have a non-trivial dependence on the ratios between the coupling strength and the field and qubit frequencies. These predictions show the vital aspects of the quantum Rabi model and promise an open avenue for further interesting physics in theory and experiments.

Chapter 7

The quantum Rabi model in periodic phase space with cold atoms

7.1 Introduction

In previous chapters, we have introduced methods to implement the quantum Rabi model, and generalizations of it, in trapped-ions systems. This quantum technology has been widely adopted to reproduce the physics of light-matter interactions of small quantum systems, using the ions internal and vibrational degrees of freedom. On the other hand, systems of cold atoms have mostly been associated, for their own nature, with the implementation of quantum many-body systems. Like for trapped-ions, spin-like degrees of freedom have been implemented with cold atoms using internal electronic transitions. Alternatively, two-level systems have been created using atomic quantum dots [221, 222] or double-well potentials [223].

In this chapter, we propose a quantum simulation of the QRM with cold atoms loaded onto a periodic lattice, using an unconventional definition of qubit. The effective two-level quantum system is simulated by the occupation of different Bloch bands, and the bosonic mode is represented by the motion of the atomic cloud into a Harmonic optical-trap potential. The qubit energy spacing is proportional to the periodic lattice depth, while the interaction with the bosonic mode is intrinsic in the qubit definition.

We show that our method, feasible with current technology, can access extreme parameters regimes of the QRM, allowing the experimental study of the transition between the USC and DSC regimes. Furthermore, the proposed system provides a generalization

of the QRM in periodic phase space that presents an interesting pattern of collapses and revivals in the DSC regime. An interesting feature of this proposal is that each atom of the non-interacting cloud simulates the QRM Hamiltonian. Thus, in any simulation run, an ensemble of QRM evolves simultaneously. This allows to obtain the bosonic mode quadrature distribution with a single collective measurement, and it could lead to interesting many-body generalization of the model when inter-atom interactions are introduced.

This chapter is organized as follows. In section 7.2, we introduce the model and we discuss the analogy with the QRM. In section 7.3, we provide details on the proposed implementation, discussing the parameter regimes that can be accessed with nowadays technology and the measurement techniques. In section 7.4, we report the results of numerical simulations that show examples of interesting dynamics that could be reproduced. Finally, in section 7.5 we summarize our results.

7.2 The model

The system here considered is composed of a cloud of ultracold atoms exposed to two laser-induced potentials: a periodic lattice and a harmonic trap[1]. When the atom density is sufficiently low, interactions among the atoms are negligible, and the system can be described with a single-particle Hamiltonian, composed of the sum of a harmonic part H_{P} and a quadratic term

$$\hat{H} = \hat{H}_{\mathrm{P}} + \frac{m\omega_0^2}{2}\hat{x}^2 \ , \qquad \hat{H}_{\mathrm{P}} = \frac{\hat{p}^2}{2m} + \frac{V}{2}\cos\left(4k_0\hat{x}\right) \tag{7.1}$$

where, $\hat{p} = -i\hbar\frac{\partial}{\partial x}$ and $\hat{x}$ are momentum and position of an atom of mass m, respectively. Here, ω_0 is the angular frequency of the atom motion in the harmonic trap, while V and $4k_0$ are the depth and wavevector of the periodic potential, respectively. The periodic lattice is resulting from a four-photon interaction with a driving field [224–226] of wavevector k_0 .

In the following, we will assume that the harmonic trap is slowly varying on the length-scale of the periodic potential. Under this assumption, the most suitable basis is given by the Bloch functions

$$\langle x\,|\phi_n(q)\rangle = \phi_n(q,x) = e^{iqx/\hbar}u_n(q,x), \tag{7.2}$$

[1]Details on the implementation can be found in section 7.3.

where q is the quasi-momentum and n is the band index, while $u_n(q,x)$ must be a periodic function with the same periodicity of the periodic potential. Accordingly, we define $u_n(q,x) = e^{-i2k_0x}e^{i4nk_0x}$. We have added the phase e^{-i2k_0x} to the $u_n(q,x)$ functions definition in order to obtain a convenient first Brillouin zone, $q \in [-2\hbar k_0, 2\hbar k_0]$. Notice that the Bloch functions are identified by a discrete quantum number, the band index n, and a continuous variable, the quasi-momentum q. Accordingly, we can define a continuous and a discrete degrees of freedom, and rewrite the Bloch basis of Eq 7.2 as $|\phi_n(q)\rangle = |q\rangle\,|n\rangle$.

First, let us consider the periodic part $\hat{H}_p$ of the system Hamiltonian , later we will discuss the effect of the harmonic trap. It is straightforward to see that the momentum operator is diagonal in the Bloch basis, while the periodic potential introduces a coupling between adjacent bands

$$\begin{aligned}\hat{H}_p\,|q\rangle\,|n\rangle &= \frac{1}{2m}\big[q+(2n-1)2\hbar k_0\big]^2\,|q\rangle\,|n\rangle \\ &\quad +\frac{V}{4}\Big(\,|q\rangle\,|n+1\rangle + |q\rangle\,|n-1\rangle\,\Big).\end{aligned} \tag{7.3}$$

Assuming that the system dynamics is restricted to the two bands with lowest energy, the periodic part $H_{\rm P}$ of the Hamiltonian can be rewritten in the Bloch basis as

$$\hat{H}_{\rm P}(q) = \frac{1}{2m}\begin{pmatrix} q^2+4\hbar k_0\;q & 0 \\ 0 & q^2-4\hbar k_0\;q\end{pmatrix} + \frac{V}{4}\begin{pmatrix}0 & 1\\ 1 & 0\end{pmatrix}. \tag{7.4}$$

Equivalently, using the Pauli matrices formalism to describe the two-fold Hilbert space defined by the first two bands, we can write

$$\hat{H}_{\rm P}(q) = \frac{q^2}{2m} + \frac{2\hbar k_0}{m}\sigma_z\;q + \frac{V}{4}\sigma_x. \tag{7.5}$$

Hence, the periodic potential introduces the free energy term of an effective two-level quantum system.

Let us now include the quadratic term of Eq. (7.1) in our treatment. In the Bloch basis, we can write

$$\langle\tilde{q},\tilde{n}|\hat{x}^2|q,n\rangle = \int_{-\infty}^{+\infty} dx\,x^2 e^{i[4(n-\tilde{n})k_0+(q-\tilde{q})/\hbar]x}. \tag{7.6}$$

Considering diagonal elements in the qubit Hilbert space, i.e., setting $\tilde{n}=n$, we have

$$\langle\tilde{q},n|\hat{x}^2|q,n\rangle = \int_{-\infty}^{+\infty} dx\,x^2 e^{i(q-\tilde{q})x/\hbar}, \tag{7.7}$$

and so

$$\frac{m\omega_0^2}{2}\langle\tilde{q},n|\hat{x}^2|q,n\rangle = -\frac{m\hbar^2\omega_0^2}{2}\langle\tilde{q},n|\frac{\partial^2}{\partial q^2}|q,n\rangle. \tag{7.8}$$

Hence, we see that the harmonic potential introduces an operator, diagonal in the qubit Hilbert space, which can be expressed as $\hat{r} = -i\hbar\frac{\partial}{\partial q}$, in the Bloch basis. This allows us to define the quasimomentum operator $\hat{q}$ and the position operator $\hat{r}$, which satisfy the commutation relation $[\hat{r},\hat{q}] = i\hbar$. On the other hand, for $\tilde{n} \neq n$, the integral in Eq. (7.6) is different from zero only if $4\hbar k_0(n-\tilde{n}) = \tilde{q} - q$. Hence, the quadratic potential introduces a coupling between neighbouring bands, for states whose momenta satisfy $\tilde{q} - q = 4\hbar k_0$, of the kind

$$\frac{m\omega_0}{2}\hat{r}^2\Big(|2\hbar k_0,0\rangle\langle -2\hbar k_0,1| + |2\hbar k_0,1\rangle\langle -2\hbar k_0,0| + \text{H.}c.\Big). \tag{7.9}$$

This effective coupling is due to the periodicity of the quasimomentum, which mixes the bands $n = 0, 1$ at the boundaries of the Brillouin zone. Such a coupling can be neglected as far as the system dynamics involves only values of the quasimomentum $\hat{q}$ included within the first Brillouin zone.

7.2.1 Equivalence with the quantum Rabi model

Let us now rewrite the Hamiltonian of Eq. (7.1) as

$$\hat{H} = \frac{\hat{q}^2}{2m} + \frac{m\omega_0^2}{2}\hat{r}^2 + \frac{2\hbar k_0}{m}\sigma_z\ \hat{q} + \frac{V}{4}\sigma_x. \tag{7.10}$$

Defining creation a and annihilation $a^\dagger$ operators $\hat{a} = \sqrt{\frac{m\omega_0}{2\hbar}}\left(\hat{r} + \frac{i}{m\omega_0}\hat{q}\right)$, and rotating the qubit basis with the unitary operator $U = \frac{1}{\sqrt{2}}\begin{pmatrix}1 & -1\\ 1 & 1\end{pmatrix}$, the total system Hamiltonian can be finally rewritten as

$$\hat{H} = \hbar\omega_0 a^\dagger a + \frac{\hbar\omega_q}{2}\sigma_z + i\hbar g\sigma_x\left(a^\dagger - a\right). \tag{7.11}$$

which corresponds to the quantum Rabi Hamiltonian. In the following, we will refer to this rotated basis to use a notation for the Pauli matrices consistent with the previous chapters. We have defined the effective qubit energy spacing $\omega_q = \frac{V}{2\hbar}$ and the interaction strength $g = 2k_0\sqrt{\frac{\hbar\omega_0}{2m}}$. Notice that, in the standard form of the QRM, the qubit-field coupling is usually written in terms of the position operator, while in Eq. (7.11) it appears in terms of the momentum operator. The two definitions are equivalent up to a global phase factor.

The full system Hamiltonian of Eq. (7.1) resembles the QRM only when the effective coupling of Eq. (7.9) between different bands induced by the harmonic potential can be neglected. Such an approximation holds until the system wavefunction $\langle q\,|\psi(t)\rangle$ is completely included in the first Brillouin zone at any evolution time. Clearly, this constraint limits the proposed implementation to values of the momentum $\hat{q}$ smaller in modulus than $2\hbar k_0$. As in any quantum simulation, the dynamics is restricted into a validity region. In the following, we will show that this constraint does not impede to observe the highly non-trivial behavior of the QRM in the USC and DSC regimes. Interestingly, some key features of the DSC regime are reproduced even when the periodicity of the quasimomentum becomes relevant for the system dynamics.

7.3 Implementation

Before going into details of the phenomena that can be observed, let us discuss the feasibility of the present proposal. In this section, we report which parameter regimes can be accessed with nowadays technology, and we briefly describe state preparation and measurement techniques. In particular, we consider previous experiments of ultracold rubidium atoms in optical lattices [227], where Fourier-synthetized lattice potentials are used in order to taylor the atomic dispersion relation [110, 228].

7.3.1 Accessibility of parameter regimes with cold atoms

The parameter regimes that can be accessed are established by the relative weights of the parameters ω_0, $\omega_q = \frac{V}{2\hbar}$ and $g = 2k_0\sqrt{\frac{\hbar\omega_0}{2m}}$, defined in Eq. (7.11). We will consider as fixed parameters the wavelength of the lattice laser $\lambda = 783.5 \times 10^{-9}$ m, for technical reasons, and, obviously, the Rubidium atomic mass $m = 1.44\times10^{-25}$ Kg. The wavevector is given by $k_0 = \frac{2\pi}{\lambda}$. On the other hand, the periodic lattice can be tuned over a wide intensity range, from $V = 0$ (absence of lattice), to about $V/\hbar = 2\pi \times 18$ KHz, corresponding to $V = 4.8E_r$, where we defined the recoil energy $E_r = \frac{\hbar^2 k_0^2}{2m}$. The frequency of the harmonic trap can also be tuned from $w_0 = 2\pi \times 0.5$ KHz, to $\omega_0 = 2\pi$ KHz.

As for the previous chapters, concerning the QRM we will set $\hbar = 1$ and we will use units of ω_0. First, notice that the value of the effective coupling strength is intrinsically linked to the trap frequency $g \sim \sqrt{\omega_0}$, hence the ratio g/ω_0 is tunable only over a narrow range of extremely high values, from $g/\omega_0 \approx 7\omega_0$ to $g/\omega_0 \approx 11$. However, the tunability of the ratio between the coupling strength and the effective qubit energy spacing allows us to explore both the USC and DSC dynamics, as shown below in section 7.4. Indeed,

the value of ω_a can be made large enough to make the qubit free Hamiltonian dominant, $g/\omega_a \approx 0.3$, or small enough to make its energy contribution negligible.

7.3.2 State preparation and measurement

Initially, the rubidium atoms are cooled to quantum degeneracy via evaporation in an optical mid-infrared dipole trap. After the cooling process, a Bose-Einstein condensate is generated, with about 6×10^4 atoms in the $m_F = 0$ Zeeman sublevel of the $F = 1$ hyperfine ground state component [227]. After this initialization, the momentum of the atoms must be manipulated, in order to produce relevant states of the simulated qubit and bosonic mode as encoded in section 7.2.1.

Notice that the qubit state is encoded in the occupation of the Bloch bands $|\pm 2\hbar k_0\rangle$, while the bosonic mode quadratures are encoded in the position $\hat{r}$ and quasimomentum $\hat{q}$ of the atoms. To prepare the atoms in the desired position of the Bloch spectrum two techniques can be used. The first one consists in deactivating for a short time the trapping potential, so that the atomic cloud is left in free fall [110]. In this way, it is possible to accelerate the atoms by a small, continuously-tunable amount of quasimomentum, due to the earth gravitational field. The second technique consists in applying a Doppler-sensitive Raman pulse [224], transferring the atoms from the $m_F = 0$ to the $m_F = -1$ Zeeman sublevel, thus applying a discrete momentum kick of $\pm 2\hbar k_0$. By controlling the share of atoms that gain positive or negative momentum, the effective qubit can be initialized in any eigenstates of σ_x (as defined in Eq. (7.11)).

Via standard time-of-flight measurement [229], both the momentum and, in principle, the position distribution of the atoms can be measured, as well as the occupation state of σ_x. Such a technique consists in switching off abruptly both the lattice and the trapping potential, in such a way that the atoms can freely expand according to their momentum distribution. After a definite time of flight, the atom positions can be detected using standard absorption imaging methods. Hence, their initial momentum and position distribution can be deduced, thus obtaining both the simulated boson wavefunction and the projection of the effective qubit state on the eigenstates of σ_x. Knowing the momentum and position distribution of the simulated field quadratures $\hat{q}$ and $\hat{r}$, the average photon number $\hat{N} = a^\dagger a$ can also be obtained (see definition of the simulated ladder operators in section 7.2.1). However, while the reconstruction of the momentum distribution can be performed with high precision [110], achieving the required resolution on the measurement of the atoms initial position can be experimentally challenging.

For completeness, we mention that the qubit operator σ_z can be also be directly measured via adiabatic mapping [229, 230], but only when the system state is close to the avoided crossing in the Bloch spectrum. This technique consists in adiabatically ramping down the lattice potential depth, in order to preserve the quasimomentum q. During the turn-off process, a Bloch wave in the nth energy band is mapped onto a corresponding free-particle momentum p in the nth Brillouin zone.

7.4 Ultrastrong and deep strong coupling regime

Let us now consider the dynamics of the QRM in the specific parameter regime of interest for the proposed quantum simulation. Given that only very high values of the ratio between the coupling strength g and the bosonic mode frequency ω_0 are accessible, the rotating wave approximation can never be applied and the model cannot be implemented in the Jaynes-Cummings limit. However, we will show that interesting dynamics at the crossover between the USC and the DSC regime can be observed, for values of parameters that are unattainable with any natural implementations of the quantum Rabi model.

By means of numerical simulations, we have compared the dynamics of the full cold atoms model of Eq. (7.1) with the corresponding effective QRM, Eq. (7.11). Numerical simulations of the full model have been performed in the position basis, applying a discretization of the real space over more than 10^3 lattice sites. The QRM model has been numerically simulated introducing a cut-off ($N > 500$) on the maximum number of photons allowed into the system.

In Fig. 7.1, we show the results of such numerical simulations, in different parameter regimes. The initial state $|\psi_0\rangle = |0\rangle |+\rangle$ is given by the vacuum of the bosonic mode and the σ_x eigenvector of positive eigenvalue. Such a state corresponds to the atomic cloud at the center of the trap and at the position $p = 2\hbar k_0$ (or $q = 0$) of the Bloch spectrum, and it can be reliably generated as detailed in section 7.3.2. In all plots, the red continuous line shows the dynamics of the full model, while the dashed blue line corresponds to the QRM. The very good agreement between the two simulations suddenly breaks down when the system state hits the border of the validity region of the quantum simulation. Different behaviors between the two regimes are more visible in the expected value of σ_x which, in the DSC regime, is approximatively a conserved quantity, as shown in the following section.

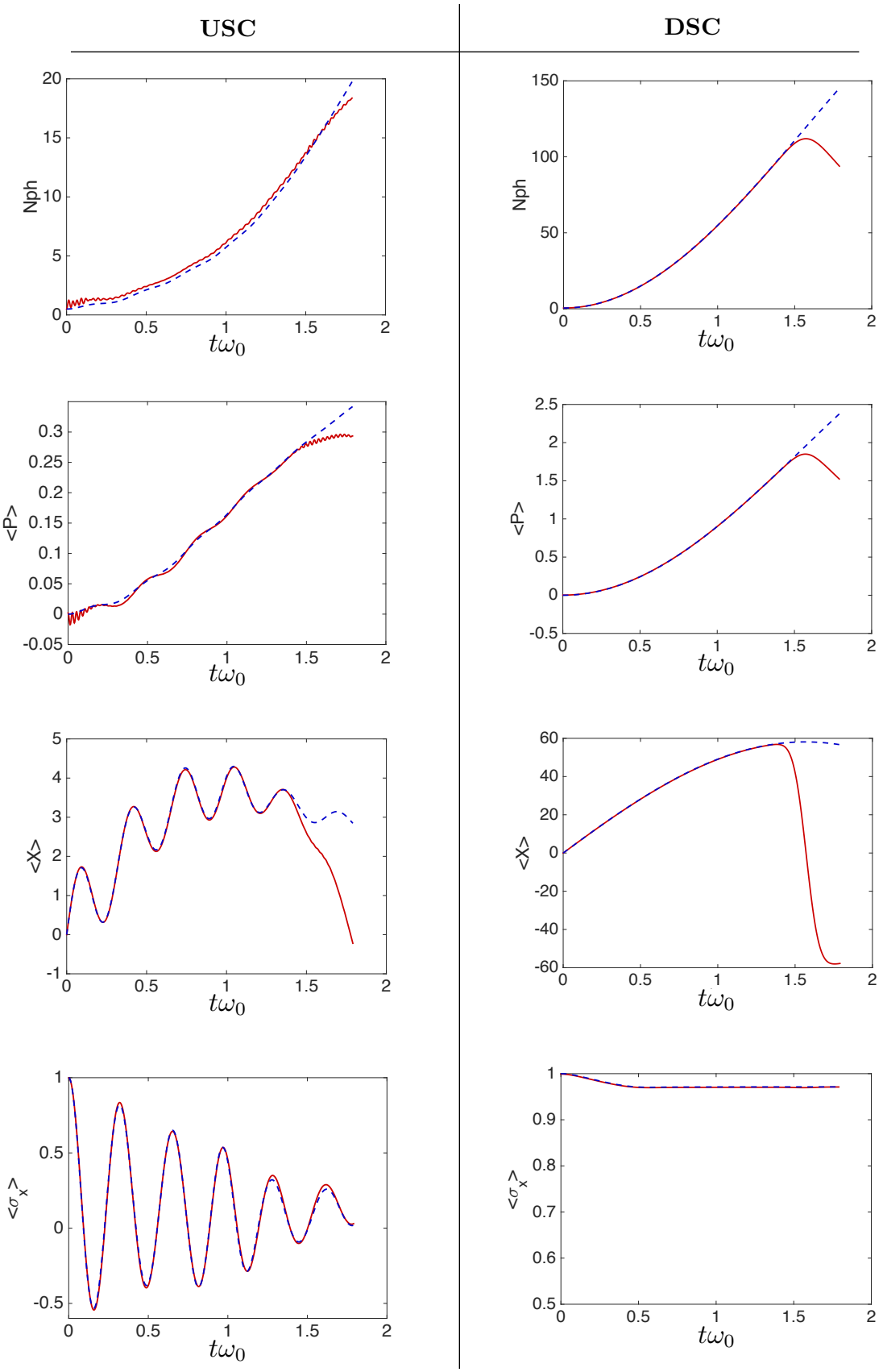

FIGURE 7.1: Comparison between the full cold atom Hamiltonian (red continuous line) and the QRM (red dashed line). The momentum is shown in units of $\hbar k_0$, while the position in units of $1/k_0$. For the USC regime, the Rabi parameters are given by $g/\omega_0 = 7.7$ and $g/\omega_a = 0.43$ while, for the DSC regime, $g/\omega_0 = 10$ and $\omega_0 = \omega_a$.

7.4.1 Collapse and revival

In the previous section, we have shown that our proposal is able to reproduce the dynamics of the QRM at the crossover between the USC and DSC regimes. We have also shown that the analogy is broken when the value of the simulated momentum exceeds the borders of the first Brillouin zone. When this is the case, the model represents a generalization of the QRM in a periodic phase space. In the following, we analyze the properties of such a model. In particular, we focus on collapses and revivals of the initial state, which represent the signature of the QRM in the DSC regime.

The system enters the deep strong coupling regime [42] when both the ratio g/ω_0 and g/ω_a are significant higher than 1. Under this condition, the system time evolution is well described by the slow-qubit approximation, which consists in neglecting the energy splitting of the qubit, setting $\omega_a = 0$. In our case, the Hamiltonian of Eq. (7.11) will be reshaped into $\hat{H}_{DSC} = \omega_0 a^\dagger a - ig\sigma_x(a^\dagger - a)$. This approximation is intuitively motivated by the rapid growth of the number of photons, which makes the higher states of the Fock basis the most relevant in the system dynamics. Given that the norms of the creation and annihilation operators is proportional to the Fock number, while the Hamiltonian term $\frac{\omega_a}{2}\sigma_z$ remains constant, the latter becomes negligible for high photon number states.

Under this approximation, the Hamiltonian can be diagonalized using the transformation

$$C_D^\dagger(\alpha) H_{DSC} C_D(\alpha) = \omega_0 a^\dagger a + \frac{g^2}{\omega_0^2} - \frac{2g^2}{\omega_0}, \quad \text{with} \quad \alpha = -\frac{g}{\omega_0}\sigma_x, \tag{7.12}$$

where we defined the operator $C_D(\alpha) = \exp\left\{\alpha a^\dagger - \alpha^* a\right\}$, which corresponds to a conditional displacement dependent on the qubit state. If we consider the initial state $|\psi_{in}\rangle = |0\rangle|\pm\rangle$, using Eq. (7.12) it is straightforward to obtain an analytic expression

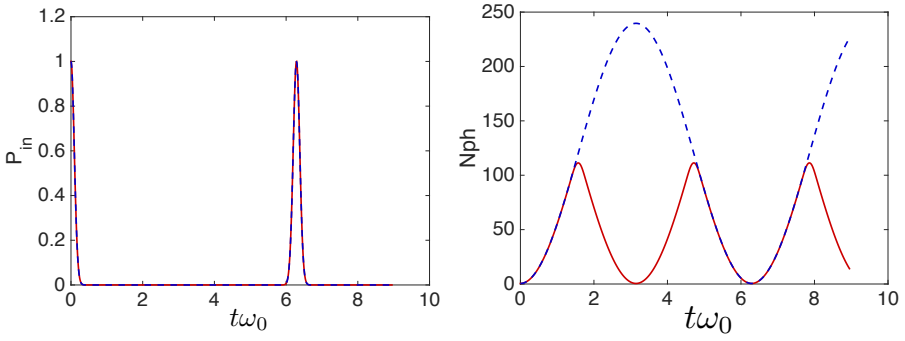

FIGURE 7.2: Comparison between the full cold atom Hamiltonian (red continuous line) and the QRM (blue dashed line). The plot shows collapses and revivals of the population of the initial state $P_{in} = |\langle\psi_{in}|\psi(t)\rangle|^2$ and of the average photon number. The initial state is given by $|\psi_{in}\rangle = |0\rangle|+\rangle$. The coupling strength is given by $g \sim 11\omega_0$, while the qubit energy spacing vanishes $\omega_a = 0$. In this trivial limit, collapses and revivals corresponds to harmonic oscillations of the atoms in the trap potential.

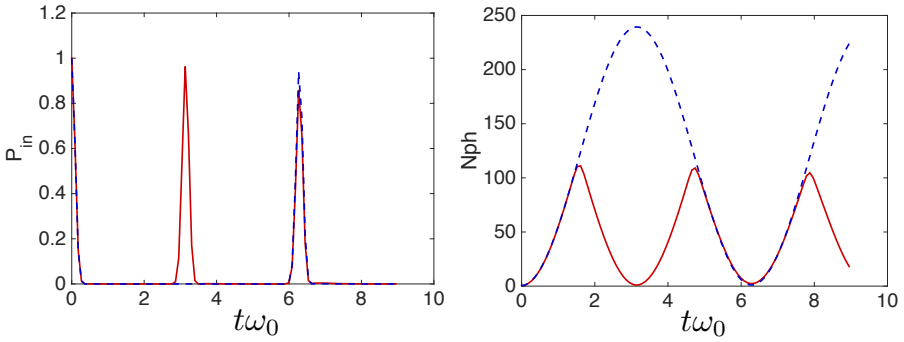

FIGURE 7.3: Comparison between the full cold atom Hamiltonian (red continuous line) and the QRM (blue dashed line). The plot shows collapses and revivals of the population of the initial state $P_{in} = |\langle\psi_{in}|\psi(t)\rangle|^2$ and of the average photon number. The initial state is given by $|\psi_{in}\rangle = |0\rangle|+\rangle$. The coupling strength is given by $g \sim 11\omega_0$, and the qubit is resonant with the simulated bosonic mode $\omega_a = \omega_0$. Notice that the extension of the QRM to a periodic phase space also presents collapse and revival, in this case with half the periodicity of the standard quantum Rabi model.

for the system evolution,

$$|\psi(t)\rangle = e^{-iH_{DSC}t}|\psi_{in}\rangle = e^{-i\phi(t)}D(\beta(t))|0\rangle|\pm\rangle\,, \tag{7.13}$$

where $\phi(t)$ is a global phase (independent of the qubit state), while $D(\beta(t))$ is a displacement operator and $\beta(t) = \pm\frac{g}{\omega_0}\left(e^{-i\omega_0 t} - 1\right)$. Accordingly, during the system time evolution σ_z is conserved, while the vacuum state is displaced into a coherent state that rotates in the phase space and with period $T = 2\pi/\omega_0$ returns into the initial state. This pattern of collapse and revival is shown in Fig. 7.2 , for the case in which the diagonalization of Eq. (7.12) is exact ($\omega_a = 0$), and in Fig. 7.3 for the resonant DSC regime ($\omega_a = \omega_0$).

Interestingly, the full model also presents a non-trivial scheme of collapses and revivals of the initial state. When the term σ_z is absent ($\omega_a = 0$), the system matches the collapses and revivals of the standard QRM, as shown in Fig. 7.2. This situations corresponds to harmonic oscillations of the atoms in the trap, in the case in which the periodic lattice is absent. When the term σ_z is turned on, peaks in the overlap P_{in} appear also at half oscillation period. This phenomenon, shown in Fig. 7.3, is due to the periodicity of the quasimomentum and to the specific definition of the effective qubit (see section 7.2.1). After half oscillation period, the quasimomentum comes back to its initial value, but the qubit experience a spin flip in the σ_x basis. The effect of the σ_z term can rectify this flip, so that the qubit as well is projected back on the initial state.

7.5 Conclusions

In this chapter, we have developed a method to implement a quantum simulation of the QRM using a system of cold atoms in a periodic lattice. An effective two-level quantum system is simulated by the Bloch-bands occupation, while a single bosonic mode is implemented by the oscillations of the atoms in a harmonic optical trap. The analogy with the QRM holds only within a finite region of the simulated boson phase space. However, by means of numerical simulations, we have shown that highly non-trivial dynamics can be feasibly implemented within the validity region of the quantum simulation. In particular, we have shown that the crossover between the USC and the DSC regime could be experimentally analyzed, for values of the parameters that are unachievable with natural implementations of the QRM. Furthermore, the proposed system represents a generalization of the QRM in a periodic phase space, which presents interesting patterns of collapses and revivals of the initial state in the DSC regime.

Chapter 8

Conclusions

In this Thesis, we have analyzed different aspects of the ultrastrong coupling (USC) regime of light-matter interactions. Our results can be gathered in two thematic research areas. From one side, we have studied how entering the USC regime modifies fundamental phenomena related to excitation transfer and entanglement generation. Furthermore, we have developed a method for measuring and controlling qubit-cavity systems, circumventing the lack of decoupling mechanisms in the USC regime. In these works, we have considered models that can be feasibly implemented in circuit quantum electrodynamics (QED) architectures, with current technology or with foreseeable improvements. In the cases in which the circuit designs represent themselves original contributions, we also provide derivations of the circuit quantization and details of the proposed implementations.

On the other hand, we have focused on developing methods for reproducing fundamental models of light-matter interaction, in all relevant regimes, as effective models in quantum-optical atomic systems. In particular, we propose three experimental implementations, considering systems of trapped ions and of ultracold atoms. These proposals are tailored in order to exploit specific features of the quantum platforms taken into account. For example, we show that the record-breaking controllability of trapped ions allows to generate arbitrary superpositions of eigenstates of the quantum Rabi model (QRM), and to observe signatures of the spectral collapse induced by two-photon interactions. Likewise, the ability of loading atomic clouds on superposition of harmonic and periodic optical potentials allows to reach the deep strong coupling (DSC) regime, where the interaction strength is even larger than the bosonic mode frequency.

Let us discuss our results in more details, in particular focusing on the scope and on interesting future research directions. In chapter 2, we have considered the simplest system that could show fundamental features of excitation transfer in the SC-USC regime

crossover, namely, a three-cavity array containing a qubit in the central site. We have shown that, while in the SC regime excitation tunnelling has a linear behavior with respect to the qubit-cavity strength g, in the USC a much richer scenario emerges. In particular, complete excitation transfer is possible for any coupling strength, but there is a critical value for which transfer is inhibited and the tunnelling time diverge. Furthermore, a discontinuity in the tunnelling time allows us to derive an operational definition for the SC/USC transition. A natural generalization of these results would be to consider scattering on qubits embedded in longer arrays which, in the limit of a large number of cavities, approximate a continuum of bosonic modes. As this Thesis is being redacted, first steps in this direction have already been undertaken [231], using numerical techniques based on Matrix Product States.

In chapter 3, we have introduced a circuit design where the fast modulation of electrical boundary conditions generates highly entangled states of superconducting qubits, in arrays of transmission line resonators. Our main goal was to show that the dynamical Casimir effect (DCE) could be used as a tool for quantum information protocols, and that its circuit implementation could lead to a generalization to the multipartite case. Indeed, we have shown that genuinely multipartite entangled states can also be generated via fast modulation of boundary conditions. In this framework, we have shown that a qubit interacting in the USC regime with a resonator strongly modifies the mode structure of the latter. The resulting anharmonicity limits the system to a low-energy subspace, where the modulation of electrical boundary conditions can be used to generate maximally entangled states of collective excitations called polaritons. The proposed scheme leads the way to two interesting research lines. On one side, it can be used as a building block for creating networks [62] of entangled quantum resonators [232]. On the other, it paves the way to the use of the DCE as a tool [233] in feasible implementations.

Previously, we have discussed how entanglement between USC polaritons can be generated in an array of superconducting resonators. However, detecting such entanglement could be challenging, as the lack of decoupling mechanisms makes standard measurement techniques, like dispersive read-out, challenging in the USC regime. In order to address this issue, in chapter 4, we have developed a method to perform spectroscopy, quantum state tomography and state engineering on a qubit-cavity system, for any coupling strength and using an auxiliary qubit as a probe. The probe qubit interacts with the cavity in the SC regime, and we assume that we can tune its energy splitting and reliably implement state preparation and projective measurements. Such requirements are well within the reach of state-of-the-art superconducting qubit technology. The proposed method could be used to measure the parity inversion of the system eigenstates, a clear signature of the USC regime. More generally, it widens the

possibilities of using the advantages of the USC regime in practical implementation of quantum information protocols.

In chapter 5 and 6, we have proposed the implementation of the quantum Rabi and two-photon Rabi models in trapped ions. The technique we have developed consists in engineering the system Hamiltonian, using tunable optical drivings, in such a way that the target model is obtained in a given interaction picture. In order to make such implementations faithful, we have shown that it is indeed possible to measure all interesting observables as they are defined in the relevant interaction picture. The proposed method allows to reproduced the desired models in a broad spectrum of regimes, providing individual real-time tunability of all system parameters. The interest in implementing the QRM in trapped ions is due to the possibility of generating and measuring the model eigenstates, in a quantum platform where state preparation and detection can be done with outstanding precision, and independent measurements of qubit and bosonic observables can be performed.

The two-photon Rabi model is relevant due to its rich dynamics and for novel, counterintuitive spectral features, obtained in the USC regime. When the coupling strength approaches a critical value, all energy levels become degenerate, and the discrete spectrum collapses in a continuous band. The implementation of our method would allow to experimentally observe a signature of this collapse. Furthermore, we have shown that our scheme can be generalized to include more qubits, using a chain of trapped ions. The resulting many-body system, dubbed two-photon Dicke, is challenging to simulate with classical resources, due to the large Hilbert space span during the system evolution. The two-photon Dicke presents spectral collapse as well, and we want to stress out that a study of the phase diagram of this model is still missing. In particular, it is not known wether this model entails a superradiant phase transition, like the standard Dicke model, or wether the spectral collapse prevents it to happen.

Finally, in chapter 7, we have shown how the QRM could be implemented using ultracold atoms technology. In this case, a bosonic mode is implemented in the motion of the atomic cloud in a harmonic optical potential, while an effective two-level quantum systems is codified in the occupation of the two bands involved in the system dynamics. This scheme allows to implement the QRM in the DSC regime for unprecedented values of the coupling strength. Furthermore, it provides an interesting generalization of the QRM to a periodic phase space, which presents a pattern of collapses and revivals more complex than the standard QRM.

To conclude, we believe that the results presented in this Thesis broaden our understanding of a variety of physical phenomena related to the USC regime of light-matter interaction. Furthermore, we propose compelling methods that allow to observe those

phenomena in atomic quantum platforms. The first experimental demonstrations of the USC regime have been implemented only recently, and we expect that the interest and relevance of this promising field will grow as more theoretical developments and experimental groups in the world become involved in it. The next challenges, on the experimental side, are to improve the characterization and control of superconducting USC systems, and to achieve this regime in different quantum technologies. In this direction, solid state devices supporting surface acoustic waves [31] represent a convincing candidate, as the coupling of these systems with superconducting qubits can be boosted using piezoelectric materials. On the theoretical side, fundamental issues related to the role of the diamagnetic term [64] and to the breakdown of the Purcell effect [34] are still open, and far from being thoroughly solved.

Appendices

Appendix A

Further details on state transfer

In chapter 2, we have studied the transfer of a single field excitation along an array of three cavities, where the central one contains a qubit interacting in the USC regime. In this appendix, we extend our treatment to consider state transfer for a superposition state, section A.1, and for a coherent state, section A.2.

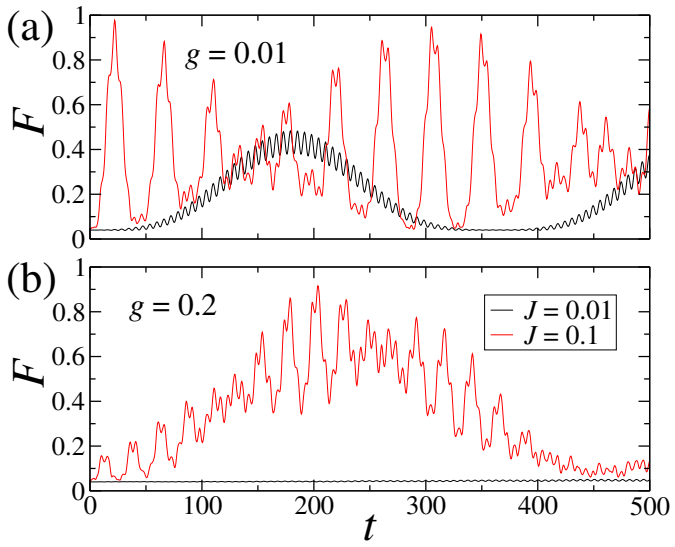

FIGURE A.1: (a) State transfer fidelity $F = \mathrm{Tr}\left[\rho_0 \rho(t)\right]$ over time for different system parameters. We define $|\phi_0\rangle = p\,|0\rangle + e^{i\theta}\sqrt{1-p^2}\,|1\rangle$, with $p = 0.2$ and $\theta = 0.63$. In the SC regime, that is when $g = J = 0.01$ (black line), the state transfer fidelity is bounded: it cannot reach 1 as far as $g \neq 0$. (b) When counter-rotating terms are involved in the dynamics ($J \gtrsim 0.1$ and/or $g \gtrsim 0.1$), the fidelity can be close to 1 even when $J < g$ (red line). Time is expressed in units of ω^{-1}.

A.1 Linear superposition

Here, we consider the state transfer of a Fock state linear superposition $|0\rangle$ and $|1\rangle$, containing zero and one excitations of the cavity mode, respectively. For simplicity, we have considered homogeneous cavity-cavity couplings, J_1=J_2, and resonance condition, $\omega_q = \omega$. The system is initialized in state $|\psi_0\rangle = |\phi_0\rangle\,|0\rangle\,|0\rangle\,|\mathrm{g}\rangle$, where $|\phi_0\rangle = p\,|0\rangle + e^{i\theta}\sqrt{1-p^2}\,|1\rangle$, with p randomly chosen between 0 and 1. We define the state transfer fidelity as $F = \mathrm{Tr}\,[\rho_0\rho(t)]$, that is a measure of the overlap of the rightmost cavity state $\rho(t)$ with the leftmost cavity initial state $\rho_0 = |\phi_0\rangle\,\langle\phi_0|$.

The results for different system parameters are shown in Fig. A.1. On one hand, in Fig. A.1a we have chosen a cavity-qubit coupling in the SC regime, $g/\omega = 0.01$, and two values for the cavity-cavity coupling $J/\omega = 0.01, 0.1$. Firstly, when both quantities are in the SC regime, the cavity-qubit interaction sets an upper bound for the maximum of the state transfer fidelity (black line). Secondly, if the cavity-cavity coupling is in the USC regime, $J/\omega = 0.1$, then almost complete state transfer occurs (red line). On the other hand, in Fig. A.1b, we plot the fidelity F for a cavity-qubit coupling in the USC regime, $g/\omega = 0.2$, and $J/\omega = 0.01, 0.1$ for the cavity-cavity coupling. When g is one order of magnitude larger than J (black line), the transfer is completely inhibited. Contrariwise, there is an enhancement in the state transfer when the cavity-cavity coupling is in the USC regime (red line).

A.2 Coherent state

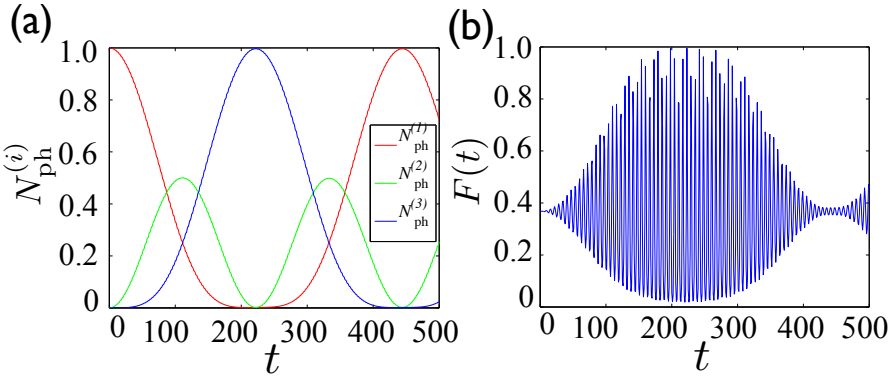

FIGURE A.2: Transfer of a coherent state of amplitude $\alpha = 1$ along a three-cavity array ($g = 0$). (a) Average photon number for the leftmost (blue), central (green) and rightmost (red) cavities. (b) State transfer fidelity over time. In the case of qubit absence, the coherent state is fully transferred. Observe that the fidelity at time zero has a finite value $F \approx 0.38$, which corresponds to the overlap between the vacuum state and the considered coherent state. Time is expressed in units of ω^{-1}.

Let us now focus on the transfer properties of coherent states. We numerically simulated the system dynamics starting from the initial state $|\psi_0\rangle = |\phi_0\rangle\,|0\rangle\,|0\rangle\,|\mathrm{g}\rangle$, where $|\phi_0\rangle = |\alpha\rangle$ is a coherent state of amplitude $|\alpha|$. For the sake of clarity, we first show how a coherent state would transfer along a three-cavity arrays in absence of the qubit interaction. This corresponds to setting $g = 0$ in our model. Such dynamics is shown in Fig. A.2 for a coherent state with $\alpha = 1$. In Fig.A.2a, we show the average photon number for the three cavities, while Fig. A.2b contains the state transfer fidelity. These figures show that the coherent state crosses the central cavity and it is recomposed in the rightmost one. The fast-oscillating behavior of the fidelity is due to relative phase rotation of different coherent state components. We observe also that the fidelity oscillates around a value slightly smaller than $F = 0.4$ due to the finite overlap between the coherent state $|\alpha\rangle$ and the vacuum state $|0\rangle$.

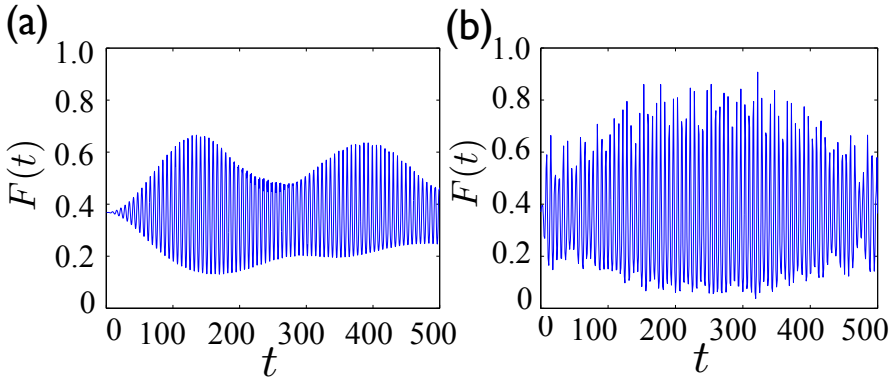

FIGURE A.3: (a) State transfer fidelity over evolution time (in units of ω^{-1}), for a coherent state of amplitude $\alpha = 1$. The system parameters are given by $g = 0.02$ and $J = 0.01$ (SC regime). (b) State transfer fidelity over evolution time, for a coherent state of amplitude $\alpha = 1$. The system parameters are given by $g = 0.2$ and $J = 0.1$ (USC regime). The maximum value that the fidelity can reach is not directly bounded by the cavity-qubit interaction.

Consider now our full model, composed of three cavities and a qubit interacting with the central one. The transfer of coherent states follows the same general rules reported for the case of the linear superposition state, even if the time-dependent fidelity has a fast-oscillating behavior. In the SC regime, the cavity-qubit interaction limits the maximum value that the fidelity can reach. Figure A.3a shows the time evolution of the state transfer fidelity in the case in which $J = 0.01$ and $g = 0.01$, where complete transfer is not allowed. In contrast, in the USC regime, high values of the fidelity can be reached also when g is larger than J. Figure A.3b shows the coherent state transfer dynamics, for a case in which both the cavity-cavity and the cavity-qubit interactions are in the USC regime. The plot shows the fidelity F over evolution time for a coherent state of amplitude $|\alpha| = 1$. In this case, the fidelity can reach $F = 0.9$, also if $g = 2J$.

The cases considered in this Appendix, linear superpositions and coherent states, display the main features of state transfer when considering the physics beyond RWA.

Appendix B

Quantization of the circuit Hamiltonian

In this appendix, we detail the derivation of the quantum model of the circuit design presented in Chapter 3, and we briefly discuss possible future development of our work. In section B.1, we derive the full quantum Hamiltonian that describes the bipartite configuration. In section B.2, we show how to extend the model to the multipartite case.

B.1 Quantum model

In this section, we derive the quantum model of the circuit design proposed in Fig. 3.2, Chapter 3. We restrict to consider the bare resonators, an effective interaction with resonant qubits can be added at the end of the derivation. Let us consider a circuit composed of two transmission line resonators (TLS), connected to the ground through the same superconducting quantum interference device (SQUID), as shown in figure B.1. A SQUID is a superconducting loop interrupted by two Josephson junctions (JJ). Here we take the two JJs that constitute the SQUID to be identical: under this assumption, the SQUID effectively behaves as a single JJ [234], namely, as a non-linear tunable inductance shunted by a small capacitance. We also assume that the JJs are such that their Josephson energy is much bigger than their charge energy $E_J \gg E_C$. In order to write the system classical Lagrangian, we will use a discrete description of the TLSs: each resonator will be represented by an infinite series of LC oscillators of infinitesimal

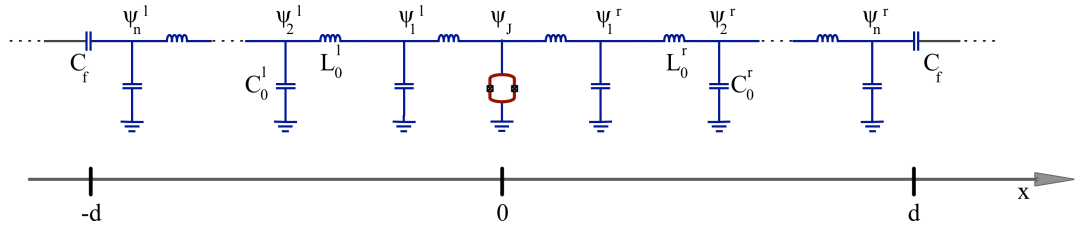

FIGURE B.1: **Sketch of the system.** Two transmission line resonators are connected to the same edge of a grounded SQUID. The SQUID low impedance imposes a voltage node at $x = 0$. Each resonator is coupled with an external line (not considered here) needed for reading the cavity.

length Δx. The system Lagrangian can be then written as

$$\mathcal{L} = \frac{1}{2}\sum_i \left\{ \Delta x C_0^l \left(\dot{\psi}_i^l\right)^2 + \frac{1}{\Delta x L_0^l}\left(\psi_{i+1}^l - \psi_i^l\right)^2 \right\} \tag{B.1}$$

$$+ \frac{1}{2}\sum_i \left\{ \Delta x C_0^r \left(\dot{\psi}_i^r\right)^2 + \frac{1}{\Delta x L_0^r}\left(\psi_{i+1}^r - \psi_i^r\right)^2 \right\} \tag{B.2}$$

$$+ \frac{1}{2} C_J \left(\dot{\psi}_J\right)^2 - \frac{E_J\left(\phi_{\text{ext}}\right)}{2\varphi_0^2}\psi_J^2. \tag{B.3}$$

We defined the magnetic flux $\psi_i^{l/r}$ in the i-th inductor of the left/right resonator as the time integral of the instantaneous voltage v_i across the element: $\psi_i^{l/r}(t) = \int_0^t v_i(\tau)d\tau$. The capacitance and inductance per unit of length are denoted by $C_0^{l/r}$ and $L_0^{l/r}$, respectively. Variables and constants with the subscript J refer to the SQUID; notice that C_J and L_J represent the total capacitance and inductance of the SQUID, which will be described by means of a lumped-element model also in the continuum limit ($\Delta x \to 0$). We defined the reduced magnetic flux as $\varphi_0 = \phi_0/2\pi$, where ϕ_0 is the magnetic flux quantum. The inductance of the SQUID depends on the external flux ϕ_{ext} threading the device: $L_J = \frac{\varphi_0^2}{E_J(\phi_{\text{ext}})}$, where $E_J(\phi_{\text{ext}}) = 2E_J\left|\cos\left(\frac{\phi_{\text{ext}}}{2\varphi_0}\right)\right|$. The Josephson energy E_J and the critical current I_c are directly related $E_J = I_c\varphi_0$.

B.1.1 Spatial modes

In the bulk of each resonator the equation of motion is given by (for the sake of simplicity we omit the superscript l/r)

$$C_0\ddot{\psi}_i(t) = \frac{1}{\Delta x}\left\{ \frac{\psi_{i+1}(t) - \psi_i(t)}{\Delta x L_0} - \frac{\psi_i(t) - \psi_{i-1}(t)}{\Delta x L_0} \right\} \tag{B.4}$$

which, in the continuum limit $\Delta x \to 0$, reduces to

$$\ddot{\psi}(x,t) = v\,\frac{\partial^2}{\partial x^2}\psi(x,t)\bigg|_{x=0} \qquad \text{where} \qquad v = \frac{1}{\sqrt{C_0 L_0}}. \tag{B.5}$$

The differential equation (B.5) can be solved using the usual variable separation ansatz $\psi(x,t) = f(x)\phi(t)$, with $f(x) = \alpha\cos(kx) + \beta\sin(kx)$, $\phi(t) = ae^{-i\omega t} + be^{i\omega t}$, and $\omega = k/\sqrt{L_0 C_0}$. The electrical boundary conditions at the far left and far right extremities are established by the capacitances C_f, which mediate the coupling with external transmission lines. This capacitive coupling can be made very small and its contribution to the resonator modes is negligible. Following a standard procedure, we will use open boundary conditions in order to evaluate the resonator modes, the interaction with the environment can be then described by means of a small effective coupling.

$$\frac{\partial\psi^l(x)}{\partial x}\bigg|_{x=-d} = 0 \qquad \text{and} \qquad \frac{\partial\psi^r(x)}{\partial x}\bigg|_{x=d} = 0. \tag{B.6}$$

The equation of motion for the dynamical variable ψ_J corresponds to the Kirchhoff law of current conservation at the central node ($x = 0$)

$$C_J\ddot{\psi}^2(0,t) + \frac{E_J(\phi_{\text{ext}})}{\varphi_0^2}\psi(0,t) = \frac{1}{L_0^l}\,\frac{\partial\psi^l(x)}{\partial x}\bigg|_{x=o} + \frac{1}{L_0^r}\,\frac{\partial\psi^r(x)}{\partial x}\bigg|_{x=0}. \tag{B.7}$$

Now, given that the resonator inductances are much bigger than the SQUID inductance $L_J = \varphi_0^2/E_J(\phi_{\text{ext}})$, the terms on the right side of equation (B.7) are very small compared to the inductive contribution of the SQUID. This mathematical statement has the following physical interpretation: the SQUID is a low-impedance element, therefore most of the current coming either from the left or from the right will flow through the SQUID directly to the ground, without crossing the other resonator. In other words, the presence of one resonator does not perceptibly modify the mode structure of the other one, although a small inductive coupling between them can be introduced from equation (B.7). This allows us to define separated modes for the two resonators, which are constrained to satisfy the boundary condition

$$(k\ d)\tan(k\ d) = \frac{C_J}{C}(k\ d)^2 - \frac{L}{L_J}. \tag{B.8}$$

This equation holds for both resonators, we omitted the superscripts l/r and we defined the total capacitance $C = C_0\ d$ and total inductance $L = L_0\ d$. Notice that modifying the external flux ϕ_{ext} results in a variation of the SQUID effective inductance L_J, and so in a modification of the boundary condition (B.8). Finally, the resonator frequencies can be found solving the differential equations (B.5), being the boundary conditions given by (B.6) and by the solution [156] of the transcendental equation (B.8).

For didactical purpose, we observe that a good approximation to the resonator

modes can be found assuming that at $x = 0$ there is a voltage node, namely $\psi(0,t) = 0$. Under this assumption, the system is composed of two independent $\lambda/4$ resonators

$$f(x) = \sqrt{2}\sum_n \sin\left(k_n\ x\right) \qquad \text{where} \quad k_n = \frac{\pi}{d}\left(\frac{1}{2} + n\right). \tag{B.9}$$

B.1.2 Hamiltonian

Now, we write the system Lagrangian exploiting the stationary spatial solutions found in section B.1.1. Integrating equations (B.1) and (B.2) over the spatial degree of freedom, in the continuum limit, we obtain the Lagrangian of the free resonators

$$\mathcal{L}_0 = \sum_{\nu=l,r}\sum_n \left\{ \frac{C^\nu}{2}\left[\dot{\phi}_n^\nu(t)\right]^2 - \frac{1}{L^\nu}\left[\phi_n^\nu(t)\right]^2 \right\}, \tag{B.10}$$

where the index ν identifies resonator, while n runs over the spatial eigenmodes (and so, over the frequencies). We are interested in the dynamics of two level quantum systems that are embedded in the resonators. These qubits effectively interact only with one mode of each cavity, hence, hereafter we will restrict to consider one mode per resonator. This treatment is valid under the condition that the oscillation of the boundary conditions do not make resonant interaction terms between the relevant mode and the other ones.

The effective interaction between the modes ϕ^l and ϕ^r can be found isolating the variable $\phi(0,t)$ in equation (B.7) and replacing it in the SQUID contribution to the system Lagrangian (equation (B.3))

$$\mathcal{L}_{int} = -\frac{\varphi_0^2}{E_J\left(\phi_{\text{ext}}\right)}\left\{ \frac{1}{L_0^l}k^l\phi^l(t) + \frac{1}{L_0^r}k^r\phi^r(t) \right\}^2. \tag{B.11}$$

Now we assume that the prefactor of the previous equation is oscillating with a frequency such that only the cross-interaction term will be relevant in the Hamiltonian dynamics. This regime is accessible when the resonators are off resonance and the difference between their frequencies is much bigger than the coupling strength. We will show that the considered regime of parameters allows such approximation. Defining the conjugate momentum $q^{l/r} = \partial\mathcal{L}_{tot}/\partial\dot{\phi}^{l/r}$, we find the system Hamiltonian

$$\mathcal{H} = \sum_{\nu=l,r}\left\{ \frac{1}{2C_\nu}q_\nu^2(t) + \frac{\omega_\nu^2 C_\nu}{2}\phi_\nu^2(t) \right\} - \frac{2\varphi_0^2}{E_J\left(\phi_{\text{ext}}\right)}\frac{\omega_l\omega_r}{Z_l Z_r}\phi_l\phi_r, \tag{B.12}$$

where we defined the impedance as $Z_\nu = \sqrt{L_\nu/C_\nu}$. Now, we perform the usual quantization process and define ladder operators

$$[\phi_\nu, q_\nu] = i\hbar \qquad , \qquad \phi_\nu = \sqrt{\frac{\hbar}{2\omega_\nu C_\nu}}\left(a_\nu^\dagger + a_\nu\right) \qquad , \qquad q_\nu = i\sqrt{\frac{\hbar C_\nu \omega_\nu}{2}}\left(a_\nu^\dagger - a_\nu\right). \tag{B.13}$$

Finally, we can write the system quantum Hamiltonian as

$$\mathcal{H}/\hbar = \omega_l a_l^\dagger a_l + \omega_r a_r^\dagger a_r - \frac{\varphi_0^2}{E_J\left(\phi_{\text{ext}}\right)}\sqrt{\frac{\omega_l\omega_r}{C_l C_r}}\frac{1}{Z_l Z_r}\left(a_l^\dagger + a_l\right)\left(a_r^\dagger + a_r\right). \tag{B.14}$$

B.1.3 Two-mode squeezing

Observe that, as stated in Chapter 3, when the driving frequency is comparable to the SQUID plasma frequency, the device can not be considered as a passive element and a more complex behaviour emerges. The SQUID plasma frequency is defined as $\omega_p 2 = \sqrt{1/C_J L_J}$, so ω_p becomes smaller as the external flux get closer to $\phi_{\text{ext}}/2\varphi_0 = \pi/2$. To overcome this problem, we consider an external flux which is oscillating with small variation Δ around a fixed offset $\bar{\phi}$. In this way, with the physical parameters we considered, the SQUID plasma frequency is much bigger than ω_d for every value of $\phi_{\text{ext}}(t)$ during the time evolution. Such condition allows us to expand the coupling parameter in the interaction term of equation (B.14)

$$\frac{\phi_{\text{ext}}}{2\varphi_0} = \bar{\phi} + \Delta\cos\left(\omega_d t\right) \qquad \Longrightarrow \qquad \frac{1}{E_J\left(\phi_{\text{ext}}\right)} \approx \frac{1}{\cos\bar{\phi}} + \frac{\sin\bar{\phi}}{\cos^2\bar{\phi}}\ \Delta\ \cos\left(\omega_d t\right). \tag{B.15}$$

Hence, the interaction term of the system Hamiltonian can be written, in the Schrödinger picture, as the sum of a constant and a time-dependent term

$$\mathcal{H}/\hbar = \omega_l a_l^\dagger a_l + \omega_r a_r^\dagger a_r + \eta\left(a_l^\dagger + a_l\right)\left(a_r^\dagger + a_r\right) + \alpha_0\left(e^{i\omega_d t} + e^{-i\omega_d t}\right)\left(a_l^\dagger + a_l\right)\left(a_r^\dagger + a_r\right) \tag{B.16}$$

with

$$\eta = \frac{\varphi_0^2}{2E_J\cos\bar{\phi}}\sqrt{\frac{\omega_l\omega_r}{C_l C_r}}\frac{1}{Z_l Z_r} \qquad \text{and} \qquad \alpha_0 = \frac{\varphi_0^2}{4E_J}\frac{\sin\bar{\phi}}{\cos^2\bar{\phi}}\sqrt{\frac{\omega_l\omega_r}{C_l C_r}}\frac{1}{Z_l Z_r}\Delta. \tag{B.17}$$

When the detuning between the resonators is large compared to the coupling parameters $\eta, \alpha_0 \ll |\omega_l - \omega_r|$, we can perform the rotating wave approximation and neglect all terms that are fast-oscillating in the interaction picture. If we choose the external driving to match the sum of the resonators frequencies $\omega_d = \omega_l + \omega_r$, the interaction Hamiltonian will reduce to a two-mode squeezing term

$$\mathcal{H}/\hbar = \omega_l a_l^\dagger a_l + \omega_r a_r^\dagger a_r + \alpha_0\left(e^{-i\omega_d t}a_l^\dagger a_r^\dagger + e^{i\omega_d t}a_l a_r\right). \tag{B.18}$$

B.2 Multipartite case

Consider a circuit scheme such that n resonators are connected to the ground through the same SQUID, as shown in figure 3.4a for $n = 4$. Equation (B.5) still holds in the bulk of each resonator, and the boundary conditions (B.6) are still valid. On the other hand, the Kirchhoff's law of current conservation (B.7) must be extended to include the contribution of every branch of the circuit

$$C_J \ddot{\psi}^2(0,t) + \frac{E_J\left(\phi_{\text{ext}}\right)}{\varphi_0^2}\psi(0,t) = \sum_\nu \frac{1}{L_0^\nu}\left.\frac{\partial \psi^\nu(x)}{\partial x}\right|_{x=o}. \tag{B.19}$$

As far as the resonator inductances are much larger than the SQUID inductance, we can still treat the system as composed of independent resonators, interacting through a small current-current coupling. In this case, resonator spatial eigenmodes can be found following the same procedure we used in the bipartite case. Neglecting a small capacitive contribution, the term in the Lagrangian which describes the current-current coupling can be written as

$$\mathcal{L}_{int} = -\frac{\varphi_0^2}{E_J\left(\phi_{\text{ext}}\right)}\left\{\sum_\nu \frac{1}{L_0^\nu} k^\nu \phi^l(t)\right\}^2. \tag{B.20}$$

In a quantum description of such system, these interactions result in single-mode drivings and two-mode interactions between the field quadratures

$$\mathcal{H}_I = \sum_\nu \alpha_\nu(t)\left(a_\nu^\dagger + a_\nu\right)^2 + \sum_{\nu,\mu}\beta_{\nu\mu}(t)\left(a_\nu^\dagger + a_\nu\right)\left(a_\mu^\dagger + a_\mu\right), \tag{B.21}$$

where the parameters $\alpha_\nu(t)$ and $\beta_{\nu\mu}(t)$ depend on the external flux $\phi_{\text{ext}}(t)$ threading the SQUID, and they are all small compared to the resonator characteristic frequencies. The time-dependence of $\phi_{\text{ext}}(t)$ establishes which terms of equation (B.21) will have a non-negligible contribution to the system dynamics. When the external flux is given by the sum of signals oscillating at different frequencies, with small variations Δ_i, around a constant off-set $\bar{\phi}$

$$\frac{\phi_{\text{ext}}}{2\varphi_0} = \bar{\phi} + \Delta_1 \cos\left(\omega_{D1} t\right) + \Delta_2 \cos\left(\omega_{D2} t\right) + \ldots, \tag{B.22}$$

with $\Delta_i \ll \bar{\phi}$, we can generalize the method used in equation (B.22)

$$\frac{1}{E_J\left(\phi_{\text{ext}}\right)} \approx \frac{1}{\cos\bar{\phi}} + \frac{\sin\bar{\phi}}{\cos^2\bar{\phi}}\,\Delta_1\,\cos\left(\omega_{D1}t\right) + \frac{\sin\bar{\phi}}{\cos^2\bar{\phi}}\,\Delta_2\,\cos\left(\omega_{D2}t\right) + \ldots \tag{B.23}$$

Hence, controlling the external flux allows to turn on and off single- and two-mode squeezing terms, as well as linear couplings between the resonators.

Appendix C

Further details on state engineering

In this appendix, we gather further details on the protocol introduced in Chapter 4. In Section C.1, we show how the creation and annihilation operators act on Rabi model eigenstates. In Section C.2, we provide a detailed derivation of the effective Hamiltonian used to modelize state transfer. In Section C.3, we estimate the time needed to perform a full tomography with the present protocol, in a realistic implementation. Finally, in Section C.4, we show how parity-forbidden transition can be implemented with a two-step process.

C.1 Some properties of the Quantum Rabi model

We will not provide here a detailed description of the properties of the quantum Rabi model (QRM) eigenstates (instead we refer to [19]). The main feature we will focus on is the parity conservation of the QRM Hamiltonian. Let us define the parity operator $\Pi = -\sigma_z e^{i\pi a^\dagger a}$, which corresponds to the parity of the number of excitations in the composite system. Once the parity operator is defined, it is straightforward to show that it commutes with the QRM Hamiltonian. This ensures that any eigenstate of the quantum Rabi model is also an eigenstate of the parity operator.

Let us now consider the action of the creation operator on an arbitrary eigenstate $|\psi_n\rangle$. From its very definition, the creation operator creates one excitation inside the cavity, thus bringing $|\psi_n\rangle$ to a vector of opposite parity. In other words, $a^\dagger |\psi_n\rangle$ belongs to a subspace orthogonal to the one in which lies $|\psi_n\rangle$. Eventually we have shown the

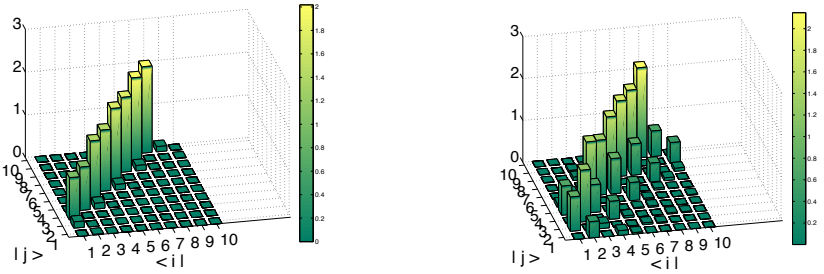

FIGURE C.1: Absolute values of the elements of the transition matrix $k_{ij} = \langle\psi_i| a |\psi_j\rangle$. The left box corresponds to the strong coupling regime ($g/\omega_r = 0.03$), while the right box corresponds to the USC regime ($g/\omega_r = 0.6$), i.e. the quantum Rabi model. The diagonal term vanish, as shown in Section C.1. Notice that, in the SC regime, where the Jaynes-Cummings model applies, the coefficients k_{ij} vanish for $\omega_i > \omega_j$.

following relation:

$$\langle\psi_j| a^\dagger |\psi_n\rangle = 0 \tag{C.1}$$

for any j such that the parity of $|\psi_j\rangle$ is the same as $|\psi_n\rangle$, as shown in Fig.C.1. This demonstration naturally extends to the annihilation operator a. As a corollary, we have:

$$\langle\psi_n| a^{(\dagger)} |\psi_n\rangle = 0 \tag{C.2}$$

We show in chapter 4 text that apart from avoided crossings, the full model eigenstates are in product states made of eigenstates of the QRM and the ancilla being in the ground or excited state. Eq. (C.2) proves that the only contribution from the ancilla to the eigenenergies comes from the free Hamiltonian $(\omega_a/2)\sigma_z^a$. This explains the behavior of the eigenenergies as a function of ω_a: fully degenerate at $\omega_a = 0$, then increasing linearly.

C.2 Derivation of the effective interaction Hamiltonian

We consider the system as being composed of the the QRM interacting via the resonator field with the ancillary qubit. This means the total Hamiltonian reads:

$$\mathcal{H} = \sum_n \omega_n |\psi_n\rangle \langle\psi_n| + \frac{\omega_a}{2}\sigma_z^a + \mathcal{H}_I$$
$$\mathcal{H}_I = g_a \sigma_x^a (a + a^\dagger) \tag{C.3}$$

where we denoted with $|\psi_n\rangle$ the eigenstates, of increasing energy ω_n, of the QRM. Using the completeness relation $\mathcal{I} = \sum_n |\psi_n\rangle \langle\psi_n|$, the interaction Hamiltonian becomes:

$$\mathcal{H}_I = g_a \sigma_x^a \sum_{i,j} k_{ij} |\psi_i\rangle \langle\psi_j| + k_{ji}^* |\psi_i\rangle \langle\psi_j| \tag{C.4}$$

where $k_{ij} = \langle\psi_i| a |\psi_j\rangle$. In the previous Section we recalled that for any i we have $\langle\psi_i| a + a^\dagger |\psi_i\rangle = 0$. Thus we can order the double sum in equation Eq. (C.4) to get:

$$\mathcal{H}_I = g_a \sigma_x^a \sum_{i>j} (k_{ij} + k_{ji}^*) |\psi_i\rangle \langle\psi_j| + (k_{ji} + k_{ij}^*) |\psi_j\rangle \langle\psi_i| \tag{C.5}$$

Since the $|\psi_n\rangle$'s are labeled in increasing energy, we can interpret the two operators in the sum the following way: one raising the energy of the polariton, $|\psi_i\rangle \langle\psi_j|$, the other one lowering the energy $|\psi_j\rangle \langle\psi_i|$. Now we will assume that the spectrum of the QRM is non-linear enough so that we are able to isolate one particular transition frequency $\omega_{ij} = \omega_i - \omega_j > 0$. This anharmonic assumption is valid in the regime of $g/\omega_r \lesssim 2$, which is the one we consider here. Thus we can perform a new Rotating Wave Approximation (RWA) when bringing the frequency of the ancilla close to resonance with ω_{ij}. More precisely, we move $\mathcal{H}_I$ to the interaction picture:

$$\tilde{\mathcal{H}}_I(t) = g_a(\sigma_+^a e^{i\omega_a t} + \sigma_-^a e^{-i\omega_a t})((k_{ij} + k_{ji}^*) |\psi_i\rangle \langle\psi_j| e^{i\omega_{ij} t} + (k_{ji} + k_{ij}^*) |\psi_j\rangle \langle\psi_i| e^{-i\omega_{ij} t}) \tag{C.6}$$

In this expression we identify two oscillating frequencies: $\omega_a + \omega_{ij}$ and $\omega_a - \omega_{ij} \equiv \delta$. In this context we will perform the standard RWA, neglecting the quickly oscillating terms. The interaction picture Hamiltonian reads:

$$\tilde{\mathcal{H}}_I(t) = g_a((k_{ij} + k_{ji}^*)\sigma_-^a |\psi_i\rangle \langle\psi_j| e^{-i\delta t} + (k_{ji} + k_{ij}^*)\sigma_+^a |\psi_j\rangle \langle\psi_i| e^{i\delta t}) \tag{C.7}$$

thus yielding a Jaynes-Cummings-like interaction Hamiltonian.

C.3 Estimation of the time required to perform the spectroscopy protocol

Our protocol allows for analyzing the spectrum of the polariton, based on measurements performed on the ancillary qubit. This means the relevant parameters for this protocol are well-known and the manipulations are now standard [174]. In this Section we will provide a rough estimation of the time required to detect the peaks in Fig. 4.4 of chapter 4.

The right order of magnitude for the experimental ω_2 spacing is given by the full width at half maximum (FWHM) of those peaks. In our case, the FWHM is of the order of $0.1\omega_r$. Besides, we span with ω_r an interval of approximate length $2\omega_r$. Considering 5 points per peak, we obtain an upper bound on the number of points we want to measure of 100. This value could be further reduced performing a more clever analysis of the spectrum.

Every point actually corresponds to computing the visibility of Rabi oscillations at a given ancilla frequency. This can be done by measuring the ancilla until half a period, in other words by monitoring the ancilla for a time $T_{\text{half}} \approx 50/\omega_r$ (see Fig. 4c in chapter 4). This monitoring requires to measure σ_z^a roughly 50 times, every measurement being of a duration at most T_{half}. For a standard cavity in circuit QED, we have $\omega_r \approx 2\pi \times 5$ GHz, which gives approximately 100 ns to recover the visibility at a given frequency ω_2.

Going from one point to another means tuning the ancillary qubit frequency. This can be done in a few nanoseconds [174], hence it is negligible compared to the computation of a single point. In the end, summing 100 ns for 100 values of ω_2, the whole spectroscopy duration is of the order of 10 microseconds.

C.4 Multi-step process for state engineering and tomography

In Chapter 4, we show how selective state-transfer processes allow to prepare and manipulate the USC system in a given state, and to perform quantum state tomography. In the theoretical framework that we introduced, selective state transfer which involves USC system states of different parity are straightforward, as the ancilla spin-flip grants parity conservation. The goal of this Section is to show how one may address transitions that should be forbidden because of parity conservation, by means of a feasible two-step protocol. Let $|\psi_a\rangle$ and $|\psi_b\rangle$ two eigenstates of the QRM of same parity. We want to distinguish the pure states made of an arbitrary superposition of $|\psi_a\rangle$ and $|\psi_b\rangle$ from the statistical mixture with same weights. To this end, we will make use of an auxiliary eigenstate of the QRM with opposite parity $|\phi\rangle$. In the following we will consider two different cases: first when the energy of $|\phi\rangle$ lies in between the energies of $|\psi_a\rangle$ and $|\psi_b\rangle$, then when it does not.

C.4.1 Forbidden transition with an auxiliary one in between

We suppose here the following ordering of the Rabi eigenstates energies. Namely: $E_{|\psi_a\rangle} < E_{|\phi\rangle} < E_{|\psi_b\rangle}$. We will consider that only those three levels are populated, assuming that we are able to initialize the ancilla in the $|+\rangle \equiv (|e\rangle + |g\rangle)/\sqrt{2}$ state. The initial state reads:

$$|\phi_i\rangle = (\alpha\,|\psi_a\rangle + \beta\,|\psi_b\rangle + \gamma\,|\phi\rangle)\,|+\rangle \tag{C.8}$$

First we perform half a Rabi oscillation between $|\psi_a\rangle$ and $|\phi\rangle$. This transforms the global state as follows:

$$|\phi_1\rangle = \alpha\frac{|\psi_a\rangle\,|g\rangle + |\phi\rangle\,|g\rangle}{\sqrt{2}} + \beta\,|\psi_b\rangle\,|+\rangle + \gamma\frac{|\psi_a\rangle\,|e\rangle + |\phi\rangle\,|e\rangle}{\sqrt{2}} \tag{C.9}$$

Then we repeat the protocol for the transition between $|\phi\rangle$ and $|\psi_b\rangle$. Thus we have:

$$|\phi_2\rangle = \alpha\frac{|\psi_a\rangle\,|g\rangle + |\phi\rangle\,|g\rangle}{\sqrt{2}} + \beta\frac{|\phi\rangle\,|e\rangle + |\psi_b\rangle\,|e\rangle}{\sqrt{2}} + \gamma\frac{|\psi_a\rangle\,|e\rangle + |\psi_b\rangle\,|g\rangle}{\sqrt{2}} \tag{C.10}$$

which we can write in a more convenient way:

$$|\phi_2\rangle = \frac{1}{\sqrt{2}}(|\phi_a\rangle\,|g\rangle + |\phi_b\rangle\,|e\rangle) \tag{C.11}$$

where $|\phi_a\rangle$ and $|\phi_b\rangle$ are two non-orthogonal states. Eventually, the reduced density matrix of the ancillary qubit reads:

$$\rho_a = \begin{pmatrix} |\alpha|^2 + \frac{1}{2}|\gamma|^2 & \frac{1}{2}(\alpha\beta^* + \alpha\gamma^* + \gamma\beta^*) \\ \frac{1}{2}(\alpha^*\beta + \alpha^*\gamma + \gamma^*\beta) & |\beta|^2 + \frac{1}{2}|\gamma|^2 \end{pmatrix} \tag{C.12}$$

Finally, assuming that we can infer the coherences between $|\psi_a\rangle$ and $|\phi\rangle$ and between $|\psi_b\rangle$ and $|\phi\rangle$ separately, this protocol allows for measuring the coherence terms relative to a forbidden transition – which correspond to the product $\alpha\beta^*$.

C.4.2 Forbidden transition between two consecutive eigenstates

In the case where the forbidden transition involves two consecutive eigenstates the result is a bit different. The energies correspond to $E_{|\psi_a\rangle} < E_{|\psi_b\rangle} < E_{|\phi\rangle}$. The initial state is again

$$|\phi_i\rangle = (\alpha\,|\psi_a\rangle + \beta\,|\psi_b\rangle + \gamma\,|\phi\rangle)\,|+\rangle \tag{C.13}$$

The first excitation transfer, associated with the transition between $|\psi_a\rangle$ and $|\phi\rangle$ yields:

$$|\varphi_1\rangle = \alpha\frac{|\psi_a\rangle\,|g\rangle + |\phi\rangle\,|g\rangle}{\sqrt{2}} + \beta\,|\psi_b\rangle\,|+\rangle + \gamma\frac{|\psi_a\rangle\,|e\rangle + |\phi\rangle\,|e\rangle}{\sqrt{2}} \tag{C.14}$$

Then when it comes to the transition between $|\psi_b\rangle$ and $|\phi\rangle$ the global state becomes:

$$|\varphi_2\rangle = \alpha\frac{|\psi_a\rangle|g\rangle + |\psi_b\rangle|e\rangle}{\sqrt{2}} + \beta\frac{|\phi\rangle|e\rangle + |\psi_b\rangle|e\rangle}{\sqrt{2}} + \gamma\frac{|\psi_a\rangle|e\rangle + |\phi\rangle|e\rangle}{\sqrt{2}} \tag{C.15}$$

which we can once again write, defining two non-orthogonal states $|\varphi_a\rangle$ and $|\varphi_a\rangle$ different than before:

$$|\varphi_2\rangle = \frac{1}{\sqrt{2}}(|\varphi_a\rangle|g\rangle + |\varphi_b\rangle|e\rangle) \tag{C.16}$$

and for the reduced density matrix of the ancilla:

$$\rho_a = \begin{pmatrix} |\beta|^2 + \frac{1}{2}|\alpha|^2 & \frac{1}{2}(\alpha\gamma^* + \beta\alpha^* + \beta\gamma^*) \\ \frac{1}{2}(\alpha^*\gamma + \beta^*\alpha + \beta^*\gamma) & |\gamma|^2 + \frac{1}{2}|\alpha|^2 \end{pmatrix} \tag{C.17}$$

Once again, one may access the coherence terms relative to the forbidden transition.

Appendix D

Two-photon Rabi: mathematical properties and parity measurement

D.1 Properties of the wavefunctions below and above the collapse point

The presence of the collapse point at $g = \omega/2$ can be inferred rigorously by studying the asymptotic behavior of the formal solutions to the time-independent Schrödinger equation $\mathcal{H}\psi = E\psi$. We consider now the simplest case $N = 1$. Using the representation of the model in the Bargmann space $\mathcal{B}$ of analytic functions [235], the Schrödinger equation for $\psi(z)$ in the invariant subspace with parity eigenvalue $\Pi = +1$ reads

$$g\psi''(z) + \omega z\psi'(z) + gz^2\psi(z) + \frac{\omega_q}{2}\psi(iz) = E\psi(z), \tag{D.1}$$

where the prime denotes differentiation with respect to the complex variable z. This nonlocal linear differential equation of the second order, connecting the values of ψ at the points z and iz, may be transformed to a local equation of the fourth order,

$$\psi^{(4)}(z)+[(2-\bar{\omega}^2)z^2+2\bar{\omega}]\psi''(z)+[4+2\bar{\omega}\bar{E}-\bar{\omega}^2]z\psi'(z)+[z^4-2\bar{\omega}z^2+2-\bar{E}^2+\Delta^2]\psi(z)=0, \tag{D.2}$$

where we have used the abbreviations $\bar{\omega} = \omega/g$, $\Delta = \omega_q/(2g)$, $\bar{E} = E/g$. Equation (D.2) has no singular points in the complex plane except at $z = \infty$, where it exhibits an unramified irregular singular point of s-rank three [236]. That means that the so-called

normal solutions have the asymptotic expansion

$$\psi(z) = e^{\frac{\gamma}{2}z^2+\alpha z} z^{\rho}(c_0 + c_1 z^{-1} + c_2 z^{-2} + \ldots) \quad \text{for} \quad z \to \infty. \tag{D.3}$$

Functions of this type are only normalizable (and belong therefore to $\mathcal{B}$) if the complex parameter γ, a characteristic exponent of the second kind, satisfies $|\gamma| < 1$. In our case, the possible γ's are the solutions of the biquadratic equation

$$x^4 + x^2(2 - \bar{\omega}^2) + 1 = 0. \tag{D.4}$$

It follows

$$\gamma_{1,2} = \frac{\bar{\omega}}{2} \pm \sqrt{\frac{\bar{\omega}^2}{4} - 1}, \qquad \gamma_{3,4} = -\frac{\bar{\omega}}{2} \pm \sqrt{\frac{\bar{\omega}^2}{4} - 1}. \tag{D.5}$$

For $\bar{\omega}/2 > 1$, all solutions are real. Whereas $|\gamma_1| = |\gamma_4| > 1$, we have $|\gamma_2| = |\gamma_3| < 1$. In this case, there exist normalizable solutions if γ_2 or γ_3 appears in Eq. (D.3). The condition for absence of the other characteristic exponents $\gamma_{1,4}$ in the formal solution of Eq. (D.2) is the spectral condition determining the parameter E in the eigenvalue problem $\mathcal{H}\psi = E\psi$. It follows that for $g < \omega/2$, a discrete series of normalizable solutions to Eq. (D.1) may be found and the spectrum is therefore a pure point.

On the other hand, for $\bar{\omega}/2 < 1$, all γ_j are located on the unit circle with $\gamma_1 = \gamma_2^*, \gamma_3 = \gamma_4^*$. Because, then, no normalizable solutions of Eq. (D.2) exist, the spectrum of the (probably self-adjoint) operator $\mathcal{H}$ must be continuous for $g > \omega/2$, i.e. above the collapse point. The exponents γ_1 and γ_2 (γ_3 and γ_4) join at 1 (-1) for $g = \omega/2$. The exponent $\gamma = 1$ belongs to the Bargmann representation of plane waves. Indeed, the plane wave states $\phi_q(x) = (2\pi)^{-1/2}\exp(iqx)$ in the rigged extension of $L^2(\mathbb{R})$ [237], satisfying the othogonality relation $\langle\phi_q|\phi_{q'}\rangle = \delta(q - q')$, are mapped by the isomorphism $\mathcal{I}$ between $L^2(\mathbb{R})$ and $\mathcal{B}$ onto the functions

$$\mathcal{I}[\phi_q](z) = \pi^{-1/4} e^{-\frac{1}{2}q^2 + \frac{1}{2}z^2 + i\sqrt{2}qz}, \tag{D.6}$$

they correspond therefore to $\gamma = 1$. It is yet unknown whether at the collapse point $g = \omega/2$, the generalized eigenfunctions of $\mathcal{H}$ have plane wave characteristics for $\omega_q \neq 0$ or which properties of these functions appear above this point, where the spectrum is unbounded from below.

D.2 Measurement of the parity operator

The parity operator, defined as $\Pi = (-1)^N \bigotimes_{n=1}^{N} \sigma_z^n \exp\{i\frac{\pi}{2}n\}$, with $n = a^\dagger a$, is a non-Hermitian operator that can be explicitly written as the sum of its real and imaginary

parts,

$$\Pi = (-1)^N \bigotimes_{n=1}^{N} \sigma_z^n \cos(\frac{\pi}{2} a^\dagger a) + i(-1)^N \bigotimes_{n=1}^{N} \sigma_z^n \sin(\frac{\pi}{2} a^\dagger a). \tag{D.7}$$

For simplicity, we will focus on the $N = 1$ case, but the procedure is straightforwardly extendible to any N. We will show how to measure the expectation value of operators of the form

$$\exp\{\pm in\ \sigma_i\ \phi\}\sigma_j, \tag{D.8}$$

where $\sigma_{i,j}$ are a pair of anti-commuting Pauli matrices, $\{\sigma_i, \sigma_j\} = 0$, and ϕ is a continuous real parameter. One can then reconstruct the real and imaginary parts of the parity operator, as a composition of observables in Eq. (D.8) for different signs and values of i, j,

$$\Re(\Pi) = -\frac{1}{2}\{\exp(in\sigma_x\frac{\pi}{2})\sigma_z + \exp(-in\sigma_x\frac{\pi}{2})\sigma_z\} \tag{D.9}$$

$$\Im(\Pi) = \frac{1}{2}\{\exp(in\sigma_x\frac{\pi}{2})\sigma_y - \exp(-in\sigma_x\frac{\pi}{2})\sigma_y\}. \tag{D.10}$$

The strategy to retrieve the expectation value of observables in Eq. (D.8) will be based on the following property of anti-commuting matrices A and B: $e^A B e^{-A} = e^{2A}B = Be^{-2A}$. Based on this, the expectation value of the observables in Eq. (D.8) can be mapped onto the expectation value of σ_j when the system has previously evolved under Hamiltonian $H = \pm n\sigma_i$ for a time $t = \phi/2$,

$$\langle\psi|\exp\{\pm in\ \sigma_i\ \phi\}\sigma_j|\psi\rangle = \langle\psi(t = \phi/2)|\sigma_j|\psi(t = \phi/2)\rangle, \tag{D.11}$$

where $|\psi(t)\rangle = e^{-in\sigma_i t}|\psi\rangle$. The expectation value of any Pauli matrix is accesible in trapped-ion setups, σ_z by fluorescence techniques and $\sigma_{x,y}$ by simple rotations. The point then is how to generate the dynamics of Hamiltonian $H = \pm n\sigma_i$. For that, we propose to implement a highly detuned simultaneous red and blue sideband interaction,

$$H = \frac{\Omega_0\eta}{2}(a + a^\dagger)\sigma^+ e^{i\delta t}e^{i\varphi} + \text{H.c.}, \tag{D.12}$$

where φ is the phase of the laser with respect to the dipole moment of the ion. This Hamiltonian can be effectively approximated to the second-order Hamiltonian,

$$H_{\text{eff}} = \frac{1}{\delta}\Big(\frac{\Omega_0\eta}{2}\Big)^2(2n + 1)\sigma_z e^{i\varphi}, \tag{D.13}$$

when $\delta \gg \eta\Omega_0/2$. The laser phase will allow us to select the sign of the Hamiltonian. Of course, one would need to be careful and maintain δ in a regime where $\delta \ll \nu$, ν being the trapping frequency, to guarantee that higher-order resonances are not excited. Finally, in order to get rid of the undesired extra term σ_z in Hamiltonian Eq. (D.13),

one needs to implement one more evolution under the Hamiltonian $H = -(1/2)\Omega_0\eta\sigma_z$. This evolution can be generated by means of a highly detuned carrier transition. So far, we have given a protocol to generate the Hamiltonian $H = \pm n\sigma_z$. In order to generate Hamiltonians $H = \pm n\sigma_y$, one would need to modify the evolution with two local qubit rotations,

$$e^{i\pm n\sigma_y t} = e^{i\sigma_x \pi/4} e^{\pm i n\sigma_z t} e^{-i\sigma_x \pi/4}. \tag{D.14}$$

Similarly, for Hamiltonian $H = \pm n\sigma_x$ one would need to perform rotations around σ_y.

Bibliography

[1] M. Planck, Verh. Deut. Phys. Ges **2**, 202 (1900).

[2] A. Einstein, Annalen der Physik **17**, 132 (1905).

[3] A. Einstein, Verh. Dtsch. Phys. Ges **18**, 318 (1916).

[4] P. A. M. Dirac, Proc. R. Soc. Lond. A **114**, 243 (1927).

[5] F. Mandl and G. Shaw, *Quantum field theory* (John Wiley & Sons, 2010).

[6] R. H. Brown and R. Twiss, Journal of Astrophysics and Astronomy **15**, 13 (1994).

[7] M. O. Scully and M. Sargent, Physics Today **25**, 38 (2008).

[8] R. Loudon, *The quantum theory of light* (Oxford university press, 2000).

[9] T. Maiman, Nature **187**, 493 (1960).

[10] R. J. Glauber, Physical Review **130**, 2529 (1963).

[11] R. J. Glauber, Physical Review **131**, 2766 (1963).

[12] S. Haroche, Reviews of Modern Physics **85**, 1083 (2013).

[13] D. J. Wineland, Reviews of Modern Physics **85**, 1103 (2013).

[14] J. P. Dowling and G. J. Milburn, Philosophical Transactions of the Royal Society of London A: Mathematical, Physical and Engineering Sciences **361**, 1655 (2003).

[15] I. I. Rabi, Physical Review **51**, 652 (1937).

[16] G. Rempe, H. Walther, and N. Klein, Physical Review Letters **58**, 353 (1987).

[17] E. T. Jaynes and F. W. Cummings, Proceedings of the IEEE **51**, 89 (1963).

[18] S. Haroche and J. M. Raimond, *Exploring the quantum* (Oxford Univ. Press, 2006).

[19] D. Braak, Physical Review Letters **107**, 100401 (2011).

[20] E. Solano, Physics **4**, 68 (2011).

[21] H. Walther, B. T. Varcoe, B.-G. Englert, and T. Becker, Reports on Progress in Physics **69**, 1325 (2006).

[22] G. Günter, A. A. Anappara, J. Hees, A. Sell, G. Biasiol, L. Sorba, S. De Liberato, C. Ciuti, A. Tredicucci, A. Leitenstorfer, et al., Nature **458**, 178 (2009).

[23] Y. Todorov, A. M. Andrews, R. Colombelli, S. De Liberato, C. Ciuti, P. Klang, G. Strasser, and C. Sirtori, Physical Review Letters **105**, 196402 (2010).

[24] A. A. Anappara, S. De Liberato, A. Tredicucci, C. Ciuti, G. Biasiol, L. Sorba, and F. Beltram, Physical Review B **79**, 201303 (2009).

[25] J. Bourassa, J. M. Gambetta, A. A. Abdumalikov Jr, O. Astafiev, Y. Nakamura, and A. Blais, Physical Review A **80**, 032109 (2009).

[26] T. Niemczyk, F. Deppe, H. Huebl, E. Menzel, F. Hocke, M. Schwarz, J. Garcia-Ripoll, D. Zueco, T. Hümmer, E. Solano, et al., Nature Physics **6**, 772 (2010).

[27] A. Fedorov, A. Feofanov, P. Macha, P. Forn-Díaz, C. Harmans, and J. Mooij, Physical Review Letters **105**, 060503 (2010).

[28] P. Forn-Díaz, J. Lisenfeld, D. Marcos, J. J. García-Ripoll, E. Solano, C. Harmans, and J. Mooij, Physical Review Letters **105**, 237001 (2010).

[29] G. Scalari, C. Maissen, D. Turčinková, D. Hagenmüller, S. De Liberato, C. Ciuti, C. Reichl, D. Schuh, W. Wegscheider, M. Beck, et al., Science **335**, 1323 (2012).

[30] C. Maissen, G. Scalari, F. Valmorra, M. Beck, J. Faist, S. Cibella, R. Leoni, C. Reichl, C. Charpentier, and W. Wegscheider, Physical Review B **90**, 205309 (2014).

[31] M. V. Gustafsson, T. Aref, A. F. Kockum, M. K. Ekström, G. Johansson, and P. Delsing, Science **346**, 207 (2014).

[32] C. Emary and T. Brandes, Physical Review A **69**, 053804 (2004).

[33] C. P. Meaney, T. Duty, R. H. McKenzie, and G. Milburn, Physical Review A **81**, 043805 (2010).

[34] S. De Liberato, Physical Review Letters **112**, 016401 (2014).

[35] F. Beaudoin, J. M. Gambetta, and A. Blais, Physical Review A **84**, 043832 (2011).

[36] H.-P. Breuer and F. Petruccione, *The theory of open quantum systems* (Oxford university press, 2002).

[37] C. Ciuti, G. Bastard, and I. Carusotto, Physical Review B **72**, 115303 (2005).

[38] S. De Liberato, D. Gerace, I. Carusotto, and C. Ciuti, Physical Review A **80**, 053810 (2009).

[39] S. Ashhab and F. Nori, Physical Review A **81**, 042311 (2010).

[40] A. Ridolfo, M. Leib, S. Savasta, and M. J. Hartmann, Physical Review Letters **109**, 193602 (2012).

[41] C. Ciuti and I. Carusotto, Physical Review A **74**, 033811 (2006).

[42] J. Casanova, G. Romero, I. Lizuain, J. J. García-Ripoll, and E. Solano, Physical Review Letters **105**, 263603 (2010).

[43] P. Nataf and C. Ciuti, Physical Review Letters **107**, 190402 (2011).

[44] T. Kyaw, S. Felicetti, G. Romero, E. Solano, and L.-C. Kwek, Scientific Reports **5** (2015).

[45] G. Romero, D. Ballester, Y. Wang, V. Scarani, and E. Solano, Physical Review Letters **108**, 120501 (2012).

[46] M. Tinkham, *Introduction to superconductivity* (Courier Corporation, 2012).

[47] A. Blais, R.-S. Huang, A. Wallraff, S. Girvin, and R. J. Schoelkopf, Physical Review A **69**, 062320 (2004).

[48] I. Chiorescu, P. Bertet, K. Semba, Y. Nakamura, C. Harmans, and J. Mooij, Nature **431**, 159 (2004).

[49] A. Wallraff, D. I. Schuster, A. Blais, L. Frunzio, R.-S. Huang, J. Majer, S. Kumar, S. M. Girvin, and R. J. Schoelkopf, Nature **431**, 162 (2004).

[50] C. Rigetti, J. M. Gambetta, S. Poletto, B. Plourde, J. M. Chow, A. Córcoles, J. A. Smolin, S. T. Merkel, J. Rozen, G. A. Keefe, et al., Physical Review B **86**, 100506 (2012).

[51] V. Bouchiat, D. Vion, P. Joyez, D. Esteve, and M. Devoret, Physica Scripta **1998**, 165 (1998).

[52] Y. Nakamura, Y. A. Pashkin, and J. Tsai, Nature **398**, 786 (1999).

[53] J. Mooij, T. Orlando, L. Levitov, L. Tian, C. H. Van der Wal, and S. Lloyd, Science **285**, 1036 (1999).

[54] J. M. Martinis, S. Nam, J. Aumentado, and C. Urbina, Physical Review Letters **89**, 117901 (2002).

[55] J. Koch, M. Y. Terri, J. Gambetta, A. A. Houck, D. Schuster, J. Majer, A. Blais, M. H. Devoret, S. M. Girvin, and R. J. Schoelkopf, Physical Review A **76**, 042319 (2007).

[56] D. Schuster, A. Houck, J. Schreier, A. Wallraff, J. Gambetta, A. Blais, L. Frunzio, J. Majer, B. Johnson, M. Devoret, et al., Nature **445**, 515 (2007).

[57] A. Lupaşcu, S. Saito, T. Picot, P. De Groot, C. Harmans, and J. Mooij, Nature Physics **3**, 119 (2007).

[58] J. Kelly, R. Barends, A. Fowler, A. Megrant, E. Jeffrey, T. White, D. Sank, J. Mutus, B. Campbell, Y. Chen, et al., Nature **519**, 66 (2015).

[59] R. Barends, L. Lamata, J. Kelly, L. García-Álvarez, A. Fowler, A. Megrant, E. Jeffrey, T. White, D. Sank, J. Mutus, et al., preprint arXiv:1501.07703 (2015).

[60] C. Wilson, G. Johansson, A. Pourkabirian, M. Simoen, J. Johansson, T. Duty, F. Nori, and P. Delsing, Nature **479**, 376 (2011).

[61] I.-C. Hoi, C. Wilson, G. Johansson, T. Palomaki, B. Peropadre, and P. Delsing, Physical Review Letters **107**, 073601 (2011).

[62] A. A. Houck, H. E. Türeci, and J. Koch, Nature Physics **8**, 292 (2012).

[63] N. M. Sundaresan, Y. Liu, D. Sadri, L. J. Szőcs, D. L. Underwood, M. Malekakhlagh, H. E. Türeci, and A. A. Houck, Physical Review X **5**, 021035 (2015).

[64] J. J. Garcia-Ripoll, B. Peropadre, and S. De Liberato, preprint arXiv:1410.7785 (2014).

[65] F. Diedrich, J. Bergquist, W. M. Itano, and D. Wineland, Physical Review Letters **62**, 403 (1989).

[66] y. Leibfried, R. Blatt, C. Monroe, and D. Wineland, Reviews of Modern Physics **75**, 281 (2003).

[67] T. Bastin, J. von Zanthier, and E. Solano, Journal of Physics B: Atomic, Molecular and Optical Physics **39**, 685 (2006).

[68] P. Schindler, D. Nigg, T. Monz, J. T. Barreiro, E. Martinez, S. X. Wang, S. Quint, M. F. Brandl, V. Nebendahl, C. F. Roos, et al., New Journal of Physics **15**, 123012 (2013).

[69] R. Blatt and C. Roos, Nature Physics **8**, 277 (2012).

[70] J. I. Cirac and P. Zoller, Physical Review Letters **74**, 4091 (1995).

[71] K. Mølmer and A. Sørensen, Physical Review Letters **82**, 1835 (1999).

[72] S. Lloyd et al., Science pp. 1073–1077 (1996).

[73] B. Lanyon, C. Hempel, D. Nigg, M. Müller, R. Gerritsma, F. Zähringer, P. Schindler, J. Barreiro, M. Rambach, G. Kirchmair, et al., Science **334**, 57 (2011).

[74] D. F. James, Applied Physics B: Lasers and Optics **66**, 181 (1998).

[75] K. Kim, M.-S. Chang, R. Islam, S. Korenblit, L.-M. Duan, and C. Monroe, Physical Review Letters **103**, 120502 (2009).

[76] J. W. Britton, B. C. Sawyer, A. C. Keith, C.-C. J. Wang, J. K. Freericks, H. Uys, M. J. Biercuk, and J. J. Bollinger, Nature **484**, 489 (2012).

[77] K. Kim, M.-S. Chang, S. Korenblit, R. Islam, E. Edwards, J. Freericks, G.-D. Lin, L.-M. Duan, and C. Monroe, Nature **465**, 590 (2010).

[78] A. Friedenauer, H. Schmitz, J. T. Glueckert, D. Porras, and T. Schätz, Nature Physics **4**, 757 (2008).

[79] R. Islam, E. Edwards, K. Kim, S. Korenblit, C. Noh, H. Carmichael, G.-D. Lin, L.-M. Duan, C.-C. J. Wang, J. Freericks, et al., Nature communications **2**, 377 (2011).

[80] A. Del Campo, G. De Chiara, G. Morigi, M. Plenio, and A. Retzker, Physical Review Letters **105**, 075701 (2010).

[81] L. Lamata, J. León, T. Schätz, and E. Solano, Physical Review Letters **98**, 253005 (2007).

[82] R. Gerritsma, G. Kirchmair, F. Zähringer, E. Solano, R. Blatt, and C. Roos, Nature **463**, 68 (2010).

[83] R. Gerritsma, B. Lanyon, G. Kirchmair, F. Zähringer, C. Hempel, J. Casanova, J. J. García-Ripoll, E. Solano, R. Blatt, and C. F. Roos, Physical Review Letters **106**, 060503 (2011).

[84] M. H. Anderson, J. R. Ensher, M. R. Matthews, C. E. Wieman, and E. A. Cornell, science **269**, 198 (1995).

[85] C. C. Bradley, C. Sackett, J. Tollett, and R. G. Hulet, Physical Review Letters **75**, 1687 (1995).

[86] K. B. Davis, M.-O. Mewes, M. R. Andrews, N. Van Druten, D. Durfee, D. Kurn, and W. Ketterle, Physical Review Letters **75**, 3969 (1995).

[87] B. Demarco and D. S. Jin, science **185**, 1703 (1999).

[88] F. Schreck, L. Khaykovich, K. L. Corwin, G. Ferrari, T. Bourdel, J. Cubizolles, and C. Salomon, Phys. Rev. Lett. **87**, 080403 (2001).

[89] A. G. Truscott, K. E. Strecker, W. I. McAlexander, G. B. Partridge, and R. G. Hulet, Science **291**, 2570 (2001).

[90] M. Andrews, C. Townsend, H.-J. Miesner, D. Durfee, D. Kurn, and W. Ketterle, Science **275**, 637 (1997).

[91] I. Bloch, T. W. Hänsch, and T. Esslinger, Nature **403**, 166 (2000).

[92] M. Matthews, B. Anderson, P. Haljan, D. Hall, C. Wieman, and E. Cornell, Physical Review Letters **83**, 2498 (1999).

[93] E. P. Gross, Il Nuovo Cimento Series 10 **20**, 454 (1961).

[94] L. Pitaevskii, Sov. Phys. JETP **13**, 451 (1961).

[95] L. P. Pitaevskii and S. Stringari, *Bose-Einstein condensation*, 116 (Oxford University Press, 2003).

[96] P. Courteille, R. S. Freeland, D. J. Heinzen, F. A. van Abeelen, and B. J. Verhaar, Phys. Rev. Lett. **81**, 69 (1998).

[97] M. Greiner, O. Mandel, T. Esslinger, T. W. Hänsch, and I. Bloch, nature **415**, 39 (2002).

[98] D. Jaksch, C. Bruder, J. I. Cirac, C. W. Gardiner, and P. Zoller, Physical Review Letters **81**, 3108 (1998).

[99] M. Lewenstein, A. Sanpera, V. Ahufinger, B. Damski, A. Sen, and U. Sen, Advances in Physics **56**, 243 (2007).

[100] A. Recati, P. Fedichev, W. Zwerger, and P. Zoller, Physical Review Letters **90**, 020401 (2003).

[101] A. J. Leggett, S. Chakravarty, A. Dorsey, M. P. Fisher, A. Garg, and W. Zwerger, Reviews of Modern Physics **59**, 1 (1987).

[102] U. Dorner, P. Fedichev, D. Jaksch, M. Lewenstein, and P. Zoller, Physical Review Letters **91**, 073601 (2003).

[103] E. Demler and F. Zhou, Physical Review Letters **88**, 163001 (2002).

[104] K. Aikawa, A. Frisch, M. Mark, S. Baier, R. Grimm, and F. Ferlaino, Phys. Rev. Lett. **112**, 010404 (2014).

[105] B. Lücke, J. Peise, G. Vitagliano, J. Arlt, L. Santos, G. Tóth, and C. Klempt, Physical Review Letters **112**, 155304 (2014).

[106] P. W. Anderson, Physical Review **109**, 1492 (1958).

[107] N. Mott, Reviews of Modern Physics **40**, 677 (1968).

[108] S. F. Edwards and P. W. Anderson, Journal of Physics F: Metal Physics **5**, 965 (1975).

[109] I. Montvay and G. Münster, *Quantum fields on a lattice* (Cambridge University Press, 1997).

[110] T. Salger, C. Grossert, S. Kling, and M. Weitz, Physical Review Letters **107**, 240401 (2011).

[111] H. Walther, B. T. Varcoe, B.-G. Englert, and T. Becker, Reports on Progress in Physics **69**, 1325 (2006).

[112] I. Bloch, Nature Physics **1**, 23 (2005).

[113] M. J. Hartmann, F. G. Brandao, and M. B. Plenio, Nature Physics **2**, 849 (2006).

[114] A. D. Greentree, C. Tahan, J. H. Cole, and L. C. Hollenberg, Nature Physics **2**, 856 (2006).

[115] D. G. Angelakis, M. F. Santos, and S. Bose, Physical Review A **76**, 031805 (2007).

[116] S. Ritter, C. Nölleke, C. Hahn, A. Reiserer, A. Neuzner, M. Uphoff, M. Mücke, E. Figueroa, J. Bochmann, and G. Rempe, Nature **484**, 195 (2012).

[117] P. Longo, P. Schmitteckert, and K. Busch, Journal of Optics A: Pure and Applied Optics **11**, 114009 (2009).

[118] P. Longo, P. Schmitteckert, and K. Busch, Physical Review Letters **104**, 023602 (2010).

[119] L. Zhou, Z. Gong, Y.-x. Liu, C. Sun, F. Nori, et al., Physical Review Letters **101**, 100501 (2008).

[120] Z. Wang, Y. Li, D. Zhou, C. Sun, and P. Zhang, Physical Review A **86**, 023824 (2012).

[121] M. Leib, F. Deppe, A. Marx, R. Gross, and M. Hartmann, New Journal of Physics **14**, 075024 (2012).

[122] D. L. Underwood, W. E. Shanks, J. Koch, and A. A. Houck, Physical Review A **86**, 023837 (2012).

[123] D. Gerace, H. E. Türeci, A. Imamoglu, V. Giovannetti, and R. Fazio, Nature Physics **5**, 281 (2009).

[124] S. Schmidt, D. Gerace, A. Houck, G. Blatter, and H. Türeci, Physical Review B **82**, 100507 (2010).

[125] M. Mariantoni, H. Wang, R. C. Bialczak, M. Lenander, E. Lucero, M. Neeley, A. O'Connell, D. Sank, M. Weides, J. Wenner, et al., Nature Physics **7**, 287 (2011).

[126] A. Sornborger and E. Stewart, Physical Review A **60**, 1956 (1999).

[127] G. De Chiara, D. Rossini, S. Montangero, and R. Fazio, Physical Review A **72**, 012323 (2005).

[128] F. A. Wolf, F. Vallone, G. Romero, M. Kollar, E. Solano, and D. Braak, Physical Review A **87**, 023835 (2013).

[129] E. Solano, G. S. Agarwal, and H. Walther, Physical Review Letters **90**, 027903_1 (2003).

[130] D. Ballester, G. Romero, J. J. García-Ripoll, F. Deppe, and E. Solano, Physical Review X **2**, 021007 (2012).

[131] M. B. Plenio and S. F. Huelga, New Journal of Physics **10**, 113019 (2008).

[132] M. Mohseni, P. Rebentrost, S. Lloyd, and A. Aspuru-Guzik, The Journal of Chemical Physics **129**, 174106 (2008).

[133] M. A. Nielsen and I. L. Chuang, *Quantum Computation and Quantum Information* (Cambridge University Press, 2004).

[134] A. Acin, D. Bruß, M. Lewenstein, and A. Sanpera, Physical Review Letters **87**, 040401 (2001).

[135] W. E. Lamb Jr and R. C. Retherford, Physical Review **79**, 549 (1950).

[136] M. E. Peskin and D. V. Schroeder, *An introduction to quantum field theory* (1995).

[137] H. B. Casimir, in *Proc. K. Ned. Akad. Wet* (1948), vol. 51, p. 150.

[138] S. K. Lamoreaux, Physical Review Letters **78**, 5 (1997).

[139] U. Mohideen and A. Roy, Physical Review Letters **81**, 4549 (1998).

[140] G. T. Moore, Journal of Mathematical Physics **11**, 2679 (1970).

[141] P. Lähteenmäki, G. Paraoanu, J. Hassel, and P. J. Hakonen, Proceedings of the National Academy of Sciences **110**, 4234 (2013).

[142] D. A. Dalvit and P. A. M. Neto, Physical Review Letters **84**, 798 (2000).

[143] P. A. M. Neto and D. A. Dalvit, Physical Review A **62**, 042103 (2000).

[144] N. Narozhny, A. Fedotov, and Y. E. Lozovik, Physical Review A **64**, 053807 (2001).

[145] N. Narozhny, A. Fedotov, and Y. E. Lozovik, Laser Physics **13**, 298 (2003).

[146] A. Dodonov, V. Dodonov, and S. Mizrahi, Journal of Physics A: Mathematical and General **38**, 683 (2005).

[147] M. Andreata and V. Dodonov, Journal of Optics B: Quantum and Semiclassical Optics **7**, S11 (2005).

[148] A. Dodonov and V. Dodonov, Physical Review A **85**, 055805 (2012).

[149] M. J. Hartmann, F. G. Brandao, and M. B. Plenio, Nature Physics **2**, 849 (2006).

[150] T. D. Ladd, F. Jelezko, R. Laflamme, Y. Nakamura, C. Monroe, and J. L. O'Brien, Nature **464**, 45 (2010).

[151] J. Clarke and F. K. Wilhelm, Nature **453**, 1031 (2008).

[152] M. Devoret and R. Schoelkopf, Science **339**, 1169 (2013).

[153] J. M. Martinis, M. H. Devoret, and J. Clarke, Physical Review Letters **55**, 1543 (1985).

[154] H. Paik, D. Schuster, L. S. Bishop, G. Kirchmair, G. Catelani, A. Sears, B. Johnson, M. Reagor, L. Frunzio, L. Glazman, et al., Physical Review Letters **107**, 240501 (2011).

[155] J. B. Chang, M. R. Vissers, A. D. Córcoles, M. Sandberg, J. Gao, D. W. Abraham, J. M. Chow, J. M. Gambetta, M. B. Rothwell, G. A. Keefe, et al., Applied Physics Letters **103**, 012602 (2013).

[156] M. Wallquist, V. Shumeiko, and G. Wendin, Physical Review B **74**, 224506 (2006).

[157] D. E. Bruschi, C. Sabín, P. Kok, G. Johansson, P. Delsing, and I. Fuentes, preprint arXiv:1311.5619 (2013).

[158] T. P. Orlando and K. A. Delin, *Foundations of applied superconductivity*, vol. 224 (Addison-Wesley Reading, MA, 1991).

[159] M. Steffen, M. Ansmann, R. C. Bialczak, N. Katz, E. Lucero, R. McDermott, M. Neeley, E. M. Weig, A. N. Cleland, and J. M. Martinis, Science **313**, 1423 (2006).

[160] L. DiCarlo, J. Chow, J. Gambetta, L. S. Bishop, B. Johnson, D. Schuster, J. Majer, A. Blais, L. Frunzio, S. Girvin, et al., Nature **460**, 240 (2009).

[161] W. K. Wootters, Physical Review Letters **80**, 2245 (1998).

[162] B. Kraus and J. I. Cirac, Physical Review Letters **92**, 013602 (2004).

[163] G. Vidal and R. F. Werner, Physical Review A **65**, 032314 (2002).

[164] B. Jungnitsch, T. Moroder, and O. Gühne, Physical Review Letters **106**, 190502 (2011).

[165] C. Eltschka and J. Siewert, Scientific Reports **2** (2012).

[166] N. Kiesel, C. Schmid, G. Tóth, E. Solano, and H. Weinfurter, Physical Review Letters **98**, 063604 (2007).

[167] S. Felicetti, G. Romero, D. Rossini, R. Fazio, and E. Solano, Physical Review A **89**, 013853 (2014).

[168] Y. Shalibo, R. Resh, O. Fogel, D. Shwa, R. Bialczak, J. M. Martinis, and N. Katz, Physical Review Letters **110**, 100404 (2013).

[169] P. Bertet, A. Auffeves, P. Maioli, S. Osnaghi, T. Meunier, M. Brune, J.-M. Raimond, and S. Haroche, Physical Review Letters **89**, 200402 (2002).

[170] S. Deleglise, I. Dotsenko, C. Sayrin, J. Bernu, M. Brune, J.-M. Raimond, and S. Haroche, Nature **455**, 510 (2008).

[171] I. Rabi, Physical Review **49**, 324 (1936).

[172] E. Irish, Physical Review Letters **99**, 173601 (2007).

[173] S. De Liberato, Physical Review Letters **112**, 016401 (2014).

[174] S. Srinivasan, A. Hoffman, J. Gambetta, and A. Houck, Physical Review Letters **106**, 083601 (2011).

[175] J. Gambetta, W. Braff, A. Wallraff, S. Girvin, and R. Schoelkopf, Physical Review A **76**, 012325 (2007).

[176] M. Steffen, M. Ansmann, R. McDermott, N. Katz, R. C. Bialczak, E. Lucero, M. Neeley, E. M. Weig, A. N. Cleland, and J. M. Martinis, Physical Review Letters **97**, 050502 (2006).

[177] Y. Todorov, A. Andrews, I. Sagnes, R. Colombelli, P. Klang, G. Strasser, and C. Sirtori, Physical Review Letters **102**, 186402 (2009).

[178] B. Askenazi, A. Vasanelli, A. Delteil, Y. Todorov, L. Andreani, G. Beaudoin, I. Sagnes, and C. Sirtori, New Journal of Physics **16**, 043029 (2014).

[179] S. Kéna-Cohen, S. A. Maier, and D. D. Bradley, Advanced Optical Materials **1**, 827 (2013).

[180] G. Scalari, C. Maissen, D. Turčinková, D. Hagenmüller, S. De Liberato, C. Ciuti, C. Reichl, D. Schuh, W. Wegscheider, M. Beck, et al., Science **335**, 1323 (2012).

[181] V. Muravev, I. Andreev, I. Kukushkin, S. Schmult, and W. Dietsche, Physical Review B **83**, 075309 (2011).

[182] T. Werlang, A. Dodonov, E. Duzzioni, and C. Villas-Bôas, Physical Review A **78**, 053805 (2008).

[183] R. Stassi, A. Ridolfo, O. Di Stefano, M. Hartmann, and S. Savasta, Physical Review Letters **110**, 243601 (2013).

[184] S. Haroche, Reviews of Modern Physics **85**, 1083 (2013).

[185] D. J. Wineland, Reviews of Modern Physics **85**, 1103 (2013).

[186] C. Blockley, D. Walls, and H. Risken, Europhysics Letters **17**, 509 (1992).

[187] A. Sørensen and K. Mølmer, Physical Review Letters **82**, 1971 (1999).

[188] E. Solano, R. de Matos Filho, and N. Zagury, Physical Review A **59**, R2539 (1999).

[189] E. Solano, R. de Matos Filho, and N. Zagury, Physical Review Letters **87**, 060402 (2001).

[190] P. Haljan, K.-A. Brickman, L. Deslauriers, P. Lee, and C. Monroe, Physical Review Letters **94**, 153602 (2005).

[191] T. Salger, C. Grossert, S. Kling, and M. Weitz, Physical Review Letters **107**, 240401 (2011).

[192] F. Dreisow, M. Heinrich, R. Keil, A. Tünnermann, S. Nolte, S. Longhi, and A. Szameit, Physical Review Letters **105**, 143902 (2010).

[193] M.-J. Hwang and M.-S. Choi, Physical Review A **82**, 025802 (2010).

[194] B. Peropadre, P. Forn-Díaz, E. Solano, and J. J. García-Ripoll, Physical Review Letters **105**, 023601 (2010).

[195] S. Felicetti, T. Douce, G. Romero, P. Milman, and E. Solano, preprint arXiv:1411.7968 (2014).

[196] Q.-T. Xie, S. Cui, J.-P. Cao, L. Amico, and H. Fan, Physical Review X **4**, 021046 (2014).

[197] S. Cui, J.-P. Cao, and L. Amico, preprint arXiv:1504.04701 (2015).

[198] H. Zhong, Q. Xie, X. Guan, M. T. Batchelor, K. Gao, and C. Lee, Journal of Physics A: Mathematical and Theoretical **47**, 045301 (2014).

[199] I. Travěnec, Physical Review A **85**, 043805 (2012).

[200] A. J. Maciejewski, M. Przybylska, and T. Stachowiak, preprint arXiv:1503.05636 (2015).

[201] I. Travěnec, Physical Review A **91**, 037802 (2015).

[202] V. V. Albert, G. D. Scholes, and P. Brumer, Physical Review A **84**, 042110 (2011).

[203] D. Braak, Journal of Physics B: Atomic, Molecular and Optical Physics **46**, 224007 (2013).

[204] K. Ng, C. Lo, and K. Liu, The European Physical Journal D-Atomic, Molecular, Optical and Plasma Physics **6**, 119 (1999).

[205] C. Emary and R. Bishop, Journal of Physics A: Mathematical and General **35**, 8231 (2002).

[206] J. Pedernales, I. Lizuain, S. Felicetti, G. Romero, L. Lamata, and E. Solano, preprint arXiv:1505.00698 (2015).

[207] P. Bertet, S. Osnaghi, P. Milman, A. Auffeves, P. Maioli, M. Brune, J.-M. Raimond, and S. Haroche, Physical Review Letters **88**, 143601 (2002).

[208] S. Stufler, P. Machnikowski, P. Ester, M. Bichler, V. Axt, T. Kuhn, and A. Zrenner, Physical Review B **73**, 125304 (2006).

[209] E. Del Valle, S. Zippilli, F. P. Laussy, A. Gonzalez-Tudela, G. Morigi, and C. Tejedor, Physical Review B **81**, 035302 (2010).

[210] y. Leibfried, R. Blatt, C. Monroe, and D. Wineland, Reviews of Modern Physics **75**, 281 (2003).

[211] H. Häffner, C. F. Roos, and R. Blatt, Physics Reports **469**, 155 (2008).

[212] R. de Matos Filho and W. Vogel, Physical Review A **50**, R1988 (1994).

[213] D. Meekhof, C. Monroe, B. King, W. Itano, and D. Wineland, Physical Review Letters **76**, 1796 (1996).

[214] R. de Matos Filho and W. Vogel, Physical Review Letters **76**, 608 (1996).

[215] S.-C. Gou, J. Steinbach, and P. Knight, Physical Review A **55**, 3719 (1997).

[216] P. Alsing and M. S. Zubairy, JOSA B **4**, 177 (1987).

[217] A. Joshi, Physical Review A **62**, 043812 (2000).

[218] C. Senko, J. Smith, P. Richerme, A. Lee, W. Campbell, and C. Monroe, Science **345**, 430 (2014).

[219] D. S. Abrams and S. Lloyd, Physical Review Letters **83**, 5162 (1999).

[220] P. Jurcevic, B. P. Lanyon, P. Hauke, C. Hempel, P. Zoller, R. Blatt, and C. F. Roos, Nature **511**, 202 (2014).

[221] A. Recati, P. Fedichev, W. Zwerger, J. Von Delft, and P. Zoller, Physical Review Letters **94**, 040404 (2005).

[222] P. P. Orth, I. Stanic, and K. Le Hur, Physical Review A **77**, 051601 (2008).

[223] M. Cirone, G. De Chiara, G. Palma, and A. Recati, New Journal of Physics **11**, 103055 (2009).

[224] G. Ritt, C. Geckeler, T. Salger, G. Cennini, and M. Weitz, Physical Review A **74**, 063622 (2006).

[225] D. Witthaut, T. Salger, S. Kling, C. Grossert, and M. Weitz, Physical Review A **84**, 033601 (2011).

[226] T. Salger, S. Kling, T. Hecking, C. Geckeler, L. Morales-Molina, and M. Weitz, Science **326**, 1241 (2009).

[227] G. Cennini, G. Ritt, C. Geckeler, and M. Weitz, Physical Review Letters **91**, 240408 (2003).

[228] T. Salger, C. Geckeler, S. Kling, and M. Weitz, Physical Review Letters **99**, 190405 (2007).

[229] I. Bloch, J. Dalibard, and W. Zwerger, Reviews of Modern Physics **80**, 885 (2008).

[230] A. Kastberg, W. D. Phillips, S. Rolston, R. Spreeuw, and P. Jessen, Physical Review Letters **74**, 1542 (1995).

[231] G.-R. Juan Jose, D. Zueco, D. Porras, and B. Peropadre, in *APS Meeting Abstracts* (2014), vol. 1, p. 34006.

[232] R. Stassi, S. De Liberato, L. Garziano, B. Spagnolo, and S. Savasta, preprint arXiv:1501.07536 (2015).

[233] G. Benenti, A. D'Arrigo, S. Siccardi, and G. Strini, Physical Review A **90**, 052313 (2014).

[234] K. K. Likharev, *Dynamics of Josephson Junctions and Circuits* (Gordon, 1992).

[235] V. Bargmann, Communications on pure and applied mathematics **14**, 187 (1961).

[236] S. I. Slavianov and W. Lay, *Special functions: a unified theory based on singularities* (Oxford University Press, 2000).

[237] I. M. Gelfand and N. J. Vilekin, *Generalized Functions* (Academic Press, New York, 1964).